



**HAL**  
open science

## Design of SRAM for CMOS 32nm

Lahcen Hamouche

► **To cite this version:**

Lahcen Hamouche. Design of SRAM for CMOS 32nm. Other. INSA de Lyon, 2011. English. NNT : 2011ISAL0013 . tel-00715803

**HAL Id: tel-00715803**

**<https://theses.hal.science/tel-00715803>**

Submitted on 9 Jul 2012

**HAL** is a multi-disciplinary open access archive for the deposit and dissemination of scientific research documents, whether they are published or not. The documents may come from teaching and research institutions in France or abroad, or from public or private research centers.

L'archive ouverte pluridisciplinaire **HAL**, est destinée au dépôt et à la diffusion de documents scientifiques de niveau recherche, publiés ou non, émanant des établissements d'enseignement et de recherche français ou étrangers, des laboratoires publics ou privés.

# THÈSE

présentée

Devant L ' Institut National des Sciences Appliquées de Lyon

pour obtenir le grade de :

**Docteur**  
**Ecole Doctorale EEA**  
**Spécialité : Génie Électrique**

Par

**Lahcen HAMOUCHE**  
**Master Recherche, Université de Rouen**

Ingénieur STMicroelectronics  
(CCDS SRAM CROLLES)

Titre de la thèse :

**Conception de Mémoires SRAM  
en technologie CMOS 32nm**

**Design of SRAM for CMOS 32nm**

Soutenue le xx-xx-2011 devant la commission d'examen composée de :

|                    |   |            |
|--------------------|---|------------|
| Patrick GIRARD     | DR CNRS, LIRMM, Univ. Montpellier                         | Rapporteur |
| Jean-Michel PORTAL | Professeur, IM2NP,<br>Univ. Provence Polytech'Marseilles  | Rapporteur |
| Amara AMARA        | Professeur,<br>Institut Supérieur d'Electronique de Paris |            |
| Bruno ALLARD       | Professeur, Ampère, INSA-Lyon                             |            |
| David TURGIS       | STMicroelectronics, Crolles                               |            |





**INSA Direction de la Recherche - Ecoles Doctorales – Quadriennal 2007-2010**

| SIGLE            | ECOLE DOCTORALE  | NOM ET COORDONNEES DU RESPONSABLE   |
|------------------|--|---|
| <b>CHIMIE</b>    | <b>CHIMIE DE LYON</b><br><a href="http://sakura.cpe.fr/ED206">http://sakura.cpe.fr/ED206</a><br><br>M. Jean Marc LANCELIN<br><br>Insa : R. GOURDON   | M. Jean Marc LANCELIN<br>Université Claude Bernard Lyon 1<br>Bât CPE<br>43 bd du 11 novembre 1918<br>69622 VILLEURBANNE Cedex<br>Tél : 04.72.43 13 95 Fax :<br>lancelin@hikari.cpe.fr   |
| <b>E.E.A.</b>    | <b>ELECTRONIQUE,<br/>ELECTROTECHNIQUE, AUTOMATIQUE</b><br><a href="http://www.insa-lyon.fr/eea">http://www.insa-lyon.fr/eea</a><br>M. Alain NICOLAS<br>Insa : C. PLOSSU<br>ede2a@insa-lyon.fr<br>Secrétariat : M. LABOUNE<br>AM. 64.43 – Fax : 64.54 | M. Alain NICOLAS<br>Ecole Centrale de Lyon<br>Bâtiment H9<br>36 avenue Guy de Collongue<br>69134 ECULLY<br>Tél : 04.72.18 60 97 Fax : 04 78 43 37 17<br>eea@ec-lyon.fr<br>Secrétariat : M.C. HAVGOUDOUKIAN  |
| <b>E2M2</b>      | <b>EVOLUTION, ECOSYSTEME,<br/>MICROBIOLOGIE, MODELISATION</b><br><a href="http://biomserv.univ-lyon1.fr/E2M2">http://biomserv.univ-lyon1.fr/E2M2</a><br><br>M. Jean-Pierre FLANDROIS<br>Insa : H. CHARLES  | M. Jean-Pierre FLANDROIS<br>CNRS UMR 5558<br>Université Claude Bernard Lyon 1<br>Bât G. Mendel<br>43 bd du 11 novembre 1918<br>69622 VILLEURBANNE Cédex<br>Tél : 04.26 23 59 50 Fax 04 26 23 59 49<br>06 07 53 89 13<br>e2m2@biomserv.univ-lyon1.fr   |
| <b>EDISS</b>     | <b>INTERDISCIPLINAIRE SCIENCES-<br/>SANTÉ</b><br><br>Sec : Safia Boudjema<br>M. Didier REVEL<br>Insa : M. LAGARDE  | M. Didier REVEL<br>Hôpital Cardiologique de Lyon<br>Bâtiment Central<br>28 Avenue Doyen Lépine<br>69500 BRON<br>Tél : 04.72.68 49 09 Fax :04 72 35 49 16<br>Didier.revel@creatis.uni-lyon1.fr   |
| <b>INFOMATHS</b> | <b>INFORMATIQUE ET<br/>MATHEMATIQUES</b><br><a href="http://infomaths.univ-lyon1.fr">http://infomaths.univ-lyon1.fr</a><br>M. Alain MILLE<br><br>Secrétariat : C. DAYEYAN  | M. Alain MILLE<br>Université Claude Bernard Lyon 1<br>LIRIS - INFOMATHS<br>Bâtiment Nautibus<br>43 bd du 11 novembre 1918<br>69622 VILLEURBANNE Cedex<br>Tél : 04.72. 44 82 94 Fax 04 72 43 13 10<br><a href="mailto:infomaths@bat710.univ-lyon1.fr">infomaths@bat710.univ-lyon1.fr</a> - alain.mille@liris.cnrs.fr |
| <b>Matériaux</b> | <b>MATERIAUX DE LYON</b><br><br>M. Jean Marc PELLETIER<br><br>Secrétariat : C. BERNAVON<br>83.85   | M. Jean Marc PELLETIER<br>INSA de Lyon<br>MATEIS<br>Bâtiment Blaise Pascal<br>7 avenue Jean Capelle<br>69621 VILLEURBANNE Cédex<br>Tél : 04.72.43 83 18 Fax 04 72 43 85 28<br>Jean-marc.Pelletier@insa-lyon.fr  |
| <b>MEGA</b>      | <b>MECANIQUE, ENERGETIQUE, GENIE<br/>CIVIL, ACOUSTIQUE</b><br><br>M. Jean Louis GUYADER<br><br>Secrétariat : M. LABOUNE<br>PM : 71.70 –Fax : 87.12   | M. Jean Louis GUYADER<br>INSA de Lyon<br>Laboratoire de Vibrations et Acoustique<br>Bâtiment Antoine de Saint Exupéry<br>25 bis avenue Jean Capelle<br>69621 VILLEURBANNE Cedex<br>Tél :04.72.18.71.70 Fax : 04 72 43 72 37<br>mega@lva.insa-lyon.fr  |
| <b>ScSo</b>      | <b>ScSo*</b><br><br>M. OBADIA Lionel<br><br>Insa : J.Y. TOUSSAINT  | M. OBADIA Lionel<br>Université Lyon 2<br>86 rue Pasteur<br>69365 LYON Cedex 07<br>Tél : 04.78.69.72.76 Fax : 04.37.28.04.48<br>Lionel.Obadia@univ-lyon2.fr  |

\*ScSo : Histoire, Géographie, Aménagement, Urbanisme, Archéologie, Science politique, Sociologie, Anthropologie



---

## Author's Publications and patents

---

### ■ JOURNALS:

- Hamouche, Lahcen; Allard, Bruno; , "Low power options for 32nm always-on SRAM architecture", (Accepted for publication to) Solid-State Electronics Journal, 2011.

### ■ INT. CONFERENCES:

- Hamouche, Lahcen; Allard, Bruno; , "PORTLESS low power mux architecture with line hard duplication," International Memory Workshop (IMW), 2010 IEEE International , vol., no., pp.1-4, 16-19 May 2010 doi: 10.1109/IMW.2010.5488404
- Hamouche, Lahcen; Allard, Bruno; LAFONT Jean-christophe , "SRAM portless bitcell and current-mode reading," Circuits and Systems (ISCAS), Proceedings of 2010 IEEE International Symposium on , vol., no., pp.3865-3868, May 30 2010-June 2 2010 doi: 10.1109/ISCAS.2010.5537704

### ■ Patents :

- Low power robust current mode sensing for 5T-portless SRAM, FR/ 28.07.09/FRA 0955274
- Low power multiplexer architecture, FR/ 26.01.10/ FRA 1050487

### ■ Rejected:

- Hamouche, Lahcen; Allard, Bruno; , "5T-Portless SRAM as a candidate for 32nm always-on memory", Transactions on Very Large Scale Integration (TVLSI) journal.



---

## Abstract

---

More and more specific applications are demanding large SRAM blocs in advance technologies. Particularly there is a need for always-on memories that consequently must be low energy consuming. For example mobile heterogeneous wireless networks are implementing multiple interfaces that are attached to concurrent networks at the same time and therefore manage multiple IP addresses simultaneously. The large amount of memory faces a serious problem of power consumption. The classical strategy of bloc extinction comes to a limit in effective energy saving and system dynamic performances. There is then a need for true always-on but very low power SRAM. Besides the design of SRAM memories in advanced technology must take into account the problem of reliability in terms of Process-Voltage-Temperature (PVT) variabilities.

Manuscript reviews the technical and industrial challenges regarding embedded SRAM, with a stress on power consumption. Always-on SRAMs offer a particular challenging example. State of art compares SRAM architectures from various viewpoints:

- Performances versus PVT variability
- Robustness of migration in further technology nodes
- Tradeoffs between bit-cell and peripherals complexities

State of the art reviews the exploratory works on analytical modeling for variability statistics

Chapter 3 wishes to discuss analytical modeling for variability statistic as a mean to simplify 32nm SRAM design. A proposal of modeling is presented to describe the statistical behavior of performance key parameters. Modeling is based on various assumptions but enables to show clear limitations of several target design parameters.

Chapter 4 details a bit-cell alternative to a 6T, 7T, 8T... as a 5T bit-cell called 5T-Portless SRAM. The performances and advantages of 5T-Portless rely on a current mode operation that offers a large reduction in dynamic power consumption additionally to a low leakage bit-cell. Operation and performance parameters are discussed from simulation based on latest update 32nm Design-Kit (high-k metal gate).

Chapter 5 details the design of a memory cut with a special emphasis on line hardcopy, matrix options and required peripherals. Design yields the layout of a 1024x64 (64kb) memory that is currently under fabrication. Results and characterizations will be included in this chapter and compared to simulation evaluations.



## Abstract

---

The conclusion chapter highlights the major contributions of the study and discusses the various simplification assumptions to see possible limitations. It is concluded affirmatively about industrial interest of the 5T-Portless SRAM for always-on embedded applications. Perspectives concern the analytical modeling for statistical behavior of SRAM as the Monte-Carlo approach is no more practicable. The migration of the 5T-Portless SRAM may be already considered in advanced nodes.

PhD results have received the following attention:

- 2 patent claims with one international extension
- 2 communications in IEEE conferences ( ISCAS 2010, IMW 2010)
- 2 submitted articles to Journal of (Solid State Circuit and Microelectronic Journal)

---

## Résumé

---

De plus en plus d'applications spécifiques embarquées exigent de larges blocs de mémoires statiques SRAM. En particulier il y a un besoin de mémoires inconditionnellement actives pour lesquelles la consommation d'énergie est un paramètre clé. Par exemple les réseaux sans fil hétérogènes sont caractérisés par plusieurs interfaces tournées vers des réseaux différents, donc de multiples adresses IP simultanées. Une grande quantité de mémoire est mobilisée et pose un sérieux problème de consommation d'énergie vis-à-vis de l'autonomie de système mobile. La stratégie classique d'extinction des blocs mémoire momentanément non opérationnelle ne permet qu'une réduction faible en consommation et limite les performances dynamiques du système. Il y a donc un réel besoin pour une mémoire toujours opérationnelle avec un très faible bilan énergétique. Par ailleurs les technologies CMOS avancées posent le problème de la variabilité et la conception de mémoire SRAM doit aboutir à un niveau de fiabilité très grand.

Le manuscrit décrit les verrous techniques et industriels concernant la mémoire embarquée SRAM très faible consommation. Le cas de la mémoire toujours opérationnelle représente un défi pertinent. Un état de l'art balaie les architectures SRAM avec plusieurs points de vue :

- Niveau des performances en fonction de la variabilité
- Capacité à la migration technologique
- Compromis entre les niveaux cellules et périphérie de la mémoire

L'état de l'art s'intéresse aux tentatives de modélisation statistique vis-à-vis de la variabilité.

Le chapitre 2 offre une discussion à propos de la modélisation analytique statistique comme moyen de simplification de la conception en 32nm. En introduisant quelques simplifications, des paramètres clé de la conception sont modélisés pour en obtenir des spécifications et en voir d'éventuelles limites.

Le chapitre 3 décrit une cellule alternative aux 6T , 7T et 8T, laquelle est appelée 5T-Portless. Les avantages et les performances de cette cellule 5T-Portless repose sur son fonctionnement en mode courant à l'origine de la réduction significative de la consommation dynamique ajoutée à une cellule intrinsèquement peu fuiteuse. Le fonctionnement et l'analyse de performances sont basés sur des simulations et un Design-Kit le plus à jour en 32nm.

## Résumé

---

Le chapitre 4 détaille la conception d'un bloc mémoire avec une attention particulière pour la recopie analogique de ligne, les possibilités de mise en matrice et différents périphériques. Un démonstrateur de 64kb (1024x64b) a été dessiné en CMOS32nm. Les résultats expérimentaux viendront compléter le chapitre et seront comparés à la simulation.

La conclusion générale reprend les résultats les plus significatifs et rediscute les principales hypothèses. La conclusion est favorable quand à l'intérêt industriel de la 5T-Portless comme mémoire embarquée toujours active. Les perspectives concernent la modélisation statistique sachant que l'approche Monte-Carlo n'est plus envisageable, et la migration de la SRAM dans d'autres Design-Kits.

Les travaux ont donné lieu à :

- Deux dépôts de brevet français repris en une extension internationale
- Deux articles de conférences IEEE ( ISCAS 2010, IMW 2010)
- Deux articles soumis à des journaux ( Solid State Circuit et Microelectronic Journal)

---

# Contents

---

|  |             |
|--|-------------|
| <b>List of Figures</b>   | <b>x</b>    |
| <b>List of Tables</b>  | <b>xiii</b> |
| <b>Abbreviations</b>   | <b>xiv</b>  |
| <b>1 Introduction</b>  | <b>1</b>    |
| <b>2 State of art of eSRAM</b>                                 | <b>5</b>    |
| 2.1 6T SRAM . . . . .  | 7           |
| 2.1.1 Read operation . . . . .                                 | 7           |
| 2.1.2 Write operation . . . . .                                | 12          |
| 2.1.3 SRAM bit-cell sizing . . . . .                           | 13          |
| 2.1.4 Retention mode . . . . .                                 | 15          |
| 2.2 Power consumption and variability . . . . .                | 17          |
| 2.2.1 Variability and consumption of a SRAM bit-cell . . . . . | 17          |
| 2.2.2 SRAM Periphery . . . . .                                 | 26          |
| 2.2.3 Conclusion . . . . .                                     | 26          |
| <b>3 Modeling for variability</b>                              | <b>29</b>   |
| 3.1 Yields and margins in SRAM . . . . .                       | 30          |
| 3.2 Discussion on modeling results . . . . .                   | 38          |
| <b>4 PORTLESS BIT-CELL AND CURRENT MODE OPERATION</b>          | <b>45</b>   |
| 4.1 5T SRAM bit-cells . . . . .                                | 45          |
| 4.2 5T-Portless bit-cell . . . . .                             | 46          |
| 4.2.1 5T-Portless bit-cell parameters . . . . .                | 51          |
| 4.2.2 Wordline driver . . . . .                                | 51          |
| 4.3 Hard-line duplication technique . . . . .                  | 53          |
| 4.4 Portless Sense and Mux architecture . . . . .              | 55          |
| 4.4.1 Current mode sensing and writing . . . . .               | 57          |
| 4.4.2 Low Power Mux structure . . . . .                        | 58          |

## Contents

---

|          |   |            |
|----------|---|------------|
| <b>5</b> | <b>Test chip and simulation results</b> | <b>63</b>  |
| 5.1      | Test chip design . . . . .              | 65         |
| 5.1.1    | Bit-cell to matrix array . . . . .      | 65         |
| 5.1.2    | Control block . . . . .                 | 68         |
| 5.1.2.1  | Pulse generator . . . . .               | 70         |
| 5.1.2.2  | Signal Generator . . . . .              | 72         |
| 5.1.2.3  | Word line driver: <i>WLD</i> . . . . .  | 73         |
| 5.1.3    | Y decoder . . . . .                     | 74         |
| 5.1.4    | Input/Output . . . . .                  | 77         |
| 5.2      | Simulation results . . . . .            | 79         |
| 5.2.1    | Comparison with the 6T SRAM . . . . .   | 87         |
| 5.3      | Testchip Results . . . . .              | 89         |
| 5.3.1    | Test Chip environnement . . . . .       | 90         |
| 5.3.2    | Portless Results . . . . .              | 92         |
| <b>6</b> | <b>Conclusion</b>                       | <b>95</b>  |
|          | <b>Bibliography</b>                     | <b>100</b> |

---

## List of Figures

---

|      |  |    |
|------|--|----|
| 2.1  | 6T SRAM bit-cell . . . . .   | 8  |
| 2.2  | 6T Butterfly curve (32nm and typical condition simulation) . . . . .   | 9  |
| 2.3  | SNM evaluation by simulation . . . . .   | 9  |
| 2.4  | Simulated SNM-curve for a CMOS 45nm SRAM under (a) process variations, (b) power supply variations and (c) temperature variations between -40°C and +125°C . . . . . | 10 |
| 2.5  | Butterfly curve for different sizes of 6T bit-cell in 32nm (simulations by Mastar) . . . . .   | 10 |
| 2.6  | Tree of variation propagation from process to transistor and circuit . . . . .   | 11 |
| 2.7  | Transient simulation result of read and write operation : (a) simulation without mismatch, (b) simulation with device mismatch . . . . .                             | 11 |
| 2.8  | Write operation in 6T Bit-cell . . . . .   | 12 |
| 2.9  | Process corners according to the NMOS and PMOS $V_{th}$ values . . . . .   | 13 |
| 2.10 | <b>WM</b> and <b>SNM</b> versus the ratio $N=\alpha/\beta$ . . . . .   | 14 |
| 2.11 | 6T SRAM bit-cell leakage versus $V_{DD}$ in CMOS 32nm . . . . .  | 15 |
| 2.12 | DVR, Leakage and dynamic power comparison . . . . .  | 18 |
| 2.13 | Most popular leakage reducing techniques . . . . .   | 19 |
| 2.14 | simulation results of the reducing leakage techniques . . . . .  | 20 |
| 2.15 | $V_{DD}$ scaling . . . . .   | 21 |
| 2.16 | Negative bit-line . . . . .  | 21 |
| 2.17 | Word line boosting . . . . .   | 22 |
| 2.18 | simulated 6T butterfly curve for $V_{DD}=1.2V$ and $V_{DD}=0.8V$ . . . . .   | 23 |
| 2.19 | SNM simulation comparison for 32nm bit-cells . . . . .   | 24 |
| 2.20 | $\Delta V_{BL}$ and $V_{SAO}$ distribution overlapping (Monte Carlo simulations) . . . . .   | 25 |
| 2.21 | 6T bit-cell Multiplexed structure . . . . .  | 25 |
| 3.1  | Transient simulation of the bit-line discharge in read operation of a 6T SRAM in CMOS 32nm . . . . .   | 32 |
| 3.2  | Bit-lines' voltage difference during discharged time $t_a$ . . . . .   | 33 |
| 3.3  | SRAM array with Y decoders and sense amplifier . . . . .   | 34 |
| 3.4  | Distribution function of $F_Z(0)$ versus $t_a$ with $C_{BL}=200$ fF . . . . .  | 37 |
| 3.5  | $V_{SAO}$ and $\Delta V_{BL}$ results of Monte Carlo simulation . . . . .  | 39 |
| 3.6  | Monte Carlo simulation results $\Delta V_{BL}$ for different $t_a$ values . . . . .  | 41 |
| 3.7  | $\mu_{\Delta V_{BL}}$ and $\sigma_{\Delta V_{BL}}$ versus the discharge time $t_a$ . . . . .   | 41 |

## List of Figures

---

|      |  |    |
|------|--|----|
| 3.8  | $t_a$ margin variation with a 10% $\sigma$ increasing . . . . .  | 42 |
| 4.1  | Schematic and simulated SNM of 45nm 5T asymmetric SRAM (a,c) and 5T Portless SRAM (b,d) . . . . .  | 46 |
| 4.2  | Portless bit-cell: (a) schematic, (b) layout . . . . .   | 47 |
| 4.3  | Portless current in read operation . . . . .   | 47 |
| 4.4  | BFC comparison of Monte Carlo simulation with $N=10^4$ iteration between 6T (a) and Portless (b) and gaussian distribution fit (c) . . . . . | 48 |
| 4.5  | leakage comparison between 6T and Portless bit-cells . . . . .   | 49 |
| 4.6  | Monte Carlo simulation results of $I_{read}$ for a typical PVT corner in CMOS 32nm . . . . .   | 50 |
| 4.7  | Portless bit-cell parameters . . . . .   | 52 |
| 4.8  | $\Delta VR$ and $I_{read}$ Versus VAXS . . . . .   | 52 |
| 4.9  | PMOS, NMOS Voltage divider . . . . .   | 53 |
| 4.10 | simulation results of WLD in different PVT corners . . . . .   | 54 |
| 4.11 | Charge pump circuit and the Word-Lline Driver with RP and WP signal sets . . . . .   | 54 |
| 4.12 | Proposal of Portless bit-cell arrangement . . . . .  | 56 |
| 4.13 | Bit-line and internal nodes voltage in read and write operation . . . . .  | 57 |
| 4.14 | Portless bit-cell column with IOcell . . . . .   | 59 |
| 4.15 | Mux bit-cells and Sense . . . . .  | 60 |
| 4.16 | Vaxs and cells' internal node voltages during a write operation in a CMOS32nm Portless arrangement . . . . .                                 | 61 |
| 4.17 | Portless multiplexer architecture . . . . .  | 62 |
| 5.1  | Schematic of the 5T-Portless memory cut . . . . .  | 64 |
| 5.2  | 5T-Portless bit-cell, schematic (a), layout (b) . . . . .  | 66 |
| 5.3  | Mux cell layout (a) and schematic (b) . . . . .  | 67 |
| 5.4  | precharge circuit (a) layout (b) schematic . . . . .   | 68 |
| 5.5  | The Sub-matrix column arrangement . . . . .  | 69 |
| 5.6  | Sub-matrix array of $32 \times 64$ , Mux cell, dummy line and precharge circuit . . . . .  | 69 |
| 5.7  | Pulse diagram generation according to write or read operations . . . . .   | 70 |
| 5.8  | Control blocks with different input output signals . . . . .   | 71 |
| 5.9  | VAXS and OAXS in both write and read operation generated by WP and WP . . . . .  | 72 |
| 5.10 | WLD block with different input and output signals . . . . .  | 74 |
| 5.11 | Cell's internal nodes voltages and AXS signals in both write and read operations . . . . .   | 75 |
| 5.12 | Ydecoder for both sub-matrix word line selection and sub-matrix selection . . . . .  | 76 |
| 5.13 | Local decoder and predecoder layout . . . . .  | 76 |

---

|      |   |    |
|------|---|----|
| 5.14 | Layout of the sub-matrix including Matrix array, Control block, Mux, and Ydecoder . . . . .   | 77 |
| 5.15 | Schematic and layout of IOcell with $Q$ and $\bar{Q}$ output data and $D$ and $\bar{D}$ input data . . . . .                              | 78 |
| 5.16 | Cut layout with the 32 sub-matrices and Inpu/Output interfaces . . . . .  | 78 |
| 5.17 | Bit effective area . . . . .  | 79 |
| 5.18 | A critical path in the matrix array with the critical bit-cells to be simulated   | 80 |
| 5.19 | Simulation of read and write operations for the full memory cut using the xasimulator . . . . .   | 82 |
| 5.20 | Simulation results for the read delay (Critical Path simulation with Eldo   | 82 |
| 5.21 | Bit-cell read current for different PVT corners . . . . .   | 83 |
| 5.22 | Leakage current difference induced by a bit-cell in the retention mode and the total bit-cell leakage in both FS and SF corners . . . . . | 84 |
| 5.23 | Bit-cell leakage in different PVT corners, simulated by Eldo in CMOS 32nm . . . . .   | 85 |
| 5.24 | Dynamic power consumption during a read operation in different PVT corners . . . . .  | 86 |
| 5.25 | Comparison of 6T SRAM column and Portless column . . . . .  | 87 |
| 5.26 | Current waveforms during read and write operations in both 6T and Portless SRAM . . . . .   | 88 |
| 5.27 | Portless CUT with other memories and logical IPs . . . . .  | 90 |
| 5.28 | Values of $I_{ON}$ of NMOS and PMOS given by the CAD and test chip measurements . . . . .   | 91 |
| 5.29 | Test chip results for the full cut leakage current . . . . .  | 93 |
| 5.30 | Test chip dynamic current measurements and CAD values for the full memory cut. . . . .  | 93 |





---

## List of Tables

---

|      |   |    |
|------|---|----|
| 3.1  | some values of $\frac{Y_L}{N}$ versus $t_a$ . . . . .   | 37 |
| 3.2  | transistor threshold voltage $V_{th}$ value and standard deviation across different technology nodes . . . . .    | 40 |
| 5.1  | Testchip PVT Specification . . . . .  | 65 |
| 5.2  | Simplified logical equations for <i>AXS</i> , <i>LAXS</i> , <i>GAXS</i> , <i>OAXS</i> signals . . . . .           | 73 |
| 5.3  | Extracted parameters from the critical path simulation . . . . .  | 81 |
| 5.4  | Hard line duplication delay in different PVT corners . . . . .  | 83 |
| 5.5  | Bit-cell leakage values for different process corners in case of ( $V_{DD}=1V$ , <b>Temp=25°C</b> ) . . . . .     | 84 |
| 5.6  | Bit-cell leakage values for different process corners in case of ( $V_{DD}=1.1V$ , <b>Temp= 125°C</b> ) . . . . . | 85 |
| 5.7  | Bit-cell leakage values for different process corners in case of ( $V_{DD}=0.9V$ , <b>Temp= -40°C</b> ) . . . . . | 85 |
| 5.8  | Bit-cell leakage values in typical, fastest and slowest corners . . . . .   | 85 |
| 5.9  | Dynamic power consumption of the full cut in typical and worst case corners . . . . .                             | 86 |
| 5.10 | Leakage current values comparison between Portless and 6T SRAM bit-cells . . . . .                                | 89 |
| 5.11 | Leakage current values comparison between Portless and 6T SRAM bit-cells . . . . .                                | 89 |



---

## Abbreviations

---

|                 |  |
|-----------------|--|
| SRAM            | Static Random Access Memory              |
| CMOS            | Complementary metal oxide semi-conductor |
| PU              | Pull Up                                  |
| PD              | Pull Down                                |
| PG              | Pass Gate                                |
| BLT             | Bit-Line True                            |
| BLF             | Bit-Line False                           |
| LBL             | Local Bit-lines                          |
| GBL             | Global Bit-lines                         |
| SA              | Sense Amplifier                          |
| SNM             | Static Noise Margin                      |
| WM              | Write Margin                             |
| $I_{read}$      | Bit-Cell read Current                    |
| PVT             | Process Voltage Temperature              |
| MC              | Monte Carlo                              |
| $V_{th}$        | threshold Voltage                        |
| DRV             | Data Retention Voltage                   |
| RBB             | Reverse Body Bias                        |
| FBB             | Forward Body Bias                        |
| $\Delta V_{BL}$ | Bit-Line Voltage difference              |
| $V_{SAO}$       | Sense Amplifier Offset                   |
| $\sigma$        | Standard deviation                       |
| $\mu$           | Average Value                            |
| RYL             | Read Operation Yield                     |
| AQL             | Acceptable Quality Level                 |
| $t_a$           | Bit-Line discharge delay                 |
| WLD             | Word Line Driver                         |
| Gcell           | Global Mux-cell bit-cell                 |
| Lcell           | Local Mux-cell bit-cell                  |
| IOcell          | Input Output Cell                        |
| $VAXS_{read}$   | VAXS voltage for the read operation      |

## List of Tables

---

|                       |                                      |
|-----------------------|--------------------------------------|
| VAXS <sub>write</sub> | VAXS voltage for the write operation |
| MSB                   | Most Significant Bit                 |
| LSB                   | Least Significant Bit                |
| RO                    | Ring oscillators                     |
| DRC                   | Design Rule Check                    |
| LVS                   | Layout Versus Schematic              |

---

## Introduction

---

Today, systems on Chip are always a fast growing market. They embedded more and more complex functions that require an increasing memory capacity. The Static Random Access Memory **SRAM** is the mostly used solution where either bandwidth or low power, or both are principal considerations. SRAM is a type of semiconductor memory where the word static indicates that, unlike dynamic RAM (DRAM) [1], it does not need to be periodically refreshed, as SRAM uses bistable latching circuitry to store each bit. SRAM exhibits data remanence, but is still volatile in the conventional sense that data is eventually lost when the memory is not powered. SRAM is also easier to control (interface to) and generally more truly random access than modern types of DRAM.

An SRAM cell has three different states it can be in: standby when the circuit is idle, reading when the data has been requested and writing when updating the contents. The SRAM to operate in read mode and write mode should have read- stability and write-ability respectively. Both conditions become difficult to satisfy in advanced technologies because of the high degree of variability in thin CMOS transistor parameter, essentially technologies beyond 45nm. Increasing the memory size makes the required degree of reliability hard to please. This makes the first challenge for the SRAMs in advanced technology nodes.

The power consumption increases with the advanced CMOS technologies. CMOS scaling requires not only very low threshold voltages to retain the device switching speeds, but also ultra-thin gate oxides to maintain the current drive and keep threshold voltage variations under control when dealing with short-channel effects. Low

threshold voltage results in an exponential increase in the sub-threshold leakage current which contributes to the static power consumption. Charging/discharging large bit-lines' capacitance represents a large portion of power consumption during a write or read operations, which represents the dynamic power. Static and Dynamic power consumption increases with the advanced CMOS technology nodes. This make the second challenge for the SRAMs in advanced technology nodes.

On-chip cache memory consumes a large percentage of the whole chip area and power consumption and expectes to increase in advanced technologies [2]. The power consumption of SRAM varies widely depending on how frequently it is accessed; it can be as power-hungry as dynamic RAM, when used at high frequencies, and some ICs can consume many watts at full bandwidth. On the other hand, static RAM used at a somewhat slower pace, such as in applications with moderately clocked microprocessors, draw very little power and can have a nearly negligible power consumption when sitting idle, in the region of a few micro-watts.

Static RAM exists primarily as general purpose products with asynchronous interface, such as the 28 pin 32Kx8 chips (usually named XXC256), and similar products up to 16 Mbit per chip. With synchronous interface, usually used for caches and other applications requiring burst transfers, up to 18 Mbit (256Kx72) per chip. Secondary as integrated on chip as RAM or cache memory in micro-controllers (usually from around 32 bytes up to 128 kilobytes). Finally as the primary caches in powerful microprocessors, such as the x86 family, and many others (from 8 kB, up to several megabytes). To store the registers and parts of the state-machines used in some microprocessors or in application specific ICs, or ASICs (usually in the order of kilobytes) SRAM is used also in FPGAs and CPLDs (usually in the order of a few kilobytes or less).

Besides many applications require always-on memories and the power consumption issue can be dramatic. When the amount of memory became large, no particular technique is required providing that the power consumption is small compared to the

---

system global power. Besides power consumption in memories brings in the front possible thermal problems like Negative Biasing Thermal Instability (NBTI). When the amount of memory becomes large there are two basic approaches to limit the power consumption. If possible any unused memory is set into a deep sleep mode.

In a heterogeneous overlay wireless network, a mobile node (MN) with multiple wireless interfaces can attach to various networks and obtains multiple IP addresses simultaneously. To allow correspondent nodes to connect to a mobile node at anytime through any mobile nodes' IP address, an mobile node must keep its interfaces awake to receive incoming packets. Unfortunately, studies indicate that power consumption of a mobile node with multiple interfaces poses a serious problem [3], even when interfaces are idle. The energy-conserving always-on schemes for a mobile node with multiple interfaces is to only maintain one awake interface and turn off completely other interfaces to minimize its power consumption [4]. The main limitation is the necessity of a robust restoring scheme to avoid packet losses. The same complex approach has been applied to cache memories [5] where turn-off is not practicable and only a fraction of excessive power consumption is saved. The same global issue is true for real-time embedded systems [6]: the usage of SDRAM memory for working context storage enables a power consumption saving with a sufficiently fast wake-up, but memory content is preserved with self-refresh mechanism. Turning-off unused amount of memory shows limitations; a trade-off between power saving and content preservation or wake-up speed must be set. Whatever there are systems where the latter approach is event not applicable. There is then a need for true always-on but very low-power SRAM.

A practical technique to limit power consumption in embedded applications is to turn-off unuseful blocks. There is then a trade-off between the wake-up requirements, the possible reduction in consumption and the complexity of the power management controller. Wireless applications suffer now from the lack of effectiveness of the latter



technique, i.e. a robust restoring scheme to avoid packet losses. The same complex approach has been applied to cache memories where turn-off is not practicable and only a small fraction of excessive power consumption is saved. Power reduction is unfortunately essential in embedding systems so the need for true always-on but very low-power SRAM is emerging.

The PhD thesis focuses On the Always-on low power SRAM memories (essentially low dynamic power) in thin CMOS technology node CMOS 32nm and beyond. chapter 2 reviews the state of the art of the eSRAM and describes different techniques to reduce the static and dynamic power consumption with respect the variability issue. Main techniques of power reduction are reviewed with their contributions and their limitations. Chapter 3 presents a discussion about a statistical variability modeling and the variability effects on the yield. In Chapter 4 an original low power architecture based on 5T-Portless bit-cell is presented, with current mode read/write operations, as an ideal candidate for the always-on SRAM memories. A test chip implementation in CMOS 32nm of the 5T-Portless is detailed in Chapter 5 and a comparison with an existing 6T SRAM memory is presented based on simulation. Chapter 5 presents some test chip functionality results and power consumption. Finally the conclusion in Chapter 6 highlights the major contributions of the study and discusses the various simplification assumptions to see possible limitations. It is concluded affirmatively about industrial interest of the 5T-Portless SRAM for always-on embedded applications. Perspectives concern the analytical modeling for statistical behavior of SRAM as the Monte-Carlo approach is no more practicable. The migration of the 5T-Portless SRAM may be already considered in advanced nodes

---

## State of art of eSRAM

---

Moore's law, which could be interpreted as a cost reduction law, has been followed successfully for more than thirty years. It is the reduction in the size of elementary transistor (area is divided by half each 18 months) that has allowed this [7]. Nevertheless, it is now very difficult to maintain the same pace due to physical limitations related to size reduction.

The level of accuracy necessary to fabricate a circuit is necessary higher with successive technology nodes, and it is becoming critical. Small variations affect each step in the manufacturing process and these variations are gaining importance in terms of parasitic effects. When a circuit is fabricated, several characteristics are monitored in order to follow the variations of the process: a lot-to-lot variation is measured and a wafer-to-wafer variation. Only global variations are thus monitored while variations at transistor levels are local. Both global and local variations influence the circuit performances, hence the manufacturing yield [8]. The semiconductor industry can no longer count on the reduction of the transistors' size from generation to generation, therefore it requires to find new paradigms to continue the scale reduction. At each new technological node, some of the initially insignificant physical limitations become important: the dispersion of performances is now the main difficulty in designing SRAM circuits. Even if the industry manages to fabricate chips with over one billion of the smallest transistors and increasing number of inputs-outputs, pertinent applications are

paradoxally seldom found that require such an amount of these tiny devices. The development cost for each new technology node grows exponentially at each step and a pause in Moore's law seems to be inevitable [9]. At 32nm, pad rings of one thousand I/Os will be common and the circuit size (amount of transistors) necessary to fill these I/O rings will be enormous and will pose several problems such as manufacturing yield limitations, thermal issues, etc. To improve manufacturing yield, it is necessary to envision the effects of all random variations, i.e. to quantify the variability of various phenomena, and then to implement solutions to limit the effect of this variability, either at technology or design levels.

The huge systems to be invented are predicted to embed a large amount of memories. Among all types of memory, the embedded Static Random Access Memory (eSRAM) is a key product. Numerous SRAM bit-cells exist that are suitable for specific applications. The topic of the thesis focuses always-on and possibly low frequency operation eSRAMs. Whatever the variability issues remain the limiting factor that push to invent new architectures of bit-cells and memory peripherals to enable satisfying manufacturing yield in 32nm CMOS and beyond.

The state of art of eSRAM is discussed from various points of view to enlighten the hard trade-offs between the layout of the bit-cell, its operations and the additional circuits to assist the operations, the density, the power consumption and finally the success to reject the effects of variability. The discussion begins with the six-transistor SRAM (6T SRAM) as a reference bit-cell and the published techniques to limit the effect of variability. The power consumption of the SRAMs is discussed but unfortunately the variability limits the efficiency of the industrial techniques to limit the power consumption. Finally the five-transistor bit-cell is proposed as an interesting alternative but in a configuration called 5T-Portless.

### 2.1 6T SRAM

The static random-access memories (SRAM) are most widely used, due to their high performance: microprocessors may contain up to 70% of SRAMs in transistor count or area. The trend in the semiconductor market is to push for more integration and more size reduction: the development and optimization of a technological node is more and more difficult and expensive. The reduction in size of a SRAM circuit in coming nodes is nonetheless complex and it faces several limitations. The reliability of the SRAM bit-cell is degraded with ever smaller technologies and the device functionality is endangered. Designing SRAM circuits in CMOS 32nm requires technical and technological solutions to overcome the size reduction limitations, while insuring satisfactory functionality, with a guaranteed reliability so that it can be economically fabricated.

The manufacturing of a standard SRAM is fully compatible with CMOS core processes. The standard SRAM bit-cell is based on a 6-transistor arrangement: it is called a 6T-SRAM. Two CMOS inverters, formed by *PU* and *PD* transistors, are connected, one opposite to the other, and two access transistors, *PG* transistors, are added (figure 2.1). Three possible operations are: writing a bit data, retaining the bit data and reading the bit data. The operation is controlled through the word-lines that activate or block the access transistors *PG*, so that there is, or not, a connection to the bit-lines *BLT* and *BLF* that propagate the bit value from or to the bit-cell.

#### 2.1.1 Read operation

During a read operation, the bit-lines are floating and converges to the potential dictated by the bit-cell when the word-line is properly activated: one bit-line is discharged to ensure the high speed and low power read operation. The voltage between bit-lines' potentials is sensed by a voltage sense amplifier *SA*.

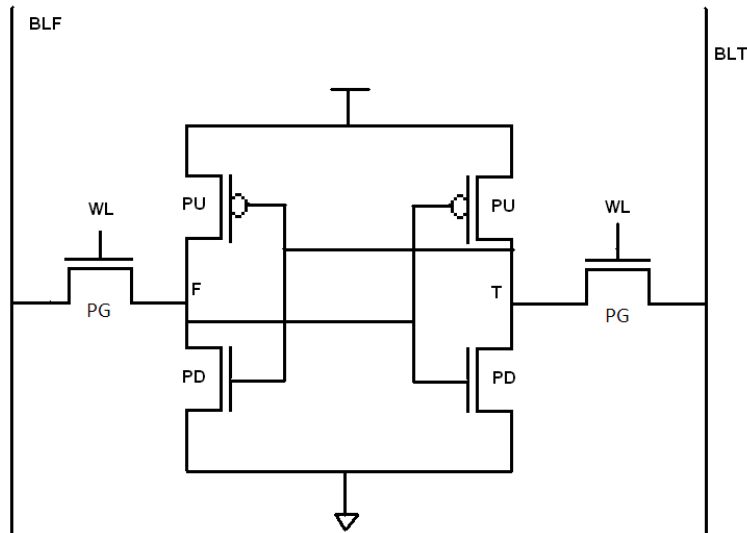


Figure 2.1: 6T SRAM bit-cell

The read operation is the most destructive operation with regard to the data integrity (both access transistors are turned on and draw charges from the coupled inverters). The indicator of the SRAM bit-cell read stability is the Static Noise Margin (**SNM**) [10]. **SNM** is a figure of merit that enables the evaluation of the stability of the memory bit-cell under static conditions. **SNM** is related to the maximum size of the box that can be drawn in the memory static transfer function (figure 2.2). Such a curve is called a butterfly curve. The **SNM** can be also evaluated by a DC simulation. In figure 2.3 the **SNM** corresponds to the  $V_n$  value that flips the bit-cell data, when the bit-cell is in a read mode i.e  $WL = V_{DD}$  and  $BLF = BLT = V_{DD}$ . This method is more efficient than the butterfly curve to evaluate the **SNM**. It allows having a numerical value that can be used to do parametric simulations or Monte Carlo simulations. However the butterfly curve has a graphical interest, it allows to have a direct comparison between different architectures or to highlight graphically the improvements or degradations of the bit-cell stability. The SRAM is affected by variations related to the Process, the supply Voltage and the local Temperature (**PVT** variations). Figure 2.4

## 2.1 6T SRAM

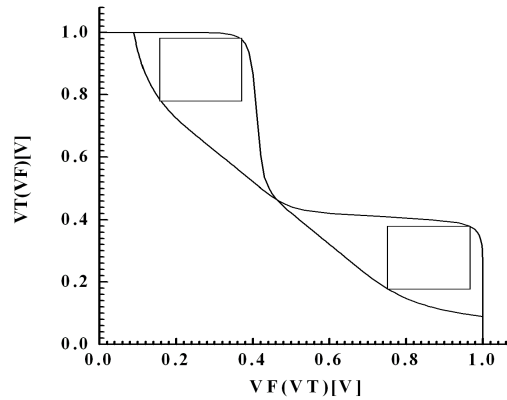


Figure 2.2: 6T Butterfly curve (32nm and typical condition simulation)

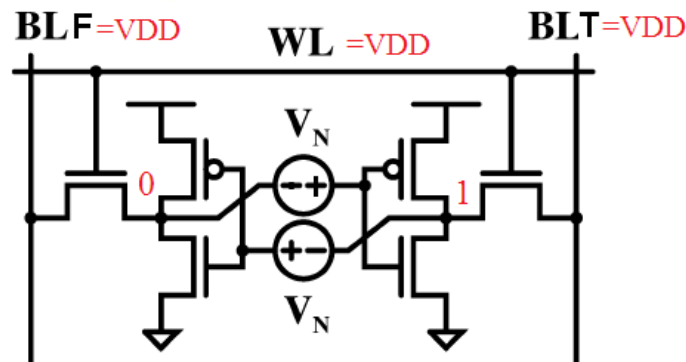


Figure 2.3: SNM evaluation by simulation

represents the variation effects on the **SNM** due to the process, the supply voltage and temperature, respectively, evaluated by simulation for the SRAM bit-cell in figure 2.1, in bulk CMOS 45nm.

Figure 2.5 shows Monte Carlo simulations, obtained with Mastar [11] for different bit-cell sizes. Decreasing the bit-cell area affects also the read stability because the process variations increase with the transistor shrinking: according to (2.1), the standard deviation  $\sigma_{V_{th}}$  of the threshold voltage  $V_{th}$  of a transistor depends on transistor length (**L**) and width (**W**), where  $A_{V_{th}}$  is a technology-depend parameter [12]. It is

clear that the  $V_{th}$  variation increases with the transistor dimension shrinking. This has a direct impact on the SRAM bit-cell parameters (figure 2.6). Experiment has shown that generally the **SNM** under PVT is roughly distributed as a Gaussian distribution with a mean value  $\mu_{SNM}$  and a standard deviation  $\sigma_{SNM}$ .

$$\sigma_{V_{th}} = A_{V_{th}} \times \sqrt{\frac{1}{W \times L}} \quad (2.1)$$

The impact of the variability is destructive on the read operation. In case of a typical

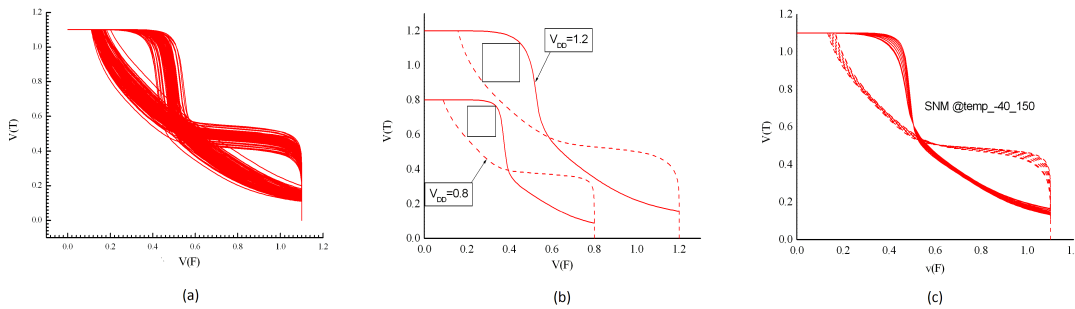


Figure 2.4: Simulated SNM-curve for a CMOS 45nm SRAM under (a) process variations, (b) power supply variations and (c) temperature variations between  $-40^{\circ}\text{C}$  and  $+125^{\circ}\text{C}$

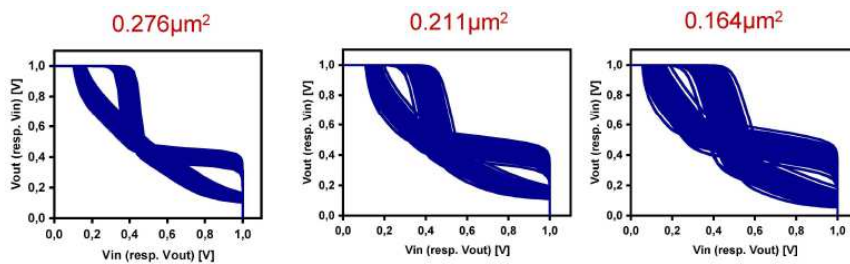


Figure 2.5: Butterfly curve for different sizes of 6T bit-cell in 32nm (simulations by Mastar)

process (figure 2.7.(a)) read and write operations are made correctly but if a device mismatch induce a change in the bit-cell transistors characteristics, as it is the case in

## 2.1 6T SRAM

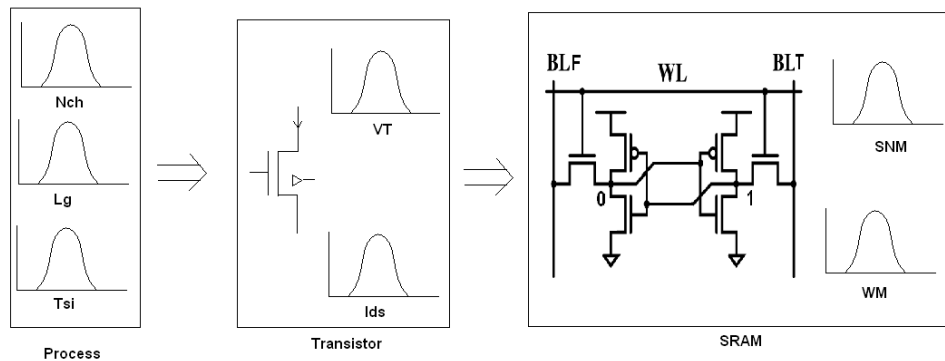


Figure 2.6: Tree of variation propagation from process to transistor and circuit

figure 2.7, the bit-cell data can be lost (figure 2.7.(b)) (**destructive read operation**). The stability concept is the bit-cell ability to keep the data value during the read oper-

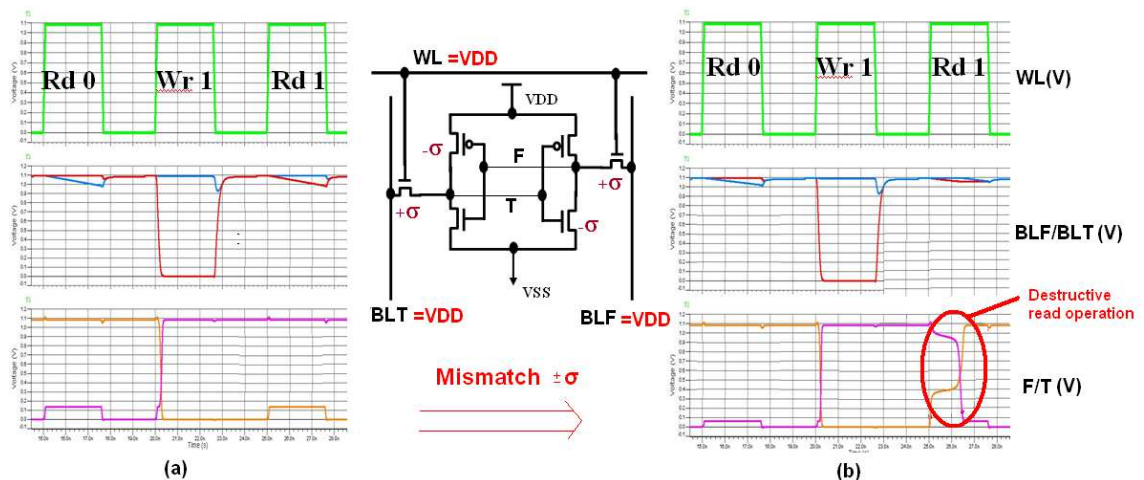


Figure 2.7: Transient simulation result of read and write operation : (a) simulation without mismatch, (b) simulation with device mismatch

ation despite of variability. The bit-cell must be enough stable to maintain the internal node voltage despite the voltage drop caused by the bit-lines voltage. However the bit-cell must also be weak enough to ensure the write operation. The read and write margins must be set as a trade-off.



### 2.1.2 Write operation

The write operation in a 6T bit-cell is explained in figure 2.8, where node **T** is initially at 1 and **F** is at 0. 0 is written into **T** by pulling the bit-line **BLT** to GND and turning on the pass gate (**PG**) by setting **WL** to  $V_{DD}$ . The data is then injected into the bit-cell. The memory write-ability is characterized by the write-margin (**WM**). The write margin (**WM**) is evaluated with a DC simulation: it is the minimum voltage difference between the bit-lines **BLT** and **BLF** able to change the bit-cell data. The write margin (**WM**) parameter characterizes the bit-cell write ability. As a result of the **PVT** variations, **WM** may not present enough margin to ensure a safe write operation. In a Slow NMOS Fast PMOS corner (**SF**) (figure 2.9), the **PG** transistor becomes too weak compared to the **PU** transistor, so the node to 1 is then difficult to pull down to 0 what means a **Write failure**.

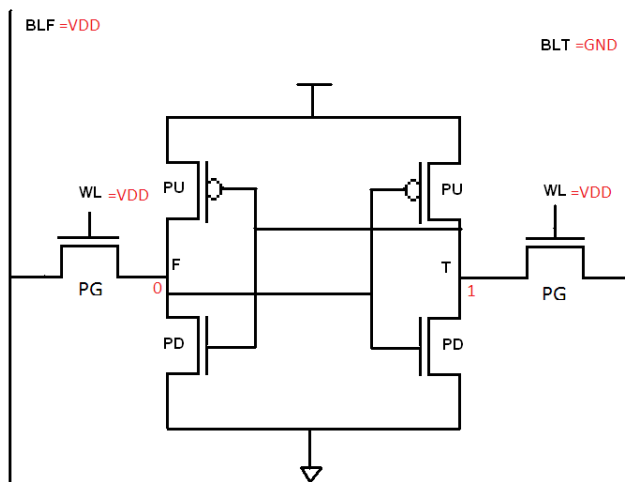


Figure 2.8: Write operation in 6T Bit-cell

In advanced technology nodes, PVT increasing variability affects also the write margining (figure 2.6). The difference between **WM** and **SNM** are reduced. As explained in next section, the SRAM operation requires that **WM** and **SNM** do not overlap. The trade-off between read stability and write ability becomes more and more difficult to

## 2.1 6T SRAM

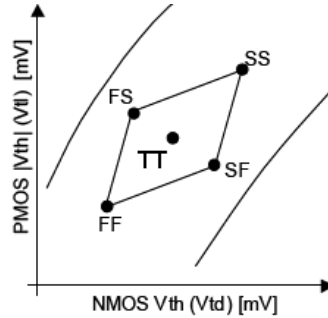


Figure 2.9: Process corners according to the NMOS and PMOS  $V_{th}$  values

set. The bit-cell sizing is set in order to target SNM and WM values. As it is developed in next section, these two parameters are antagonist regarding the bit-cell sizing.

Variability is the topic of large research efforts [10]. The issue is seen from a characterization point of view [13, 14, 15]. Other papers in literature focus the demonstration of solutions to overcome the variability effects. In most cases the efforts are dedicated to one bit-cell particularly [16, 17]. The present manuscript follows the same idea but after an effort to select a best bit-cell candidate. The state of the art will not cover the attempt to use advanced transistors [18, 19, 20] or non-bulk CMOS technologies [21, 22, 23]. The discussion is limited here to standard CMOS. In [24] the variability on  $V_{th}$  is corrected by active body-biasing inside a convergence loop: this technique affects all the transistors on the die and may not be considered for embedded systems.

### 2.1.3 SRAM bit-cell sizing

In the 6T SRAM bit-cell, a good read-margin implies a stronger pull-down transistor (**PD**) than the pass-gate transistor (**PG**), i.e. a large ratio  $\beta = \frac{(\frac{W}{L})_{PD}}{(\frac{W}{L})_{PG}}$ . The ratio  $\alpha = \frac{(\frac{W}{L})_{PG}}{(\frac{W}{L})_{PU}}$  is necessarily high to guarantee the write-ability as the pull-up transistor (**PU**) is set to a minimum size. The **PD** transistor maximum size is limited for a given bit-cell area. To obtain a large  $\beta$  ratio inclines to decrease the **PG** transistor, hence

to decrease the  $\alpha$  ratio i.e. decrease the write-margin (**WM**). As shown in figure 2.10 regarding the  $\alpha/\beta$  ratio, for a given bit-cell area, decreasing the **WM** (write ability) corresponds to increasing the **SNM** (read stability). Read-margin and write-margin must be set as a trade-off [25].

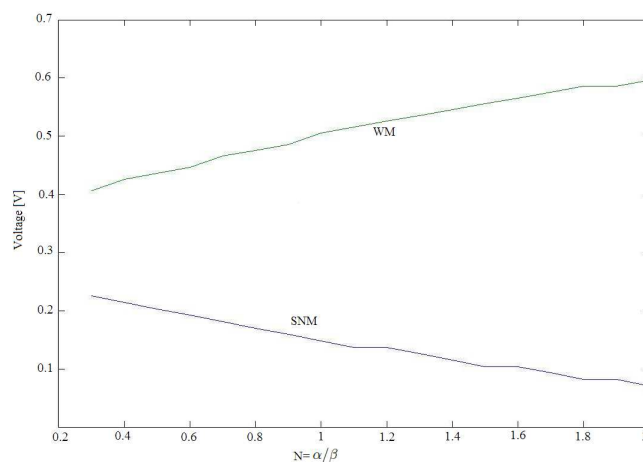


Figure 2.10: **WM** and **SNM** versus the ratio  $N=\alpha/\beta$

In order to optimize the trade-off between SNM and WM, some potential solutions exist at the periphery level. The first one is to set enough  $\beta$  ratio in order to have a good stability. The non favorable value set for the ratio  $\alpha$ , requires additional circuitry to help the write operation. This is called a **write assist** circuit. The second solution is to set the  $\alpha$  ratio to have enough write margin and add a set up in the periphery to help the read operation. This technique is called a **read assist**. Write assist, read assist and other design solutions are detailed in next section. The design solutions are efficient to reject the effect of variability and reduce the power consumption but they require generally an additional silicon area and/or a power consumption penalty. Again a trade-off must be set.

## 2.1 6T SRAM

### 2.1.4 Retention mode

In retention mode, bit-lines are precharged to  $V_{DD}$  and the WL is set to  $GND$ . The data is then stored into the bit-cell. In this mode the bit-cell must be continuously supplied to maintain data and compensate for the leakage current  $I_{leak}$ . In this mode the power consumption is equal to  $I_{leak} \times V_{DD}$  which is called the **Static power consumption**. Static power consumption increases with the supply voltage  $V_{DD}$  so the technique usually used to reduce the power consumption is the  $V_{DD}$  scaling. As shown in figure 2.11 the leakage depends exponentially on the power supply  $V_{DD}$ .

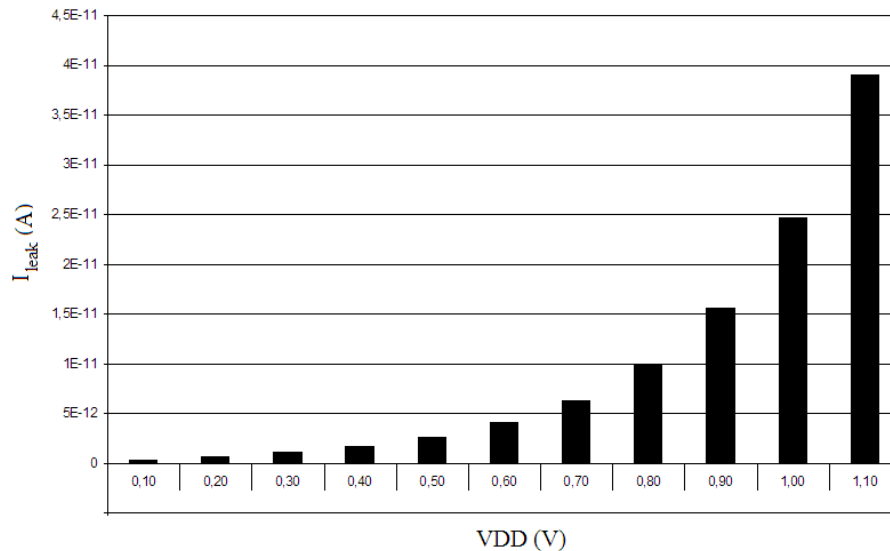


Figure 2.11: 6T SRAM bit-cell leakage versus  $V_{DD}$  in CMOS 32nm

The 6T SRAM bit-cell necessitates a minimum supply voltage to maintain the data. It is called the Data-Retention Voltage (DRV) [26]. Like SNM and WM, the DVR parameter varies with the PVT variations. The  $V_{DD}$  scaling reduces the static power consumption but insufficient DRV can cause a retention failure. The DRV statistical distribution must be studied to estimate the minimum value above which the data can be retained reliably [27].

Body biasing design is another efficient technique to reduce the leakage current.

The leakage depends to the value of the threshold voltage  $V_{th}$  of a transistor. According to (2.2) [28], the threshold voltage can be increased by changing the voltage value of the transistor's body. That technique is called the body biasing.

$$V_{th} = V_{FB} + (\Phi_{s0} - \Delta\Phi_s) + \gamma\sqrt{\phi_{s0} - V_{BS}} \left(1 - \lambda\frac{X_d}{L}\right) \quad (2.2)$$

In next section VDD scaling and body biasing techniques are compared. This technique requires generation of different supply voltage levels. Additional circuitry area is needed and additional power consumption is engendered. The interest of these techniques depends potentially on the dedicated memory application.

Variations of gate length (L), gate width (W), gate oxide thickness ( $T_{ox}$ ), and the channel dopant concentration (Na) increase with the technology scaling, thus the random variation of the MOSFET threshold voltage increases while its value diminishes to retain the device switching speed with the technology scaling. Variability on  $V_{th}$  has been demonstrated to vary more rapidly since CMOS 90nm [29]. The SRAM functionality margin is negatively affected [30, 31]. The transistor leakage current increases with technology scaling and its values can affect the SRAM data in retention mode. This is an additional but indirect limitation [32] that sets the minimal value of power supply in retention mode (DVR).

It appears that there are 3 ways to lessen the fluctuations: namely reducing the technology-dependent parameters, increasing the transistor geometrical factor or introducing design-level improvements. The latter is related to design options. The former is related to technology process. The geometrical factor is incompatible with Moore's law and ITRS roadmap. The only scalable solutions, apart from an improved technology (which will come in time), are based on design improvements.

Next section reviews the existing design techniques to reduce the power con-

## 2.2 Power consumption and variability

---

sumption and reject the effects of variability. It details different solutions that can be applied at bit-cell, bit-cell array and at periphery level respectively.

## 2.2 Power consumption and variability

Power consumption in memories is the sum of dynamic and static power. Dynamic power is the power needed to ensure different operations (read, write, decoding. . .). It depends on the number of operations made in a working time. The static power, which is the power due mainly to the transistors' leakage, is always present as long as the memory is biased. The power consumption of a chip can be modeled by (2.3) where  $C$  is the bit-lines and parasitic effective capacitances,  $V_{DD}$  is the supply voltage,  $I_{leak}$  the full chip leakage current and  $f$  the operating frequency of the circuit.

$$P = C \times V_{DD}^2 \times f + I_{leak} \times V_{DD} \quad (2.3)$$

As discussed previously, the total power is a function of  $V_{DD}$ . The mostly used technique to reduce the power consumption is  $V_{DD}$  scaling. In advanced CMOS technology nodes, transistor's leakage increases exponentially due to the rapid scaling of transistor channel and length for each successive technology [32]. Additionally the size of the memories continues to increase, thus the static and dynamic power consumption of the memory becomes more and more important.

### 2.2.1 Variability and consumption of a SRAM bit-cell

In retention mode, leakage is the main power consumption. The memory sleep mode consists in decreasing the matrix voltage (bit-cells' supply voltage) and/or switch-off the periphery supply voltage. The major contribution to leakage is the bit-cell array. The leakage depends on the bit-cell architecture. In [33] a comparison between 6T, 8T

and 9T bit-cells in terms of Static Noise Margin  $SNM$ , Write Margin  $WM$ ,  $DRV$  and leakage is presented. Figure 2.12 shows a comparison of static and dynamic power for 6T, 8T and 9T structures respectively, obtained by simulation. Each bit-cell has been layouted with minimal area in 32nm standard CMOS.

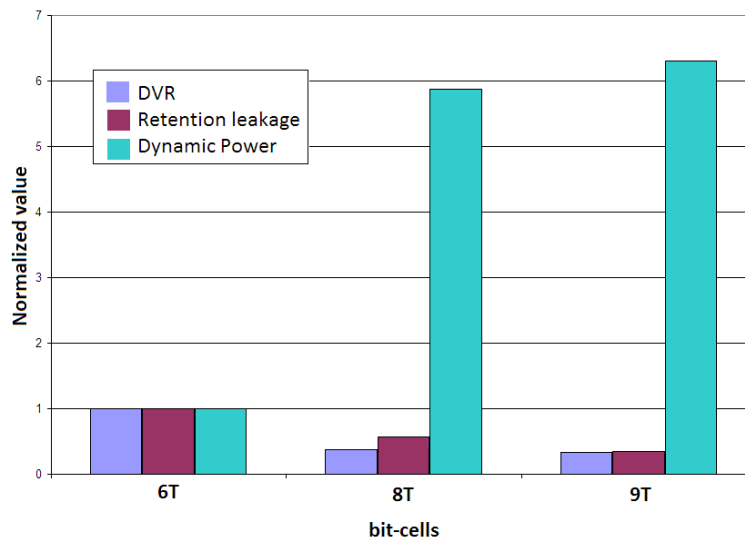


Figure 2.12: DVR, Leakage and dynamic power comparison

Since 9T is more stable than 8T and 8T is more stable than 6T,  $DRV$  of 9T is the lowest and thus offers less leakage than the other bit-cells. However 9T has more parasitic capacitances so its dynamic power is larger. The memory global consumption depends on the type of dedicated application. If the memory is frequently operating and has short retention time, dynamic power is the major contributor to the memory global consumption and 6T SRAM bit-cell is then favorable. If the memory is not frequently operating and period of retention is the major state in the memory working time, then leakage is the major contributor of the full chip power consumption. In this case bit-cells like 9T or 8T are the best candidate.

Leakage, as discussed previously, can be scaled according to  $V_{DD}$  or acting on the transistor's body voltage. Three techniques exist to reduce the leakage (figure 2.13)

## 2.2 Power consumption and variability

- Reverse Body Bias (RBB): the PMOS transistors' body ( $V_{DDs}$ ) initially connected to  $V_{DD}$  is supplied with higher voltage and NMOS transistors' body (GNDs) initially connected to GND is supplied with a lower voltage. The initial power voltage ( $V_{DD}$  and GND) are kept unchanged.
- Source Body Bias: the body power supplies ( $V_{DDs}$  and GNDs) are kept unchanged but  $V_{DD}$  is decreased and GND is increased.
- $V_{DD}$  scaling (VS): both power supply ( $V_{DD}$ ) and body power supplies ( $V_{DDs}$ ) are reduced.

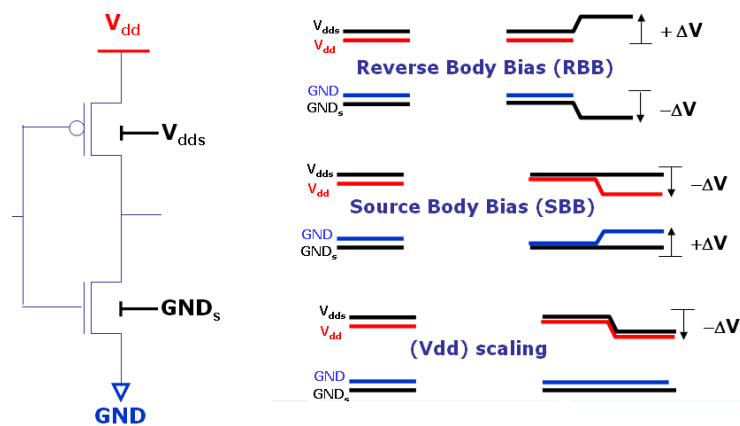


Figure 2.13: Most popular leakage reducing techniques

The most efficient technique to reduce the leakage is the source body bias (SBB) as shown in figure 2.14, but this technique reduce considerably the bit-cell power supply and the retention capability. The most stable solution regarding the data retention is the reverse body bias (RBB). It offers a reduction in power supply without scaling the bit-cell voltage supply.



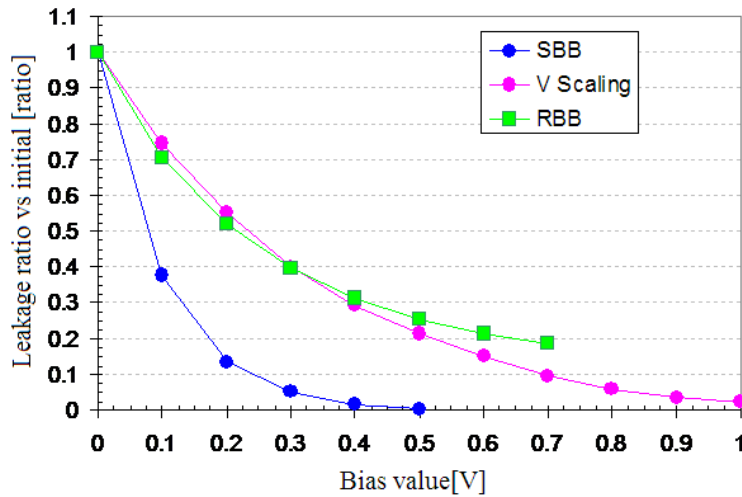


Figure 2.14: simulation results of the reducing leakage techniques

Dynamic power can be reduced also by decreasing  $V_{DD}$  but this can arise problems in the read stability by reduction of the Static Noise Margin ( $SNM$ ). Write ability can also be damaged by reduction of the Write Margin ( $WM$ ) [34]. Read assist and write assist can help to ensure safe write or read operations at low  $V_{DD}$  respectively.

There are 3 main write assist techniques:

- Supply down scaling (Figure 2.15): it consists in reducing the bit-cell supply to  $V_{DD} - \Delta V$  to obtain a less stable bit-cell. PU transistor is weakened versus PG, so the write ability is improved.
- Negative bit-line (Figure 2.16): the bit-line BL is set to  $GND - \Delta V$  to create a stronger PG transistor and enable to flip the bit-cell easily.
- World line boosting (Figure 2.17): PG can be stronger by increasing WL voltage, the current sinking is more important and the write operation is made rapidly.

These techniques allow to perform write functionality at low  $V_{DD}$  supply so the dynamic power is reduced. Reducing  $V_{DD}$  affects also the read stability.  $SNM$  decreases as far as  $V_{DD}$  declines. Figure 2.18 shows the simulated 6T bit-cell butterfly curve for

## 2.2 Power consumption and variability

---

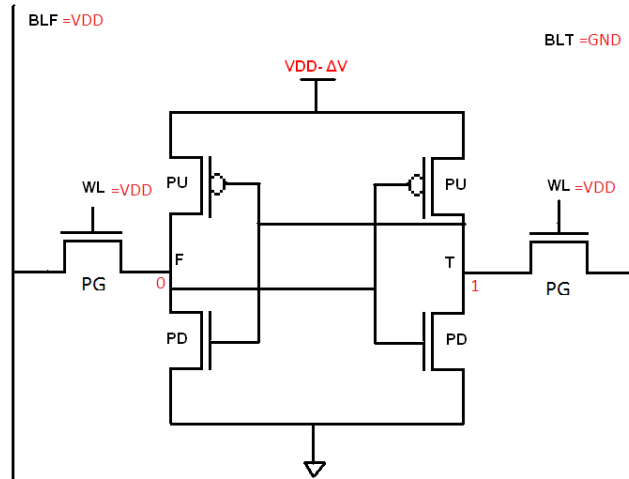


Figure 2.15:  $V_{DD}$  scaling

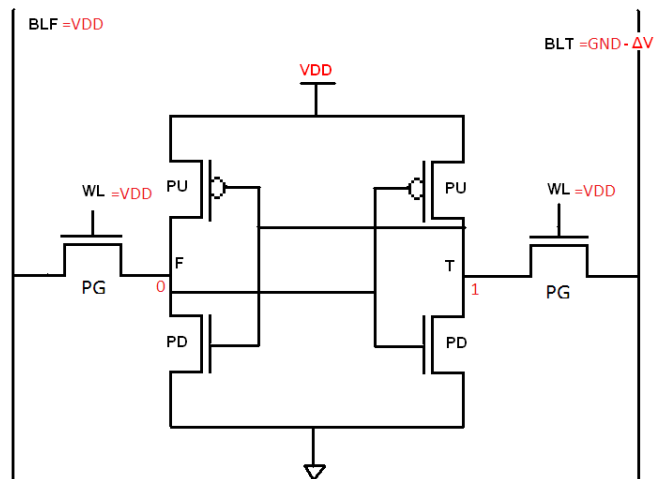


Figure 2.16: Negative bit-line



## 2.2 Power consumption and variability

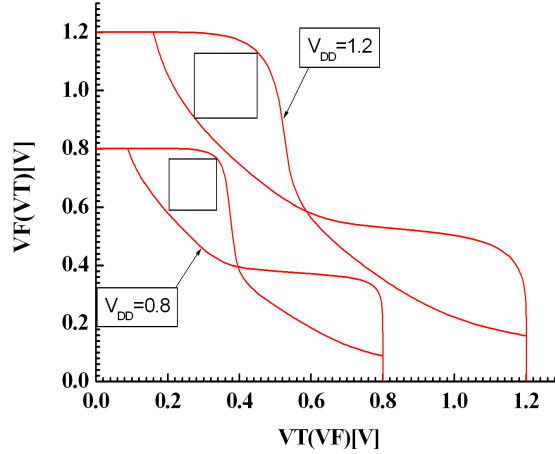


Figure 2.18: simulated 6T butterfly curve for  $V_{DD}=1.2V$  and  $V_{DD}=0.8V$

sense amplifier offset,  $V_{SAO}$  ( $\Delta V_{BL} \geq V_{SAO}$ ).

Power consumption in read operation is evaluated by (2.4) where  $\Delta V_{BL}$  is the bit-line voltage difference and  $P_{SA}$  the power consumption of the sense amplifier (SA). With transistor shrinking, PVT variability becomes important and  $V_{SAO}$  and  $\Delta V_{BL}$  variability increases. Figure 2.20 presents a Monte Carlo simulation of PVT effects on a 32nm minimal area 6T bit-cell with respect to the sense amplifier. As PVT increases in amplitude, an overlap of  $\Delta V_{BL}$  and  $V_{SAO}$  is detected meaning a loss in manufacturing yield. So the required margin  $\Delta V_{BL}$  must be more important to insure the functionality and a satisfying manufacturing yield. According to (2.4) dynamic power consumption may not be reduced effectively.

$$P = C \times \Delta V_{BL} + P_{SA} \quad (2.4)$$

In [36] a statistical method to determine rigorously the bit-line discharge time is developed, but the non-Gaussian distribution of  $\Delta V_{BL}$  makes it difficult to estimate accurately time margins. Margins are always set arbitrarily what degrades the power

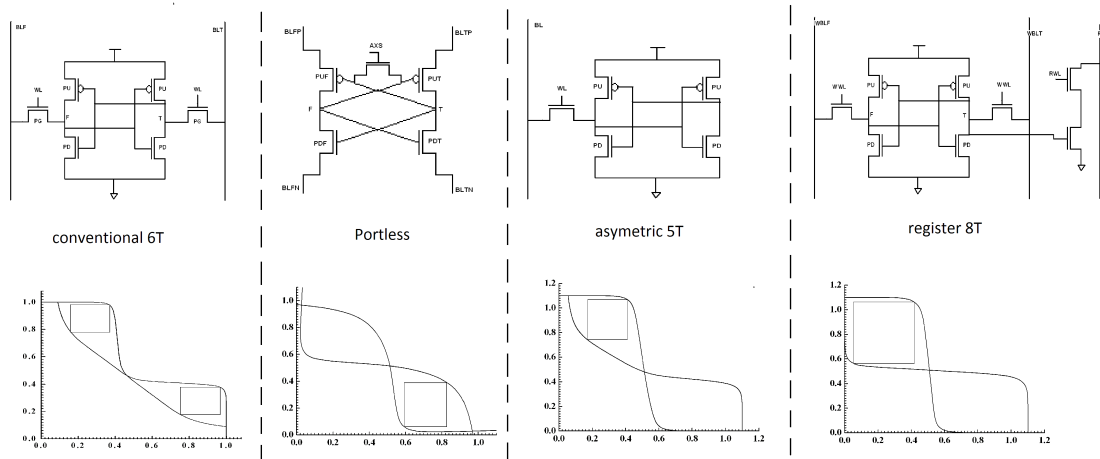


Figure 2.19: SNM simulation comparison for 32nm bit-cells

consumption and circuit performances.

The largest contribution to the dynamic power in SRAM memory is related to bit-lines, when they are discharged and charged during write/read operation respectively. The dynamic power (2.3) becomes larger with the memory size. To reduce the power consumption and read/write delays, bit-cells' columns are divided in a multiplexed structure. This reduces the bit-line effective capacitance, but in read/write operations both selected and unselected bit-cells are sinking current. The read current ( $I_{read}$ ) is consumed  $M$  times where  $M$  is the number of Mux (Figure 2.21). The unselected bit-cells which are in retention mode are disturbed by the read/write operation because their  $PG$  transistors are activated. In [37] a technique of charge recycling is developed, to limit the waste of power in read/write operation by reducing the bit-line swing during write operation and recycling the charge stored in bit-lines capacitances. This technique is quite effective to reduce the power consumption but the read/write errors are increasing when reducing the voltage swing, particularly in the advanced technologies where variability is augmented.

## 2.2 Power consumption and variability

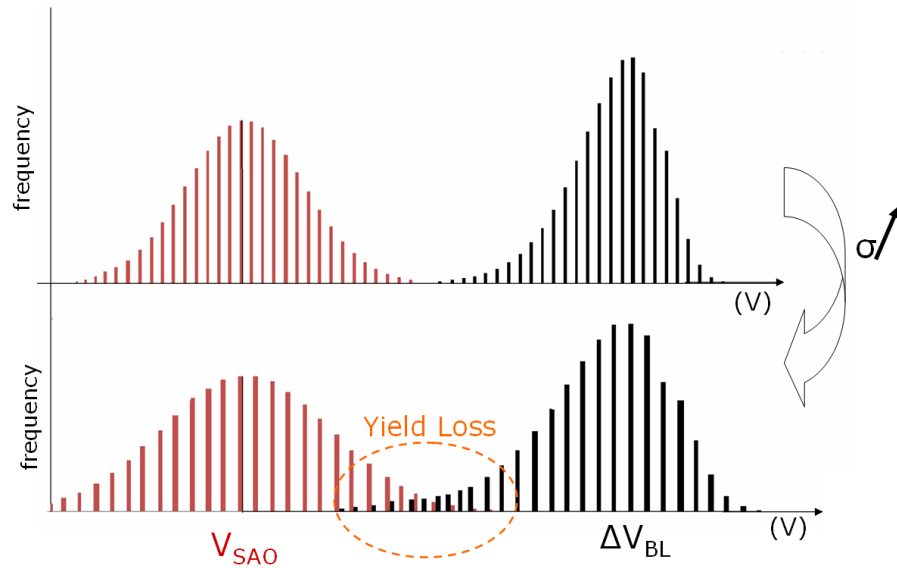


Figure 2.20:  $\Delta V_{BL}$  and  $V_{SAO}$  distribution overlapping (Monte Carlo simulations)

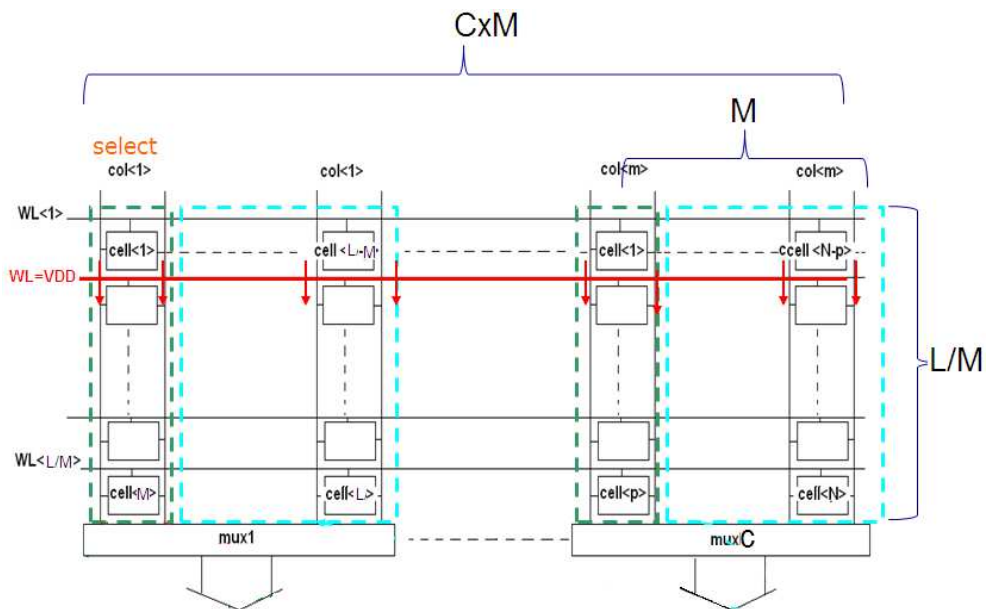


Figure 2.21: 6T bit-cell Multiplexed structure

## 2.2.2 SRAM Periphery

The SRAM periphery is the logic circuitry required to ensure the address decoding, data sensing and control of the different memory operations. In periphery the leakage is not a major portion of the power consumption. Unlike bit-cell matrix, the periphery can be switched-off during retention mode and consequently the leakage contribution is practically null. Dynamic power is essentially consumed in decoders and I/Os. During a decoding operation address bits are changed randomly and the worst case is when all address bits are changed simultaneously. To minimize the dynamic power, a technique of pre-decoding is experimented [38]. This technique aims to partially decode the address to minimize the number of switched signals in long decoder wires, so the waste in power is limited. Sense-amplifier (SA) consumption is also considered and in [39] an example of low power sense amplifier is presented. This structure allows to obtain a low voltage swing and high speed. The main problem of the differential sense-amplifier remains the offset which increases as the variability increases, so the required bit-line differential voltage margin,  $\Delta V_{BL}$ , increases and consequently the power consumption increases too.

## 2.2.3 Conclusion

The PhD objectives are to propose and design a SRAM architecture for true always-on operation and able to survive to the increasing variability of coming technology nodes.

Many techniques to reduce the power consumption in memories are discussed in previous section. PVT variability has a negative impact on power consumption because all power reducing techniques are limited by yield drop due to variability. Although some additional structures can help to reduce the power consumption, they require additional circuitries that consume energy and silicon area. As discussed previously, the largest power is dissipated in the array matrix. The main contributor to leakage is the bit-cell. The major part of the dynamic power is consumed in bit-lines during

## 2.2 Power consumption and variability

---

read/write operation.

- There is a need for a low leakage bit-cell which allows low dynamic power, without degrading stability. It is essential for the PhD objectives.
- Moreover the voltage sense operation is limited by constraints on the voltage sense amplifier offset ( $V_{SAO}$ ). The bit-lines capacitance charge and discharge are associated to power consumption difficult to decrease. An alternative technique must be considered.
- The usefulness of assist circuit is based on the possibility to tune the power supply without impact on the bit-cell operations. The many trade-off in the design are even more complex to define. A safe approach is to be demonstrated.

We come to the conclusion that a current mode operation is a candidate to solve most of the previous limitations. The 5T-Portless bit-cell has already been presented for this major improvement. Unfortunately literature indicates that the Portless is not industrially interesting beyond 45nm.

Chapter 4 details a **new 5T-Portless SRAM structure** where the technology limitations has been overcome thanks to a new set of operating points. The bit-cell is less leaky than the 6T SRAM and permits to have a read/write operation based on original current mode operations called the **hard-line copy**.

The design of the 5T-Portless bit-cell faces the same ever limitations with respect to variability. The work presented in chapter 4 has led to a reflexion about an alternative method to Monte-Carlo simulation. In chapter 3 is presented a tentative modeling approach to take variability into account prior to design effort. This chapter is isolated from the Portless issues and details a study of variability modeling developed for the 6T SRAM margins. the relations between margins and yield is discussed with a projection in advanced technology nodes.



Chapter 5 details a test chip design and presents a comparative simulation results with 6T-SRAM in standard 32nm CMOS. Few experimental results are detailed in Chapter 5.

---

## Modeling for variability

---

In a CMOS technology node, process variations are quantified as a mean value and a standard deviation of a given transistor physical parameter (transistor geometry  $L$  and  $W$ ,  $N_a$  dopant channel concentration, gate oxide thickness  $T_{ox}$  . . . ). Indeed variations at circuit level are not estimated using a direct or explicit method, i.e. functions like  $P = f(L, W, N_a, T_{ox} \dots)$ , where  $P$  is a given functional parameter, like the SNM for the SRAM bit-cell for example. Such functions are difficult to determine but they would ease the design of circuits with an implicit consideration of variability effects. The design of any sub-block of a large circuit is more efficient when it is based on solid specification values. In the case of SRAM, the specifications are for example SNM, WM . . . , i.e. circuits parameters as opposed to transistor parameters and technology parameters.

In fact a designer develops solutions based on experiment in a trial-correction manner. The effects of variability are evaluated throughout expensive Monte Carlo simulations. A Monte Carlo simulation is a set of a predefined simulation scheme where the physical parameters of the transistor models are tuned randomly. The circuit parameters values change over the simulation iterations. The distribution of a given parameter  $P$  values is approximated generally as a Gaussian shape of mean value  $\mu_P$  and standard deviation  $\sigma_P$ . These representations of the cell parameters are used by the designer to set margins to satisfy a manufacturing yield target. The design exercise

may be time consuming in the case of intricate trade-offs between the various margins. The designer has no way to prove that a trade-off is optimal. Moreover the parameter distributions are not necessarily Gaussian. This introduces inaccuracies and a satisfying trade-off for a designer may reveal actually a failure with respect to manufacturing yield.

In advanced CMOS technology nodes, larger margins in SRAM bit-cell are required to face variability increases. There is a penalty in bit-cell performances and density. In [40] authors are engaged to increase the SRAM bit-cell supply voltage to limit the sensitivity of the bit-cell to variability. There is a direct penalty on power consumption on one hand, and there is a severe limitation to this method with advanced technology nodes on the other hand. There is a need for an alternative design paradigm and the parameter functions  $P$  as proposed here-above seem to be a first step. It is now proposed a tentative method to explicit such parameter functions  $P$  and yield pertinent values for the SRAM margins prior to the design effort.

## 3.1 Yields and margins in SRAM

Usually SRAM margin prediction is difficult to perform. It is a trade-off between performances and reliability and manufacturing yield. A design performance is the measurement of the guarantee of a targeted yield. It means to achieve enough SRAM margins, no more no less. The manufacturing yield concept may be defined in relation to the probability to have a wrong operation (read, write or retention) in a SRAM circuit. It is considered globally at a system level. Unfortunately margins are set at the bit-cell design level. The main problematic in the circuit design is the ability to quantify margins at the cell design level that are required for a given chip manufacturing yield while featuring maximal performances, i.e. to make the ideal optimization.

A SRAM manufacturing yield may be quantitatively appreciated with an explicit value, namely the Acceptable Quality Level (AQL), or implicitly in terms of Gaussian

### 3.1 Yields and margins in SRAM

---

distribution. AQL means a maximum number of defective bit-cells per billion of fabricated bit-cells. An issue is to translate this maximum number of defective bit-cells into quantitative values for acceptable fluctuations, and to work out solutions to meet the manufacturing yield constraint. For example a typical AQL value for 10 Megabit of SRAM bit-cells could be 100 ppm. If one million of circuits of 10Mb bit-cells is considered, it is not allowed more than 100 defective bit-cells globally thus the AQL evaluation in (3.1).

$$\frac{100 \text{ defective bit-cells}}{10^6 \text{ circuits} \times 10 \cdot 10^6 \text{ bits}} = 10^{-11} \quad (3.1)$$

The manufacturing yield may also be expressed as the necessary distribution of good circuits. The previous AQL value of  $10^{-11}$  is translated into a requirement for functional circuits up to  $7\sigma$  from the nominal process values. Improvements in SRAM design are sometimes presented in term of gain in sigmas. In literature it means that the proposed improvement enables to save initially bad circuits up to a certain number of sigma from the nominal process values.

In this chapter the example of the SRAM read operation is detailed and the relationship between the delay margin and the reading yield is explicated. The reading yield (RYL) is the probability to have a read success in a memory of  $\mathbf{N}=n \times m$  bits (figure 3.3) with a given delay margin needful for bit-lines discharging. The delay must be long enough to ensure a targeted yield but it must be as short as possible to ensure maximal performances: reducing power consumption and guarantee a good operation speed.

By an abuse of language, the read or write yield refer to the probability of a fault instead of the probability of success. Of course one quantity translates easily into the other. From now on, it is detailed an explicit expression of the read yield in a SRAM

bit-cell as the probability of a faulty read operation.

A faulty read operation corresponds to an error while sensing the data from one or more bit-cells of a selected word-line. A bit-cell read error is caused essentially by an insufficient bit-line voltage difference  $\Delta V_{BL}$  at the input of the sense amplifier (SA). The voltage difference  $\Delta V_{BL}$  should be more important than the sense amplifier offset value ( $V_{SAO}$ ) [41]. Unfortunately PVT variability trends to spread  $\Delta V_{BL}$  values and  $V_{SAO}$  values (figure 2.20). An overlapping of values is predictable and the read operation in this case is faulty.

The read mode operation leads to various phenomena inside the bit-cell. For example a glitch may be observed on the bit-line voltage along with the rising edge of the WL signal (figure 3.1). The read current is also perturbed by the leakage current of the passive bit-cells connected to the same column. So modeling the read mode operation is quite complex. A simplified model is considered here (figure 3.2) what is sufficient to illustrate the modeling approach for variability. All the neglected phenomena can be modeled in the same maner as what is detailed in the next section.

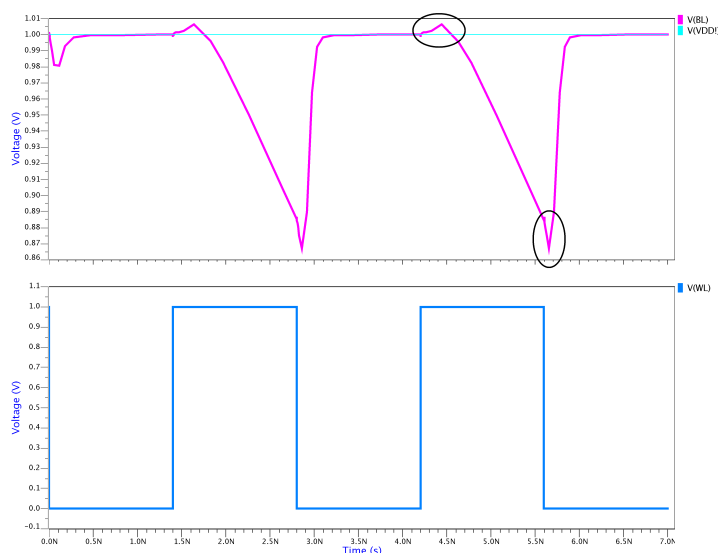


Figure 3.1: Transient simulation of the bit-line discharge in read operation of a 6T SRAM in CMOS 32nm

### 3.1 Yields and margins in SRAM

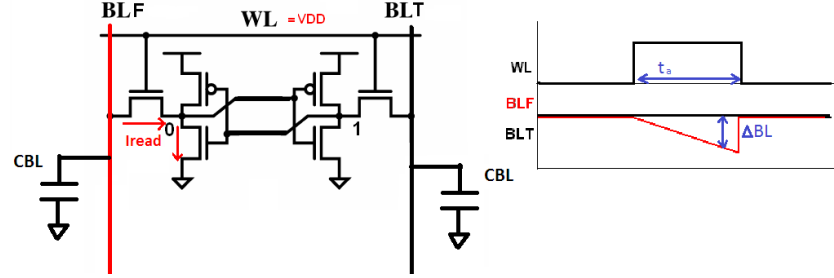


Figure 3.2: Bit-lines' voltage difference during discharged time  $t_a$

In order to avoid this situation, the designer play usually with the bit-line discharge time  $t_a$ . The problematic is how much delay time is necessary to avoid the  $\Delta V_{BL}$  and  $V_{SAO}$  values overlap if a huge number of bit-cells is fabricated. Another problematic is to determine what bit-cell parameter is the most efficient to solve the variability issue at hand.

It is considered the read operation in a memory of  $\mathbf{N}=\mathbf{n} \times \mathbf{m}$  bits (figure 3.3). Let  $B$  be the random variable that represents the number of wrong by read bits and  $P$  the probability to have a faulty read operation on a sole bit of a column. Mathematically  $\mathbf{RYL} = P(B \geq 1)$ .  $B$  is a binomial distribution.  $\mathbf{RYL}$  can be calculated as (3.2).

$$\begin{aligned}
 P(B \geq 1) &= 1 - P(B = 0) \\
 &= 1 - C_m^0 P^0 (1 - P)^m \\
 &\approx 1 - (1 - m \times P) \\
 &= m \times P
 \end{aligned}$$

(3.2)

For a targeted  $\mathbf{RYL}$  value, the probability  $P$  must be:

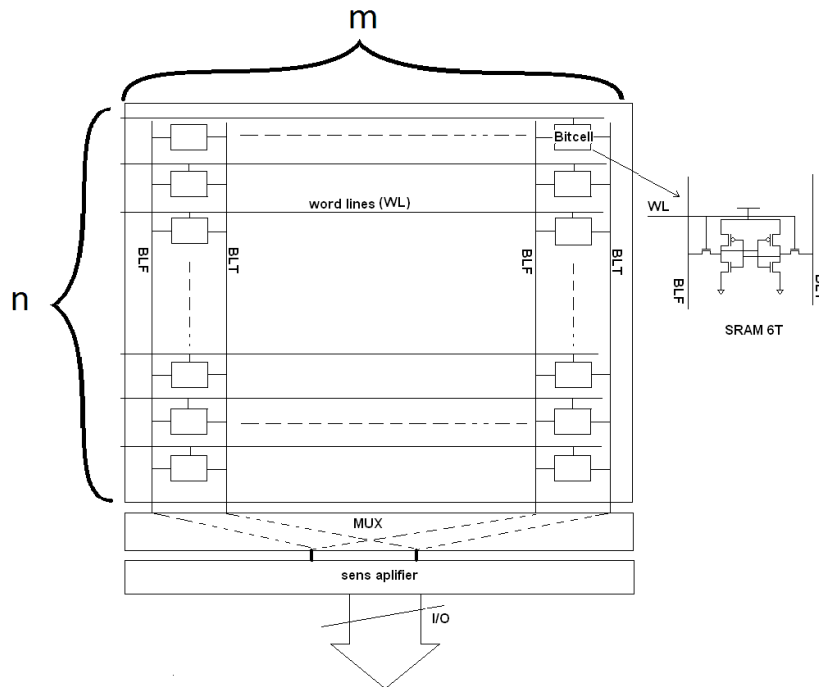


Figure 3.3: SRAM array with Y decoders and sense amplifier

$$P = \frac{\mathbf{RYL}}{m}$$

The approximation in (3.2) is valid for  $0 \leq P \leq 1/m$ . Let  $p$  be the probability to have a faulty data sensing from a single bit-cell (namely a wrong by read bit). A similar line of thinking applied to  $m$  columns can be applied to  $n$  bit-cells of one column. With the same assumption  $0 \leq p \leq 1/n$ :

$$p = \frac{P}{n}$$

$p$  can be expressed as (3.3). The degree of probability of fault at bit-cell level is inversely proportional to the memory size  $\mathbf{N}$  as mentioned in (3.3). The degree of reliability needed at bit-cell level increases as the memory size increases for a targeted

### 3.1 Yields and margins in SRAM

---

yield **RYL**.

$$p = \frac{\mathbf{RYL}}{n \times m} = \frac{\mathbf{RYL}}{\mathbf{N}} \quad (3.3)$$

With the **PVT** variation, bit-line voltage difference  $\Delta V_{BL}$  and the sense amplifier offset  $V_{SAO}$  vary correspondingly. Both parameters can be considered as continuous random variables. The probability  $p$  can be expressed as explained in (3.4):

$$\begin{aligned} p &= P(\Delta V_{BL} \leq V_{SAO}) \\ &= \int_{-\infty}^{+\infty} f_{SAO}(\nu) F_{\Delta V_{BL}}(\nu) d\nu \end{aligned} \quad (3.4)$$

Where  $f_{SAO}$  is the probability density function of  $V_{SAO}$  and  $F_{\Delta V_{BL}}$  is the distribution function of the bit-line voltage difference  $\Delta V_{BL}$ .

The voltage difference  $\Delta V_{BL}$  is obtained when the bit-line capacitances are discharged by the bit-cell's pull-down transistor **PD** through the pass-gate transistor **PG** during a time-period  $t_a$ , called discharged time (figure.3.2). Relationship between  $\Delta V_{BL}$  and  $t_a$  is given in (3.5) where  $I_{read}$  is the bit-cell read current and  $C_{BL}$  is the bit-line effective capacitance. Considering  $I_{read}$  constant,  $\Delta V_{BL}$  can be considered as a linear function of the discharge time  $t_a$ .

$$\Delta V_{BL} = \frac{I_{read} \cdot t_a}{C_{BL}} \quad (3.5)$$

The probability  $p$  expressed in (3.4) is then :

$$p = P\left(\frac{I_{read} \cdot t_a}{C_{BL}} \leq V_{SAO}\right) \quad (3.6)$$

The parameter  $\frac{\mathbf{RYL}}{\mathbf{N}}$  can be identified as the AQL discussed previously with respect to read operation. AQL can be expressed as (3.7):

$$AQL = \frac{\mathbf{RYL}}{\mathbf{N}} = P\left(\frac{I_{read} \cdot t_a}{C_{BL}} \leq V_{SAO}\right) \quad (3.7)$$



The main target in expressing a matrix read yield in function of cell parameters is first to estimate the required reliability at the cell level to accomplish an acceptable global read operation yield. Second to have the degree of sensitivity of the read yield versus the discharge time  $t_a$ , which is a parameter set by the designer. In next paragraph the global read yield is expressed as a function of the discharge time  $t_a$  with several assumptions.

Let  $\mathbf{Z}$  be a random variable defined as:

$$Z = \frac{I_{read} \cdot t_a}{C_{BL}} - V_{SAO}$$

**RYL** can be expressed as (3.8):

$$\frac{\mathbf{RYL}}{\mathbf{N}} = P\left(\frac{I_{read} \cdot t_a}{C_{BL}} \leq V_{SAO}\right) = P(\mathbf{Z} \leq 0) \quad (3.8)$$

Considering  $I_{read}$  and  $V_{SAO}$  as Gaussian variables,  $\mathbf{Z}$  is also a Gaussian variable with mean value  $\mu_Z$  and the standard variation  $\sigma_Z$  as:

$$\mu_Z = \frac{\mu_{Iread} \times t_a}{C_{BL}} - \mu_{SAO}$$

and

$$\sigma_Z = \sqrt{\left(\frac{\sigma_{Iread} \times t_a}{C_{BL}}\right)^2 + \sigma_{SAO}^2}$$

Equation 3.8 becomes:

$$\frac{\mathbf{RYL}}{\mathbf{N}} = P(Z \leq 0) = F_Z(0) \quad (3.9)$$

where  $F_Z$  is the distribution function of the  $\mathbf{Z}$  variable.  $\mathbf{Z}$  depends on the bit-lines' discharge time  $t_a$ , so determining the delay margin time, revert to solve equation (3.10)

### 3.1 Yields and margins in SRAM

---

against  $t_a$ . Explicitly it is:

$$\int_{-\infty}^0 \frac{\exp\left(\frac{-(x-\mu_Z)^2}{2\sigma_Z^2}\right)}{\sqrt{2\pi}\sigma_Z} dx = \frac{\mathbf{RYL}}{\mathbf{N}} \quad (3.10)$$

Figure 3.4 shows the variation of  $F_Z(0)$  versus the bit-line discharge time  $t_a$ , in case of a 6T bit-cell with:

|          |                  |               |
|----------|------------------|---------------|
|          | $I_{read}$       | $V_{SAO}$     |
| $\mu$    | $31\mu\text{A}$  | $30\text{mV}$ |
| $\sigma$ | $2.2\mu\text{A}$ | $8\text{mV}$  |

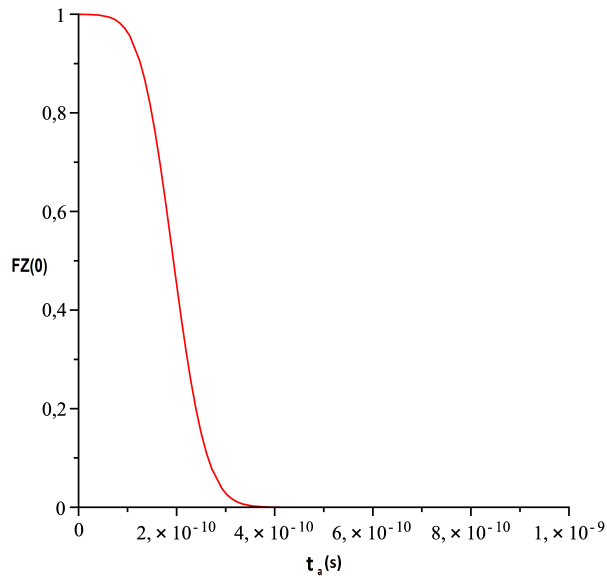


Figure 3.4: Distribution function of  $F_Z(0)$  versus  $t_a$  with  $C_{BL}=200$  fF

Figure 3.4 demonstrates that the discharge delay  $t_a$  is the low level parameter that drives the yield of read operation (**RYL**). One advantage of the modeling effort

|                                   |         |                           |                         |                        |                     |
|-----------------------------------|---------|---------------------------|-------------------------|------------------------|---------------------|
| $t_a(\text{ps})$                  | 400     | 500                       | 600                     | 650                    | 700                 |
| $\frac{\mathbf{RYL}}{\mathbf{N}}$ | 0.00022 | $4.971862 \times 10^{-7}$ | $6.215 \times 10^{-10}$ | $2.14 \times 10^{-11}$ | $7 \times 10^{-13}$ |

Table 3.1: some values of  $\frac{\mathbf{RYL}}{\mathbf{N}}$  versus  $t_a$

presented here is to offer the determination of the critical parameters at the cell level with respect to high level yields to guarantee. As presented in Table (3.1)  $\frac{Y_L}{N}$  decrease three decades after each 100ps of  $t_a$  for an  $AQL = \frac{Y_L}{N} = 10^{-11}$ ,  $t_a$  should be nearly equal to 650ps more than that corresponds to an inflated values of **RYL** and penalize the operation delay, but less corresponds to an unacceptable value of **RYL**.  $F_Z$  shows that **RYL** decrease violently so, according to the theoretical calculation made in this section, the margin estimation can be made with a good precision.

## 3.2 Discussion on modeling results

In this section, results of theoretical calculation made in previously will be compared with the result of Monte Carlo circuit simulations.

The 6T SRAM in figure 3.3 is designed in 32nm CMOS. The effect of various discharge time values is evaluated with respect to read operation yield. The read operation is simulated selecting nominal values for the temperature and supply voltage. For a given discharge time  $t_a$ ,  $10^4$  simulations are performed in the Monte Carlo scheme. The read operation is considered as faulty when  $\Delta V_{BL} \leq V_{SAO}$  in the simulation results. The distribution of  $\Delta V_{BL}$  values is compared to the distribution of the offset in the sense amplifier. The read operation yield is correlated to the overlapping of the distributions. Practically one Monte Carlo run as in figure 3.5 costs nearly 5 min computation on a computer farm. In order to satisfy a yield target, the designer must iterate the Monte Carlo runs providing that he is taking action on an efficient circuit parameter (delay margin  $t_a$  with respect to read operation).

The modeling effort presented here wishes to give explicitly the circuit parameter value from the yield target value.

The Monte Carlo simulation results are plotted in figure 3.6 for increasing discharge time values. The distributions of  $\Delta V_{BL}$  and  $V_{SAO}$  do effectively move away. In this case the read operation yield evaluates favorably. It appears that a discharge value

### 3.2 Discussion on modeling results

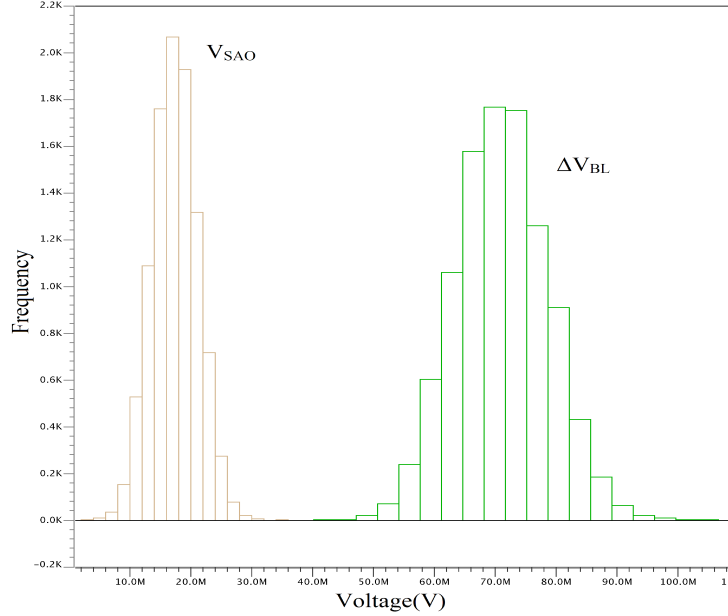


Figure 3.5:  $V_{SAO}$  and  $\Delta V_{BL}$  results of Monte Carlo simulation

of 650ps indicates a change in the behavior of the bit-cell towards a more successful read operation (non significant overlap of the distributions). However the designer only possesses a qualitative approach of the read operation yield. He may not say if  $t_a=650ps$  is sufficient or  $t_a=800ps$  although the impact in operating frequency is important.

The mean value and standard deviation of the  $\Delta V_{BL}$  distributions are plotted in figure 3.7. Monte Carlo simulations show a proportional variation of  $\mu_{\Delta V_{BL}}$  and  $\sigma_{\Delta V_{BL}}$  with  $t_a$ . The increasing  $\sigma_{\Delta V_{BL}}$  balances negatively the increase in  $\mu_{\Delta V_{BL}}$ . So the designer must settle a satisfying  $t_a$  value with respect to the read operation yield. A penalty on the bit-cell operating frequency appears that is not efficiently balanced by the gain with respect to the variability (increasing  $\sigma_{\Delta V_{BL}}$ ).

The modeling approach (3.10) gives explicitly the latter values. In (3.5)  $\Delta V_{BL}$  depends on  $t_a$  assuming that  $I_{read}$  is a Gaussian variable with the mean value  $\mu_r$  and

the standard deviation of  $\sigma_r$ .  $\Delta V_{BL}$  is thus a Gaussian variable with the parameters:

$$\sigma_{\Delta V_{BL}} = \frac{\sigma_r \cdot t_a}{C_{BL}} \quad (3.11)$$

$$\mu_{\Delta V_{BL}} = \frac{\mu_r \cdot t_a}{C_{BL}} \quad (3.12)$$

The proportional variation versus  $t_a$  is explicit and agrees very well with the Monte Carlo verification in figure 3.7. The optimal value for  $t_a$  is extrapolated from (3.5) and is also verified by the Monte Carlo simulation. The main advantage for the designer is to get a quantitative value of the read operation yield that the Monte Carlo simulation can not give. At no cost the model (3.5) gives the appropriate value of the circuit parameter in relation to the operation yield at hand, from a yield target value. This information is interesting to evaluate if a bit-cell is scalable in other technology nodes. Doing the same with the Monte Carlo approach requires to possess a *Design Kit* where transistors characteristics are sufficient, and will cost a tremendous computation effort.

Table 3.2 presents the distribution of the transistor threshold voltage  $V_{th}$  in various technology nodes. The standard variation increases what demonstrates an increase in the variability. Unfortunately the mean value of  $V_{th}$  decreases. As explained in [42], the ratios  $\frac{I_{read}}{\sigma_{I_{read}}}$  and  $\frac{V_{th}}{\sigma_{V_{th}}}$  are proportional in the 6T SRAM.  $I_{read}$  dispersion in future technologies will be the same as the  $V_{th}$  one. The ratio of the  $I_{read}$  mean value to its standard deviation will consequently decrease. (3.11) indicates a similar consequence for  $\Delta V_{BL}$ , independently of the discharge delay  $t_a$ . The distribution function  $F_Z$  (3.9)

|                              |      |      |     |     |
|------------------------------|------|------|-----|-----|
| $V_{th}(\text{V})$           | 0.45 | 0.35 | 0.3 | 0.2 |
| $\sigma_{V_{th}}(\text{mV})$ | 19   | 25   | 28  | 32  |

Table 3.2: transistor threshold voltage  $V_{th}$  value and standard deviation across different technology nodes

is affected similarly to the other variables. In table 3.2 the standard deviation increases

### 3.2 Discussion on modeling results

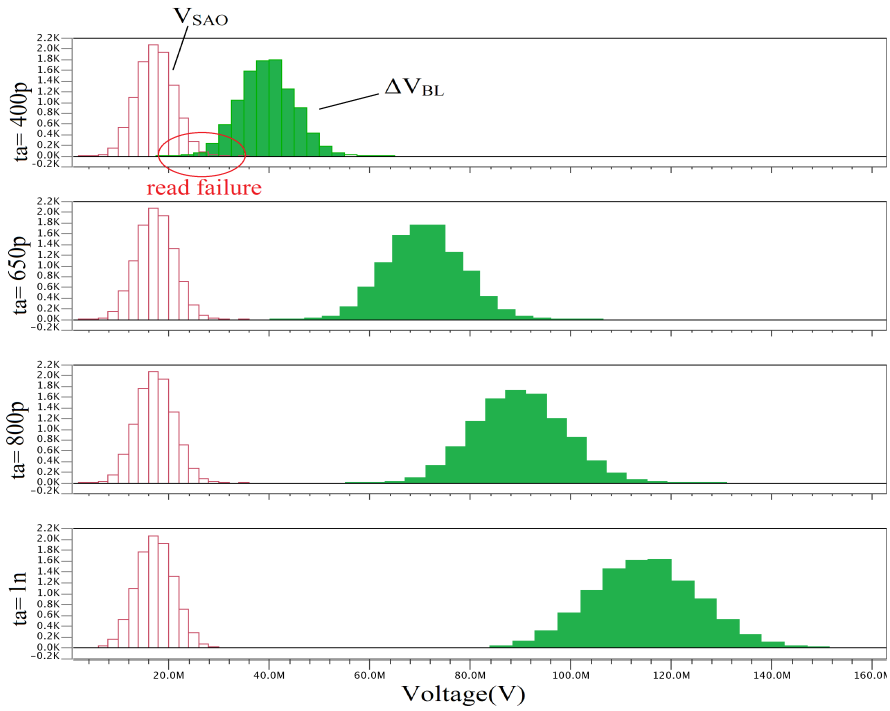


Figure 3.6: Monte Carlo simulation results  $\Delta V_{BL}$  for different  $t_a$  values

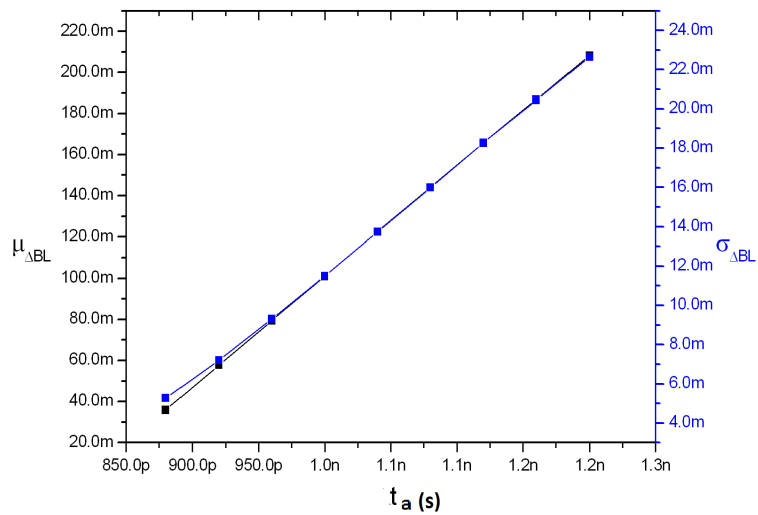


Figure 3.7:  $\mu_{\Delta V_{BL}}$  and  $\sigma_{\Delta V_{BL}}$  versus the discharge time  $t_a$

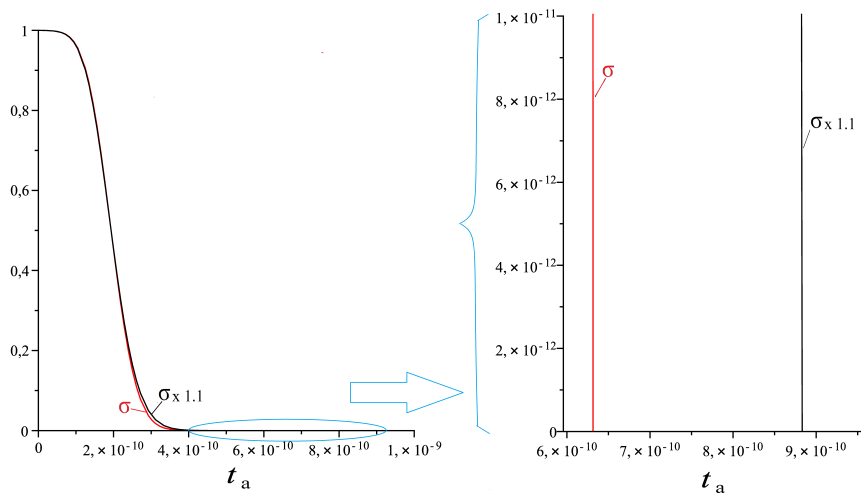


Figure 3.8:  $t_a$  margin variation with a 10%  $\sigma$  increasing

of nearly 12% between 45nm and 32nm technology nodes and 32nm and 22nm respectively. The same variation is considered for the standard deviation of  $F_Z$ . The figure 3.8 shows that a variation of 12% of  $\sigma_Z$  requires an additional  $t_a$  delay of 350ps what means 26% in operating frequency penalty for the same read operation yield.

Moreover the typical memory cut is expected to increase in size while variability is also expected to increase. The target in read operation yield is expected to be the same or even increase so the reliability of the bit-cell in read mode operations needs to improve drastically (3.7). The proposed model indicates that the read operation yield of the 6T SRAM faces several problems to come.

**Remarque** Figure 3.7 may be interpreted differently. In the Cadence framework and the Design-Kits, the transistor parameters are represented as Gaussian distributions with respect to Monte Carlo approach. Then it could be said that the similarity of the waveforms in figure 3.7 is not surprising as the model presented here is based on a Gaussian approximation. This observation may only be verified experimentally but the number of devices to be considered is unreasonably huge. The fact is also that the leakage current for example is not a Gaussian distribution through Monte Carlo

### 3.2 Discussion on modeling results

---

simulations. So Gaussian parameters do not obligatorily lead to Gaussian quantities through simulations. This argument is not in favor of the observation. Finally even if the latter observation stands, it is obvious that the modeling approach detailed in (3.10) gives directly results that cost a large simulation effort otherwise. In the worst case, the validation of the method may be said as uncompleted but it is sufficient to show how promising is the modeling approach.

**Conclusion** This section introduces a modeling approach for variability. In the case of the read operation of the 6T SRAM, an explicit model relates the read operation yield to the circuit parameter of main influence (discharge time  $t_d$ ). This model has been verified using Monte Carlo simulations. The results are satisfying and push for a further development of the approach.

Meanwhile the application to the 6T SRAM shows the limitations of this bit-cell in advanced technologies. The penalty in discharge time margin becomes impracticable. In fact the voltage read mode is limited. The principle of bit-line discharge is power consuming on one hand and prone to delay on the other hand. In contrary the 5T-Portless SRAM in the next chapter takes its advantages from a current mode read operation.





---

## PORTLESS BIT-CELL AND CURRENT MODE OPERATION

---

### 4.1 5T SRAM bit-cells

There are two kinds of bit-cells with 5T transistors in literature: the 5T asymmetric [43, 44] and the 5T Portless [45, 46, 47]. Figure 4.1 pictures both 5T SRAM bit-cells with their respective butterfly curve. The 5T asymmetric bit-cell offers more density than the 6T bit-cell and a better leakage current margin [43], but it requires a complex periphery. Because of its single bit-line, the write ability and read stability trade-off is difficult to obtain. The design of the 5T asymmetric requires thus an additional periphery to assist the read and/or write operation [44]. The dynamic hopping of supply voltage is the efficient lever to solve the read/write antagonist assistance. It renders the memory peripheral more complex than for the 6T. It reduces the possible gain in density with the missing transistor. This added overhead and the relatively limited benefits have prevented the widespread use of asymmetric 5T cells. Moreover the 5T asymmetric has been demonstrated in 45nm but not in 32 nm.

The 5T-Portless remains the alternative bit-cell to the 6T bit-cell for low-power and always-on applications. The Pass-Gate transistors are missing in the Portless bit-cell but replaced by a transistor (AXS) connected to the two bit-cell internal nodes.

## 4 PORTLESS BIT-CELL AND CURRENT MODE OPERATION

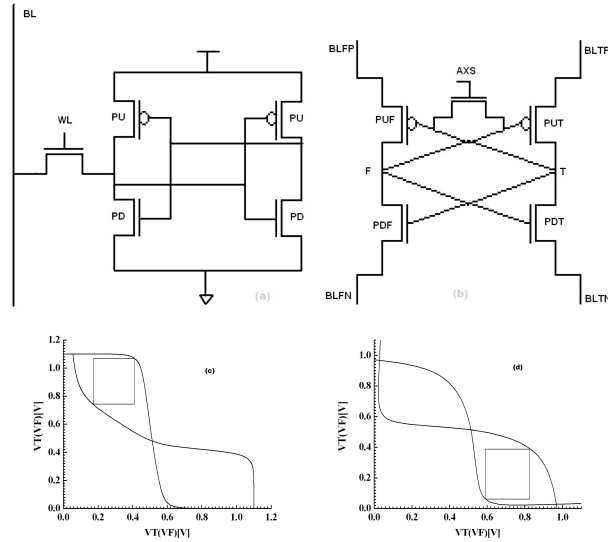


Figure 4.1: Schematic and simulated SNM of 45nm 5T asymmetric SRAM (a,c) and 5T Portless SRAM (b,d)

The AXS's gate voltage  $V_{AXS}$  acts as the word line signal that enables the read and write operations. The Portless bit-cell inherently operates in current mode. The bit-cell is supplied by the bit-lines and the data sensed from the bit-cell is the bit-line current difference. This chapter presents the 5T-Portless bit-cell with its state of the art, parameters and performances.

### 4.2 5T-Portless bit-cell

The 5T-Portless comprises 5 transistors as shown in figure 4.2.

In this bit-cell structure, the data information sensed from the bit-cell is not the bit-line voltage difference but the bit-line current difference: as shown in figure 4.3 the bit-line current difference depends on the data stored in the bit-cell. In case of  $F=0$  ( $T=1$ ), the read current is sinking from BLTP and sourcing to BLFN when AXS transistor is activated. A current difference is created between BLTP and BLFP (positive bit-lines biased to  $V_{DD}$ ) and also between BLTN and BLFN (negative bit-lines biased

## 4.2 5T-Portless bit-cell

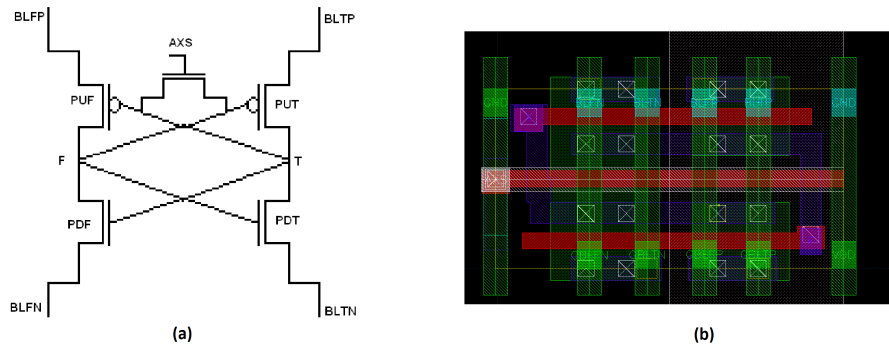


Figure 4.2: Portless bit-cell: (a) schematic, (b) layout

to GND).

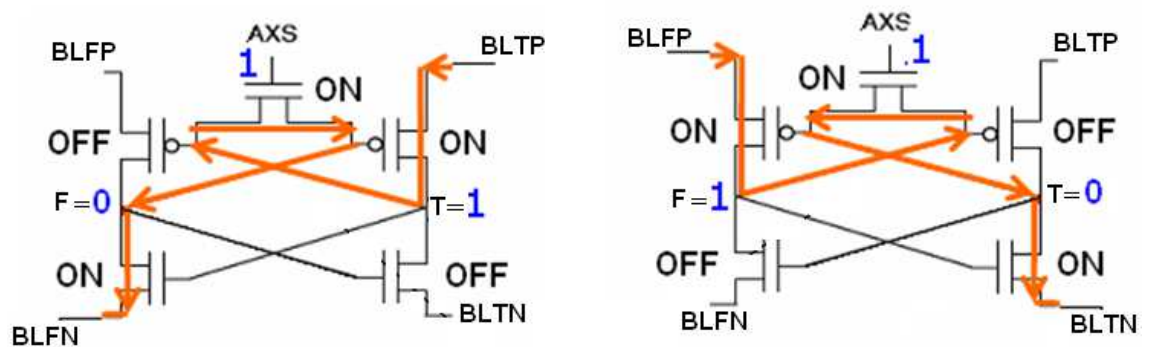


Figure 4.3: Portless current in read operation

The Portless SRAM bit-cell presents a good stability with a low power read/write operation [47]. Portless internal nodes are not related directly to bit-lines so they are not disturbed by bit-line voltage in read operation. Figure 4.4 shows the Monte-Carlo simulation of the SNM performance for the 45nm CMOS 6T and Portless bit-cells respectively. The 6T bit-cell shows more vulnerability to the process variations than the Portless bit-cell: the simulated SNM is fitted with a Gaussian distribution with the resulting parameters  $\mu=214\text{mV}$  ( $\sigma=25\text{mV}$ ) for the Portless bit-cell. It is safer than  $\mu=187\text{mV}$  ( $\sigma=23\text{mV}$ ) for the 6T bit-cell (figure 4.4.c). The requirement for operational bit-cells up to  $7\sigma$  from the mean-value is more favorable when the SNM mean-value

## 4 PORTLESS BIT-CELL AND CURRENT MODE OPERATION

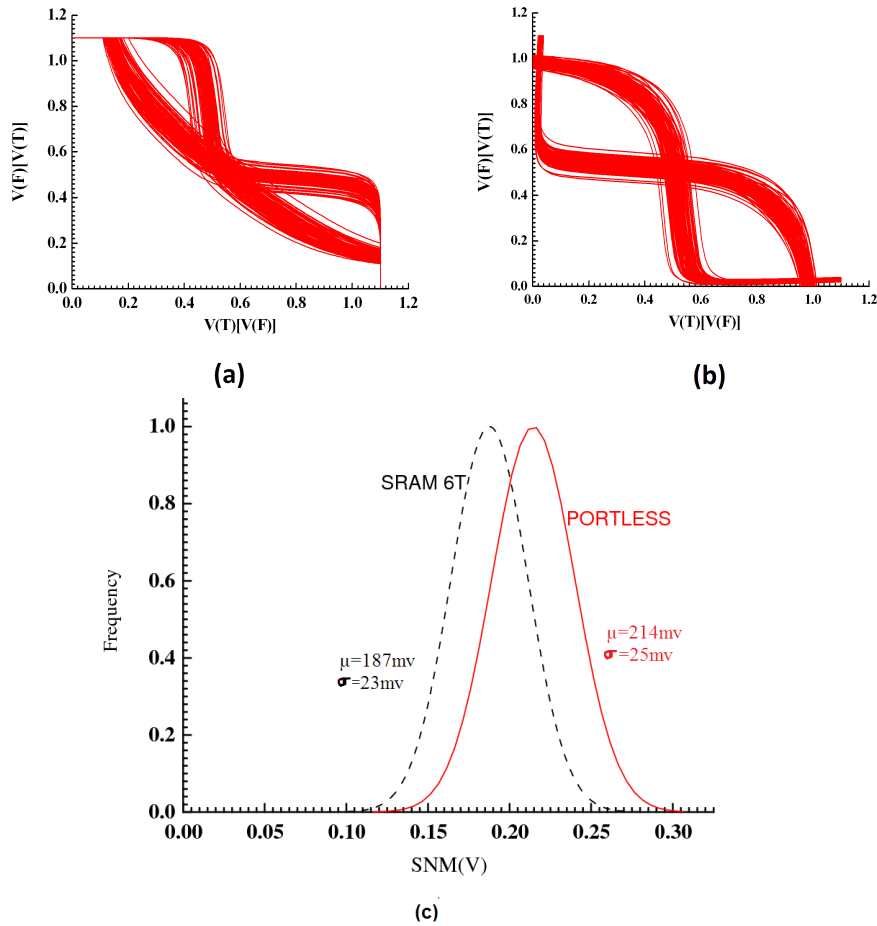


Figure 4.4: BFC comparison of Monte Carlo simulation with  $N=10^4$  iteration between 6T (a) and Portless (b) and gaussian distribution fit (c)

is higher. The critical minimum value of SNM is more easily reached when the mean value is smaller. The Portless bit-cell comprises less transistors hence less mismatch, plus the bit-line has no direct action on the internal nodes of the bit-cell, hence less perturbation in read mode.

The lack of Pass-Gate transistors eliminates their contribution in term of leakage, so the leakage sources in Portless are less than in 6T. The Portless bit-cell features 3-times less leakage current than the 6T bit-cell. Figure 4.5 presents the 6T and Portless leakage values obtained by a Monte Carlo simulation (45nm design). The Monte-Carlo

## 4.2 5T-Portless bit-cell

simulation gives fitting parameters  $\mu=11.6\text{pA}$  and  $\sigma=9\text{pA}$  for the Portless bit-cell and  $\mu=38\text{pA}$  and  $\sigma=30\text{pA}$  for the 6T bit-cell respectively. The leakage distribution of the two bit-cells shows that the Portless is less leaky than the 6T and has much less standard deviation.

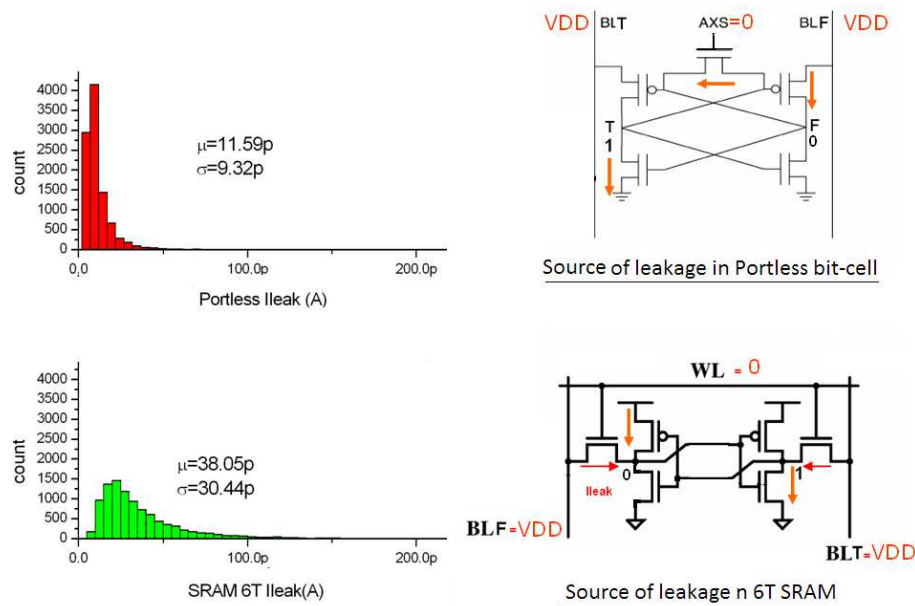


Figure 4.5: leakage comparison between 6T and Portless bit-cells

It is clear that the Portless presents better performances than the 6T in stability, density and static consumption at bit-cell level. In [46] the technique used to sense the bit-cell data is to amplify the bit-lines current difference with a current amplifier. Many kinds of current amplifier have been experimented [48, 49] but the current difference generated by the bit-cell is quite small. An average value of  $6.29\mu\text{A}$  is simulated for a typical PVT corner (figure 4.6) for the bit-cell in CMOS 32nm. The current sense amplifier for the SRAM memory suffers from an offset due to the transistor mismatch that continues to rise at each technology advanced node. This problem must be overcome.

The current mode presents several advantages [49]. The bit-lines are not dis-

## 4 PORTLESS BIT-CELL AND CURRENT MODE OPERATION

charged during read or write operations, so the dynamic power is reduced and the read operation is less sensitive to the bit-line capacitance fluctuation that affects the discharge time delay thus the operation speed. In return the sense amplifier presents a problem in its functionality due to the transistors' mismatch that affects considerably the read current value because of offsets. The leakage of bit-cells in retention mode in the same column perturbs also the current values. These phenomena reduce the reliability of the current amplifiers essentially for the small current values, what is the case in the Portless bit-cell.

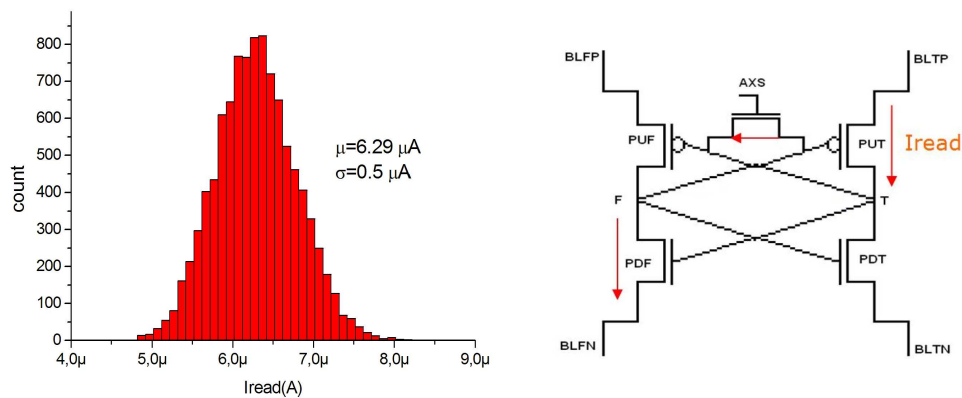


Figure 4.6: Monte Carlo simulation results of  $I_{read}$  for a typical PVT corner in CMOS 32nm

In write operation, the technique used is to lower the potential of the BLTP and BLFP bit-lines (figure 4.2) to create a voltage difference between the inverters' supply voltage and to flip the bit-cell data [46]. The AXS transistor is activated during the write operation. This method presents a functionality issue in advanced technology nodes because of the supply voltage scaling. Pulling-down one bit-line potential can destroy the data of the bit-cells of the column in retention mode [26].

The Portless bit-cell presents good performances in stability and power consumption but its read/write current mode presents a reliability problem. In next section bit-cell parameters and characterizations are detailed. A new current mode for write and read operations is presented based on a technique called "hard line copy". This

## 4.2 5T-Portless bit-cell

---

technique solves the problem of the current amplifier and enables to realize read, write and multiplexer operations with reduction in power consumption and augmented reliability.

### 4.2.1 5T-Portless bit-cell parameters

Two parameters are defined to evaluate the read stability and write ability of the Portless bit-cell. The first one,  $\Delta VR$ , denotes the internal nodes' voltage difference and determines the bit-cell stability. The higher  $\Delta VR$ , the less possible the situation of perturbation of the bite-cell internal node voltage. The second parameter is  $I_{read}$ , the drain current of the AXS transistor. The latter current is the same as the current difference between the bit-line ones (Figure 4.7).  $\Delta VR$  and  $I_{read}$  depend on  $V_{AXS}$  (gate-to-source voltage of transistor AXS). Figure 4.8 shows the DC simulation results for  $\Delta VR$  and  $I_{read}$  in a 32nm Portless bit-cell as function of  $V_{AXS}$  for process corners Fast NMOS/Fast PMOS (FF), Fast-Slow (FS), Slow-Fast (SF), Slow-Slow (SS) and Typical-Typical (TT) respectively.  $V_{AXS_{read}}$  is the  $V_{AXS}$  value that corresponds to the maximum of  $I_{read}$ , with enough  $\Delta VR$  margin: it is then an optimal operating point for read operation.  $V_{AXS_{write}}$  is the  $V_{AXS}$  value that corresponds to a null  $\Delta VR$  margin: it is an ideal condition for write operation. It may be noted that  $V_{AXS_{read}}$  value for FS corner is less than for SF. It remains unchanged for the other corners.  $V_{AXS_{write}}$  depends also on the operating corner. Particularly  $V_{AXS_{write}}$  must be larger than  $V_{DD}$  to reach null  $\Delta VR$  conditions in SF corner. There is then an interest to provide a circuit-level correction of the process corner effects to control the optimal value of  $V_{AXS_{write}}$  and  $V_{AXS_{read}}$  respectively. It is the purpose of next section.

### 4.2.2 Wordline driver

The circuit presented in figure 4.9 is a voltage divider when the PMOS and NMOS transistors are both turned-on. It will be used to control the AXS transistor gate. It



## 4 PORTLESS BIT-CELL AND CURRENT MODE OPERATION

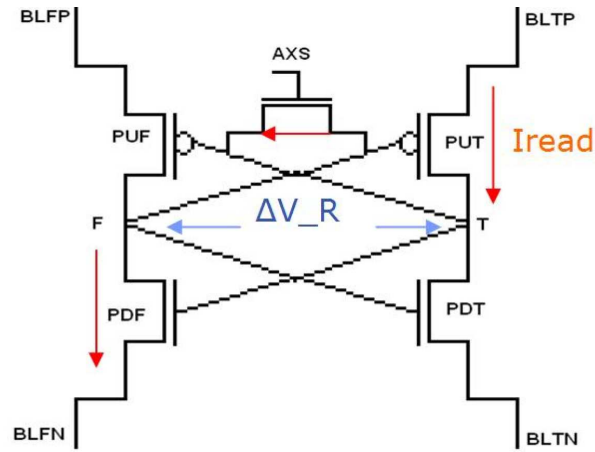


Figure 4.7: Portless bit-cell parameters

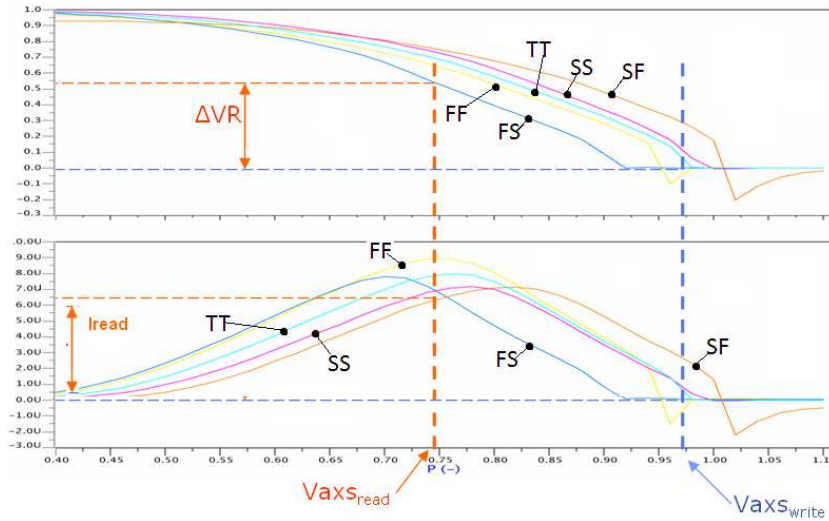


Figure 4.8:  $\Delta V_R$  and  $I_{read}$  Versus VAXS

### 4.3 Hard-line duplication technique

is namely a World Line Driver (**WLD**). The voltage  $V_S$  is a fraction of  $V_{DD}$ , but its value depends on the process corner. The  $V_S$  value increases in case of SF corner and decreases in case of FS corner. Figure 4.10 presents simulation results for different PVT (Process Voltage Temperature) corners. The nominal value of  $V_S$  can be adjusted with proper PMOS and NMOS transistors' sizing. The value  $V_S$  is set to provide the  $V_{AXS_{read}}$  value for all corners because when  $V_S$  increases, it compensates for the slow NMOS and when it decreases, it compensates for the fast NMOS corner. In write operation the  $V_{AXS}$  value must be larger than  $V_{DD}$  to ensure a null  $\Delta VR$  condition. A charge pump as in Figure 4.11 is used to produce the proper voltage value [50]. The capacitors are integrated as CMOS gate capacitance. Figure 4.11 shows the Word-Line driver with the different WP and RP signal sets for read, write and retention mode respectively.  $V_{ddo}$  is the voltage outcome from the latter charge pump. This circuit is simple and solves the problem of process variability without significant area penalty.

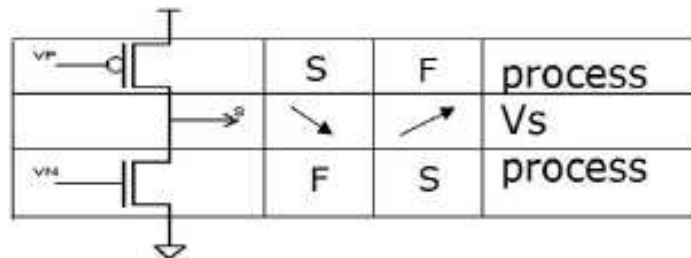


Figure 4.9: PMOS, NMOS Voltage divider

### 4.3 Hard-line duplication technique

Previous section has shown that the bit-cell with a  $V_{AXS}$  value set to  $V_{AXS_{read}}$  is stable and presents an optimal  $I_{read}$  value. The same bit-cell with  $V_{AXS}$  set to  $V_{AXS_{write}}$  is completely destabilized and easy to write. The idea for a hard-line duplication technique is to select two Portless bit-cells in the same column, as shown in figure

## 4 PORTLESS BIT-CELL AND CURRENT MODE OPERATION

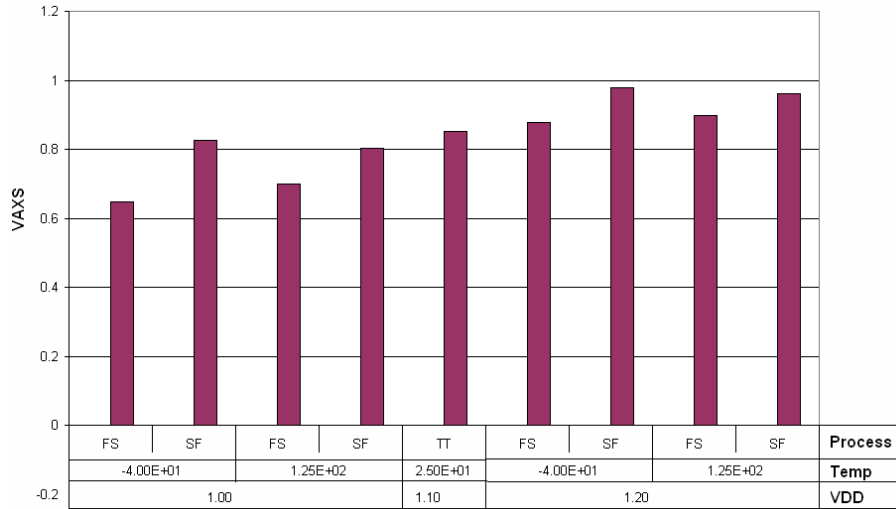


Figure 4.10: simulation results of WLD in different PVT corners

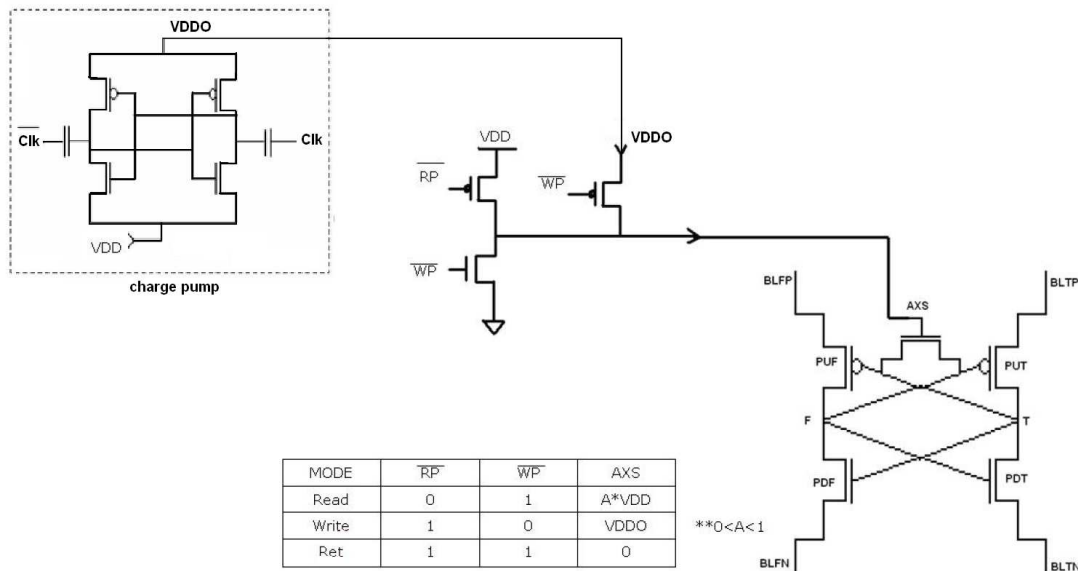


Figure 4.11: Charge pump circuit and the Word-Line Driver with RP and WP signal sets

#### 4.4 Portless Sense and Mux architecture

---

4.12. One bit-cell (Rcell) is biased with voltage  $V_{AXS} = V_{AXS}_{read}$  and an other bit-cell (Wcell) with voltage  $V_{AXS} = V_{AXS}_{write}$ , the other bit-cells in the same column are in retention mode, i.e.  $V_{AXS} = 0$ . The bit-line precharge circuit consists of PMOS and NMOS pairs operating as current sources. The  $I_{read}$  current of the bit-cell Rcell creates a current difference between bit-lines BLTP and BLFP of the column. The bit-cell Wcell is rendered less stable than the bit-cell Rcell and consequently injects and/or absorbs a current so as to compensate the current difference. The current in Wcell imposed by the bit-line current difference defines the data stored in Wcell. Data is thus copied from the bit-cell Rcell to the bit-cell Wcell but the other bit-cells in the same column are not disturbed by the operation. This method offers a large gain in dynamic power consumption because bit-lines are not charged nor discharged during the operation. Moreover the duplication operation is performed in one clock cycle.

This technique allows to copy a data from one bit-cell of a column to another bit-cell of the same column in one clock cycle, without changing the bit-lines' voltage values. Figure 4.13 shows bit-line voltage and internal nodes voltage waveforms during a hard line copy operation. With this method a significant gain in dynamic power is possible compared to the standard 6T SRAM, additionally to the reduction in bit-cell leakage.

## 4.4 Portless Sense and Mux architecture

The previous section has presented the portless bit-cell and the principle of operation inside a column arrangement. The hard-line duplication copy is now used to access a bit-cell value in read operation and also write operation.

## 4 PORTLESS BIT-CELL AND CURRENT MODE OPERATION

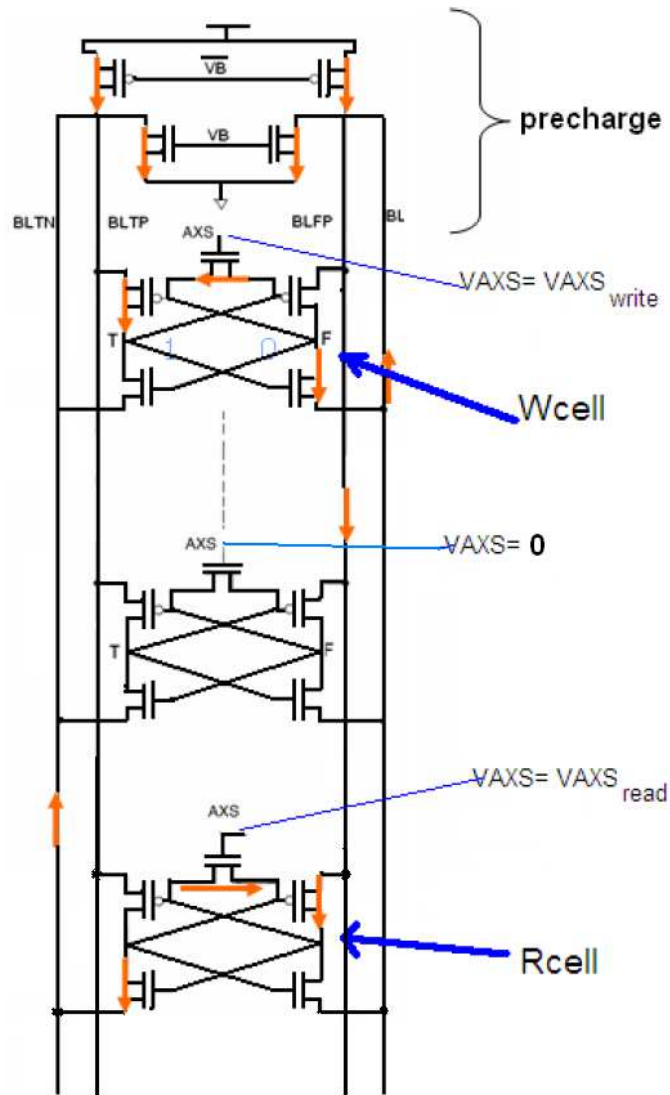


Figure 4.12: Proposal of Portless bit-cell arrangement

## 4.4 Portless Sense and Mux architecture

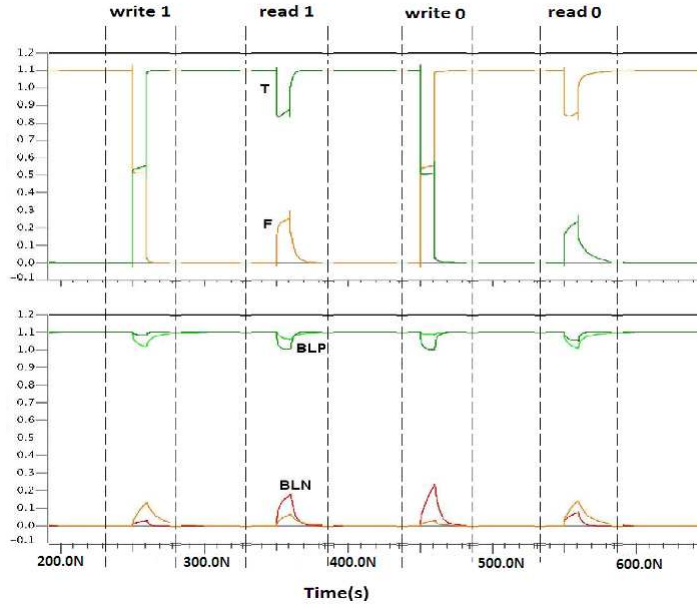


Figure 4.13: Bit-line and internal nodes voltage in read and write operation

### 4.4.1 Current mode sensing and writing

In order to sense/write the data from/in a bit-cell in a column, an additional Portless bit-cell, called **IOcell** (Input Output cell), is placed at the bottom of each bit-cell column (figure 4.14). Two access transistors are added in order to read or write a data in the IOcell. In read operation,  $V_{AXS}$  of a given bit-cell is set to  $V_{AXS}_{read}$  and the IOcell is set to  $V_{AXS}_{write}$  value, applying the hard-line duplication technique between the targeted bit-cell and the IOcell. The data is copied from the targeted bit-cell to the IOcell. Write operation is performed dually by inverting the roles of the IOcell and the targeted bit-cell. The sensing technique allows to keep positive bit-lines voltage at  $V_{DD}$  and negative bit-line voltage at GND in retention, write or read operations. This offers a large gain in dynamic power consumption because bit-lines are not charged nor discharged at every write or read operation. The bit-cells in a same column are not disturbed by the operations in one of them.

The novel current functioning proposes a possibility to realize the current read/write

operation without a sense amplifier that causes high dynamic power consumption and a weak tolerance to variability. The conventional problem in the 6T SRAM architecture is the trade-off to settle between write ability and read stability. A stable bit-cell is difficult to write and an easy bit-cell to write is not stable in the read operation [25]. This trade-off is more and more difficult to find at each technology node. In Portless architecture, the hard-line duplication technique allows to have a read operation (copy of the data from the bit-cell to the IOcell) and a write operation (copy of the data from the IOcell to the bit-cell) exactly by the same mechanism. The trade-off to set between write ability and read stability doesn't exist with this read/write technique. The advantage of the read/write operation with the hard-line duplication method makes the Portless a good candidate for advanced technologies.

The bit-line current difference depends actually on the leakage current generated by the rest of the column bit-cells which are in retention mode. So the number of bit-cells in a column may be limited. In this case the solution is to divide the column height and to arrange the matrix into a multiplexed structure.

### 4.4.2 Low Power Mux structure

In a 6T Mux structure, in read or write operation, WLs of both selected and unselected bit-cells are activated, so all these bit-cells are sinking current, thus the read current is consumed Mux times. Unselected bit-cells which are in retention mode are also disturbed by the WLs activation. The hard-line duplication technique offers in contrary a feasibility of a Mux structure with a low power consumption. Figure 4.17 shows a matrix arrangement of Portless bit-cells for a cut of L words by C bits and M multiplexers. The matrix of L words is divided in L/M sub-matrix of M words. Each sub-matrix columns are connected to a Mux-cell, as shown in figure 4.15. It contains two bit-cells, Lcell and Gcell. Lcell is connected to the sub-matrix bit-cells and Gcell is connected to the Gcells of the other sub-matrices and to the IOcell. Gcell and Lcell

#### 4.4 Portless Sense and Mux architecture

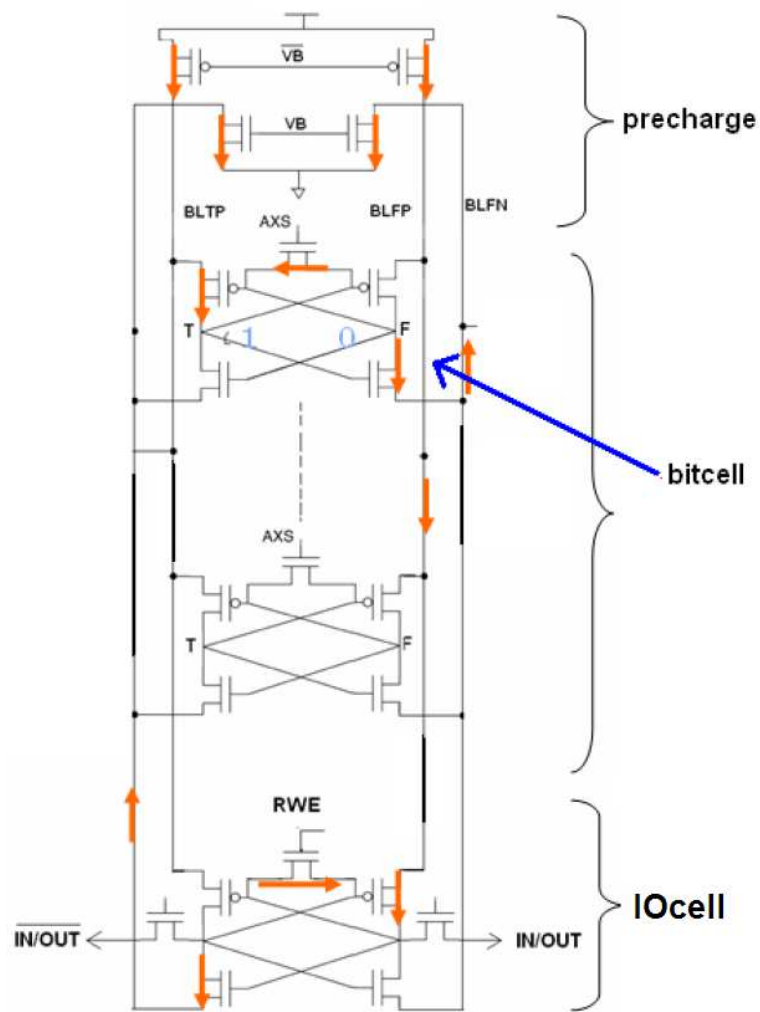


Figure 4.14: Portless bit-cell column with IOcell



#### 4 PORTLESS BIT-CELL AND CURRENT MODE OPERATION

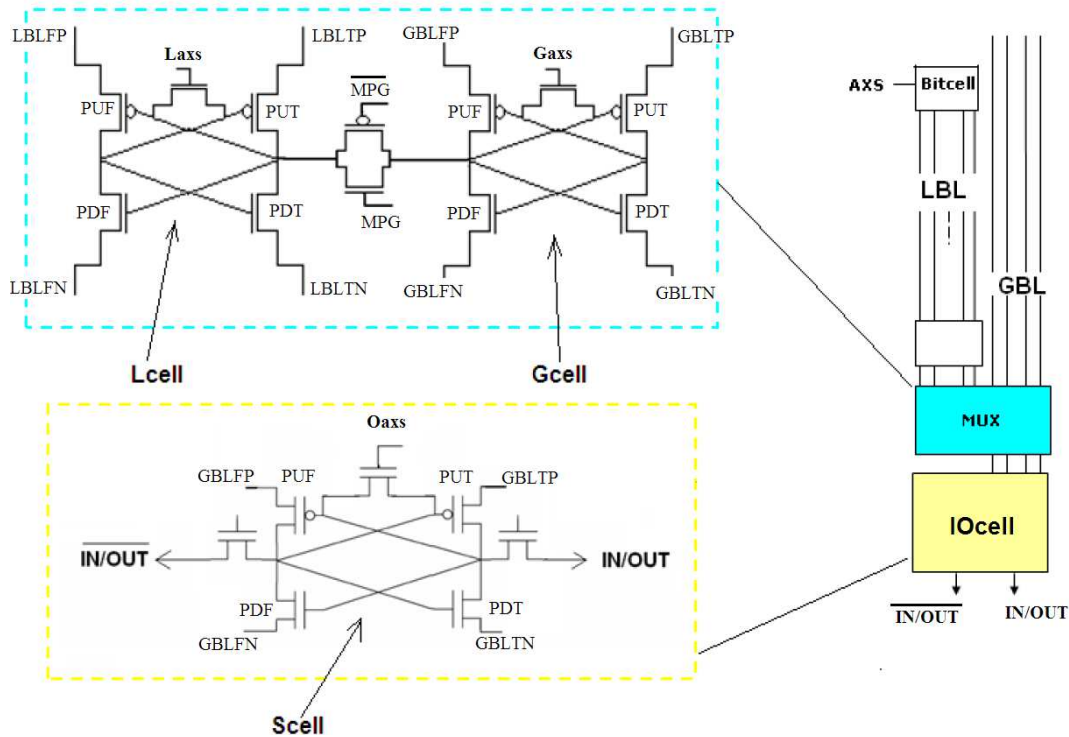


Figure 4.15: Mux bit-cells and Sense

are connected via a double switch. In this structure there is a local bit-line to relate the sub-matrix bit-cells and Lcell with their proper precharge circuits, and Global bit-lines to relate Gcells and IOcell with proper precharge circuits.

The write operation is performed in three steps based on the hard-line duplication method. First the IOcell data is copied into the Gcell. Secondly the data is copied from Gcell to Lcell through the double switch and finally the data is copied from Lcell to the targeted bit-cell. Figure 4.16 shows transient simulation results of a write operation, i.e. the bit-cells' Vaxs voltage and bit-cells' internal node voltages. Two access transistors are added to the IOcell in order to read or write a data. The write operation is performed the other way round, inverting the roles of Gcell and Lcell respectively. This new MUX architecture allows a gain in dynamic power: only read or write bit-cells are sinking/sourcing current, and the hard-line duplication operates

#### 4.4 Portless Sense and Mux architecture

without charge nor discharge of bit-lines. Bit-cells in retention are not disturbed and may even be in retention mode under low  $V_{DD}$  condition to reduce leakage [26].

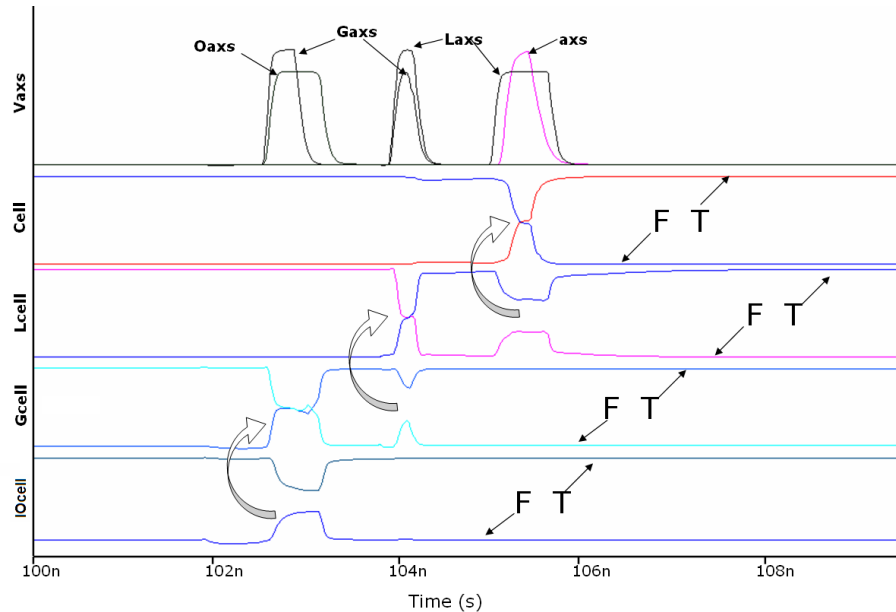


Figure 4.16: Vaxs and cells' internal node voltages during a write operation in a CMOS32nm Portless arrangement

This chapter has introduced the 5T Portless SRAM as a good candidate for low-power, always-on memory. The classical voltage sense has come to a limit as demonstrated in literature. The use of current sense amplifiers does not solve the limitations. The hard-line duplication has been developed and overcomes the limitations. The 5T-Portless also operates with new conditions that give new interests in the Portless in advanced technology nodes. The leakage issue is naturally minor because of the 5T structure. The dynamic power consumption is controlled through a multiplexed arrangement of bit-cells and an original implementation of the hard-line copy technique. Next chapter introduces the design and simulations in CMOS 32nm.

## 4 PORTLESS BIT-CELL AND CURRENT MODE OPERATION

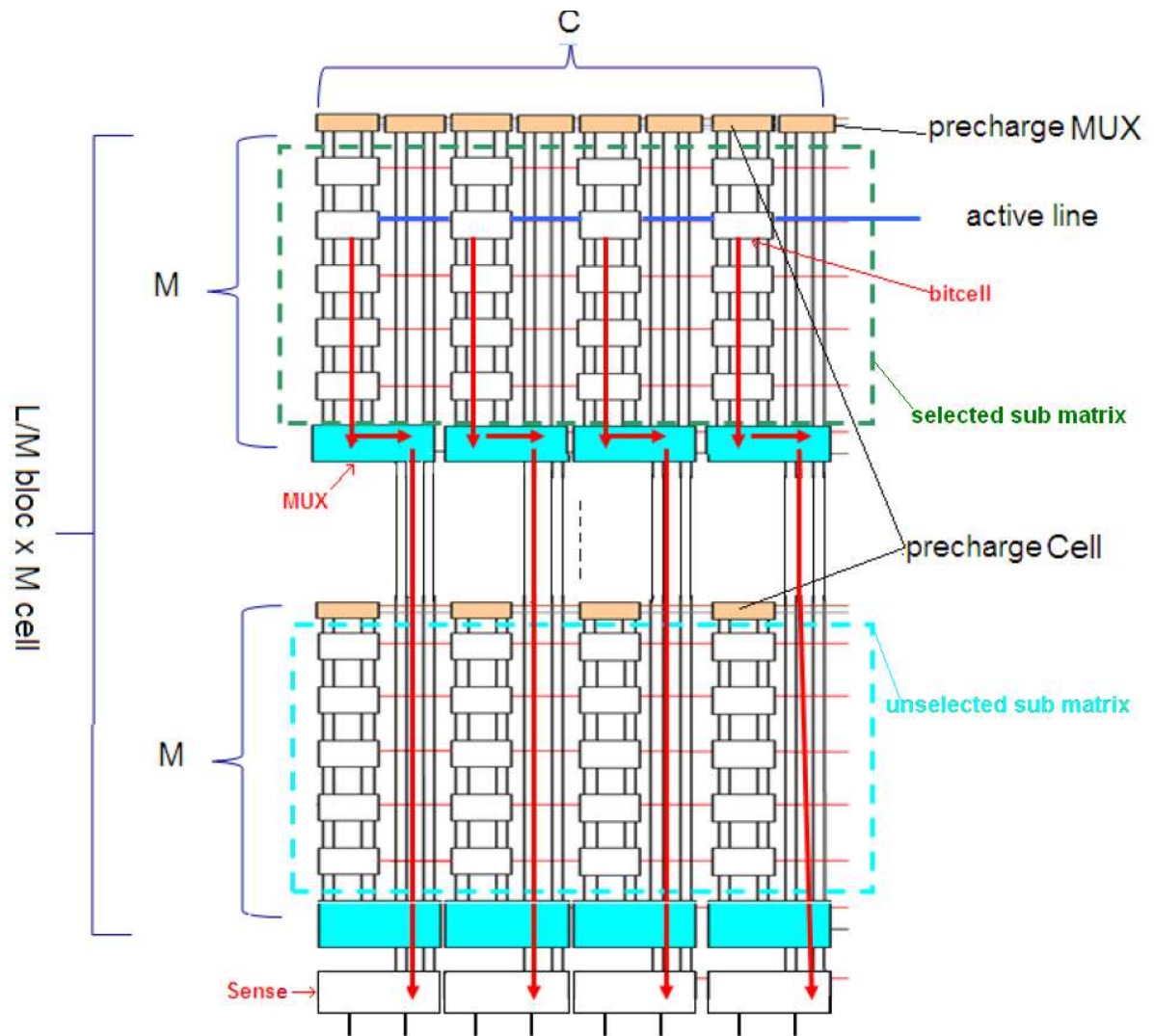


Figure 4.17: Portless multiplexer architecture

---

## Test chip and simulation results

---

The original structure of the 5T-Portless memory based on the hard line-duplication technique is implemented in CMOS 32nm. A cut of 64Kb ( $1024 \times 64$ ) is developed in this technology. Figure 5.1 shows the structure of the cut. The matrix of  $1024 \times 64$  is divided into 32 sub-matrixes of  $32 \times 64$  bits. The Multiplexer architecture detailed in Chapter 4 is implemented here. The *WLD* block is the word line driver that generates the *VAXS* voltage potential level. A charge pump is placed in each sub-matrix to control the *Vddo* level for the *WLD* block. The *Control* block controls the read and the write operations and the retention mode. It generates the pulse for different signals (*AXS*, *Gaxs*, *Laxs*, *Oaxs* . . .). This block is repeated for each sub-matrix to reduce the power consumption by limitation of wires' length. *Dummy* is a fictitious line of cells that gives a feedback about the process status to set up the control signals. Finally the *Decoder* blocks select the active sub-matrix (*MSB*) and the sub-matrix' active line (*LSB*). A technique of predecoding is implemented to reduce the dynamic power consumption.

In this chapter the design of the memory cut is detailed. Simulation results and a benchmark with the conventional 6T architecture is discussed.



Figure 5.1: Schematic of the 5T-Portless memory cut

## 5.1 Test chip design

---

|                             |                       |
|-----------------------------|-----------------------|
| Supply Voltage ( $V_{DD}$ ) | 0.9V, 1V, 1.1V        |
| temperature                 | -40°C, +25°C, +125 °C |
| process corner              | FF, FS, SF, SS, TT    |

Table 5.1: Testchip PVT Specification

## 5.1 Test chip design

The different blocks required to apply the hard line duplication are presented. The technique of hard line duplication is implemented to ensure the read and write operations and activates the multiplexed structure. The design is implemented with the CMOS32lp (low power) RVT (regular  $V_{th}$ ) process. The gate length is extended to 40nm to have a positive impact on the leakage and variability issues. As explained in (2.1), the increase in L and W concurs to a reduction in  $V_{th}$  hence on bit-cell performance with respect to variability. The test chip must be functional with the following specifications:

Simulations are performed with the "Eldo" simulator for the small blocks and with the simulator "xa" (fast spice simulator) for the full cut. All simulations in this chapter are performed with extracted netlists that include the parasitic devices in layout.

### 5.1.1 Bit-cell to matrix array

The 5T-Portless, as explained in Chapter 4, is a cross-coupled inverter with an *AXS* transistor. The *AXS*' drain and source are connected to the bit-cell internal nodes. The bit-cell is supplied by its four bit-lines: *BLTP* and *BLFP* (connected to  $V_{DD}$  potential voltage) and *BLTN* and *BLFN* (connected to the GND potential voltage). The five bit-cell transistors are sized to  $W=240\text{nm}$  and length  $L=40\text{nm}$ . The bit-cell size is  $0.444\mu\text{m} \times 0.864\mu\text{m} = 0.383\mu\text{m}^2$ . The eSRAM is designed with the standard Design Kit, i.e. without the SRAM implants that allow the violation of DRC (Design

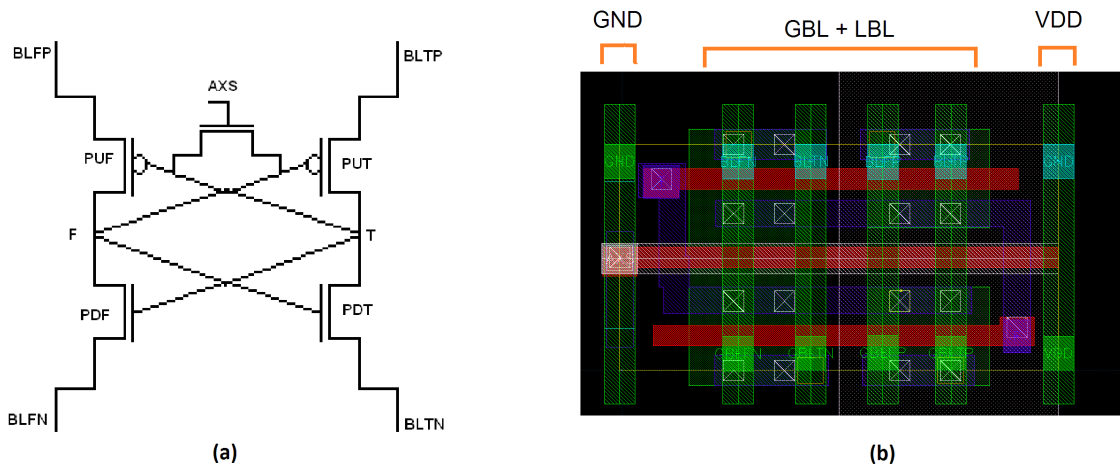


Figure 5.2: 5T-Portless bit-cell, schematic (a), layout (b)

Rule Check) for a more aggressive density. The density of the Portless bit-cell is here quite modest but comes from a trade-off with immunity to variability and low power performance.

Figure 5.2 presents the Portless bit-cell's Layout and schematic views. Local bit-lines, which connect the same column bit-cells, are in layer *M2* (metal 2). The global bit-line, that connects the Mux's global bit-cells of the sub-matrices and the IOcells, are in layer *M4* (metal 4). The *AXS* signal is in layer *M3* (Metal 3).

As explained previously the  $1024 \times 64$  bit matrix is divided into 32 sub-matrices of  $32 \times 64$  bits, in order to limit the number of bit-cells in a column. So the global bit-lines and local bit-lines drive the same number of bit-cells: 32 bit-cells in a global bit-line column and 32 bit-cells in a local bit-line column.

The Mux cell as detailed in Chapter 4, has two bit-cells. The Mux-cell and the Portless bit-cell has the same width ( $W_{MUXcell} = 0.864 \mu\text{m}$ ) and a length of  $L_{MUXcell} = 1.985 \mu\text{m}$ . Figure 5.3 presents the cell layout and schematic views. *Lcells* are connected to local bit-lines and *Gcells* are connected to global bit-lines. The signals *Laxs*, *Gaxs* *MPG* and  $\overline{MPG}$  are in layer *M3* (metal 3).

Figure 5.4 presents the layout and schematic of the precharge circuit. Like the

## 5.1 Test chip design

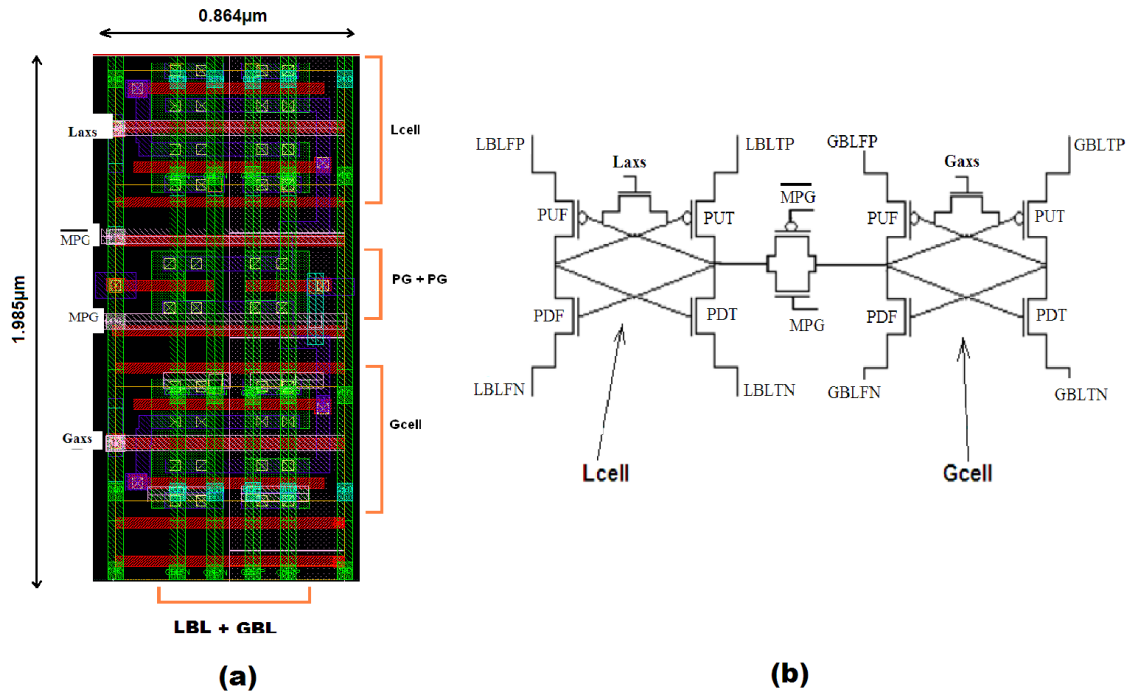


Figure 5.3: Mux cell layout (a) and schematic (b)

Mux cell, the precharge circuit has the same width ( $W_{Precharge}=0.864\mu\text{m}$ ) and length of  $L_{Precharge}=3.166\mu\text{m}$ . The fictitious bit-cell (Dummy bit-cell) is added at the bottom of the column and controlled by the *DAXS* signal. The sub-matrix column has an arrangement as presented in figure 5.5. As indicated previously all control signals (*AXS*  $\langle 0:31 \rangle$ , *LAXS*, *GAXS*, *PG* and *DAXS*) are in layer M3 (Metal 3). The Global bit-lines are in M4 (Metal 4) and Local bit-lines in M2 (Metal 2).  $V_{DD}$  and GND are layered vertically in M2 an M4 and horizontally in M3 to obtain a standard supply grid (i.e. a satisfying trade-off between proximity to the bit-cell, parasitic impedances and silicon penalty of the metal routing).

The sub-matrix layout is presented in figure 5.6. The sub-matrix size including the Mux cell, Dummy line and precharge circuit is  $55.30\mu\text{m} \times 19.80\mu\text{m} = 1094.94\mu\text{m}^2$ . The sub-matrix embeds  $32 \times 64$  bits, so the equivalent bit area is  $0.534\mu\text{m}^2$ . The sub-matrix arrangement inflates the bit-cell area by 39%. The Mux cell is one main



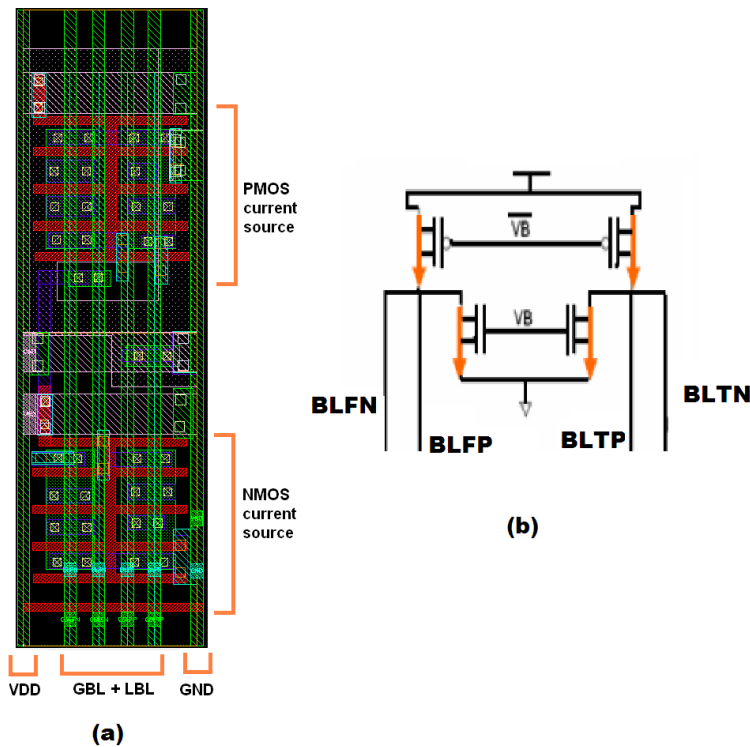


Figure 5.4: precharge circuit (a) layout (b) schematic

contributor to this inflation and the same situation is encountered with multiplexed 6T SRAM. The density is modest but can not be improved unless violation of DRC (SRAM implants).

In next section the mechanism of the generation of the pulse is detailed. The generation of the pulse is performed by the **Ctrl** (control) block.

### 5.1.2 Control block

Read operations are performed, as explained in Chapter 4, in three steps: first the data is copied from the bit-cell to a Lcell, secondly the data is copied from the Lcell to a Gcell and finally from the Gcell to a IOcell. So there is a need to create a state machine that creates the  $AXS<0:31>$ ,  $LAXS$ ,  $GAXS$ ,  $OAXS$  and  $PG$  pulses, according to read/write or retention mode as explained in figure 5.7. The control block is designed

## 5.1 Test chip design

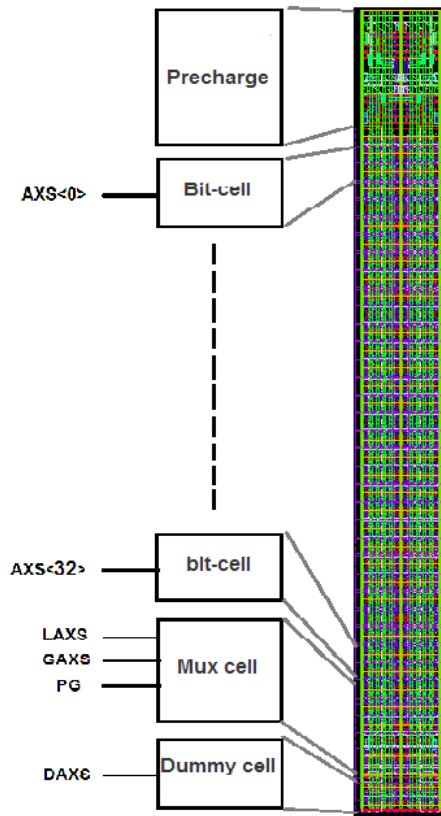


Figure 5.5: The Sub-matrix column arrangement

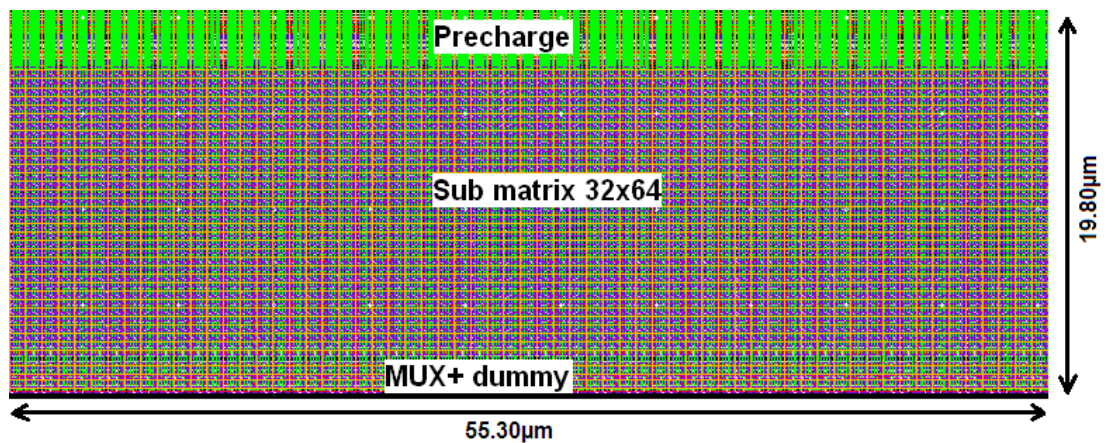


Figure 5.6: Sub-matrix array of  $32 \times 64$ , Mux cell, dummy line and precharge circuit

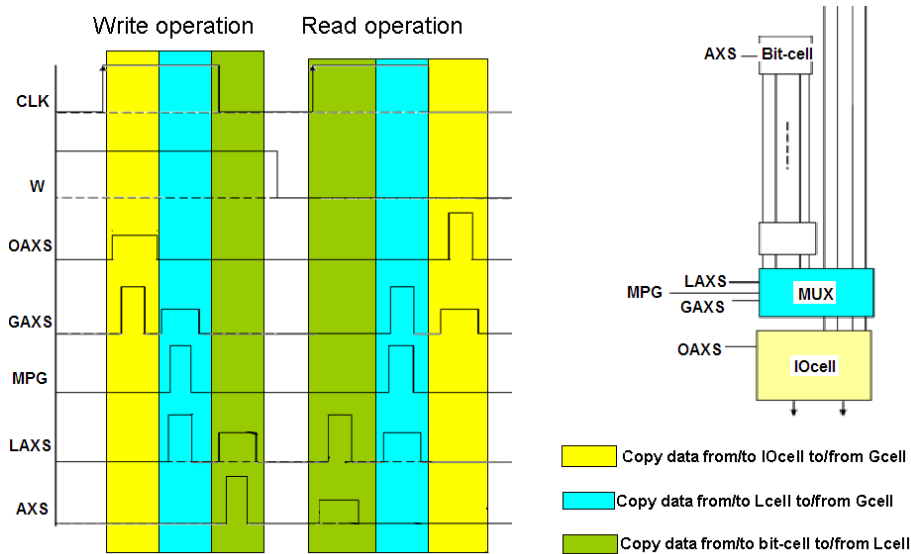


Figure 5.7: Pulse diagram generation according to write or read operations

in order to generate the three steps of a read or write operation in each clock (CLK) period. These steps are asynchronous so the pulses width and the steps' sequence must be generated automatically according to the PVT state. The PVT variability engenders a variation in the hard line copy delay. To solve this problem, the dummy bit-cell lines are used to estimate the pulse width necessary to the hard-line copy. The *Control* block can be divided into three sub-blocks. The *Pulse Generator* generates the Read Pulse (*RP*) and the Write Pulse (*WP*). The *Signal Generator* generates the pulses *pAXS*, *pLAXS*, *pGAXS*, *pOAXS* and *PG*. Finally the *WLDs* gives the pulse levels to performe the word line signals  $\text{texts}l_{\text{AXS}}\langle 0:31 \rangle$ , *LAXS*, *GAXS*, *OAXS* and *PG* (figure 5.8).

### 5.1.2.1 Pulse generator

The pulse generator block gives both pulses *RP* (read pulse) and *WP* (write pulse). *RP* is the pulse generated for the read bit-cell and *WP* is the pulse generated for the written bit-cell. For a good functionality the read pulse must be larger and encloses the write pulse. So the functionality of the pulse generator block is to perform the two

## 5.1 Test chip design

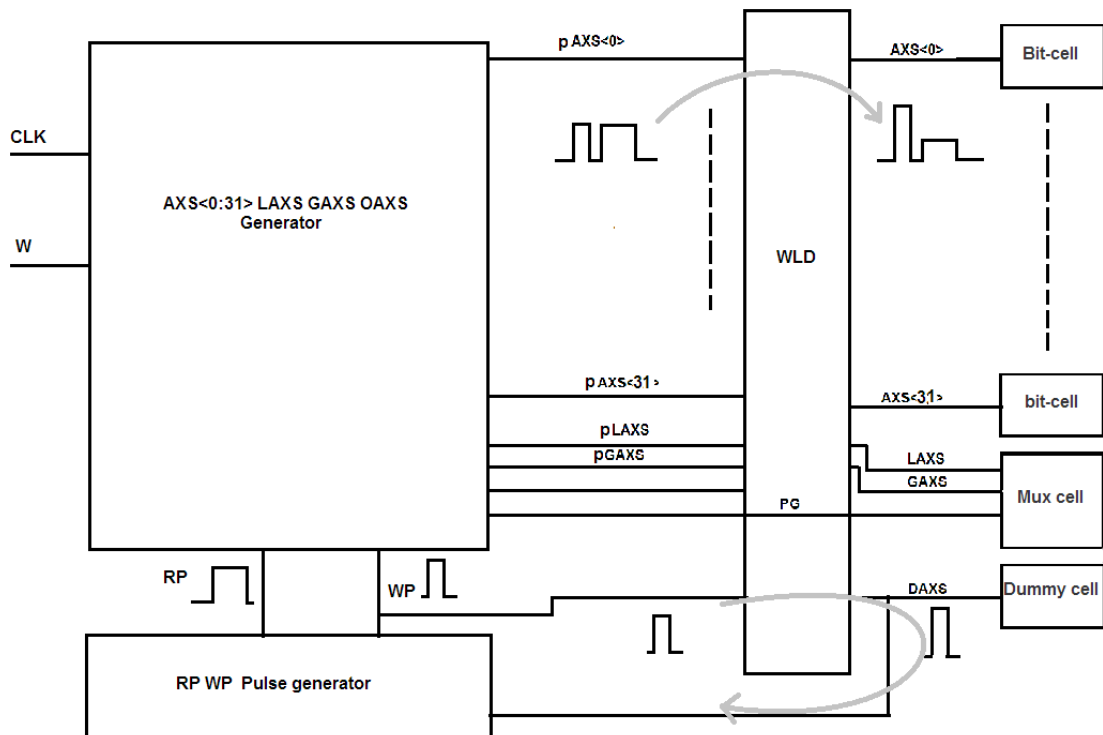


Figure 5.8: Control blocks with different input output signals

pulses in this configuration. The two pulses are generated in three steps: first the clock generates the positive edge of  $RP$  then the positive edge of  $RP$  generates the positive edge of  $WP$ . The  $DAX$  pulse, generated by the same pulse as  $WP$ , is connected to the  $V_{dd0}$  potential voltage and compared with  $V_{DD}$ . The negative edge of  $WP$  is generated when  $DAX$  value is larger than  $V_{DD}$  value (a voltage level comparator is used to compare  $DAXS$  and  $V_{DD}$ ). The  $WP$  negative edge generates the  $RP$  negative edge (figure 5.9).

The method used to create  $WP$  and  $RP$  allows to have different pulse widths according to the  $PVT$  corner. Using a dummy word line gives a feed back about the process state. In figure 5.8, the *Pulse Generator* activates the  $WP$  signal. This signal is transmitted to the  $WLD$  block and the dummy word line. The  $DAXS$  signal rises up depending on the line capacitance and resistance. The  $DAXS$  signal is sensed by the pulse generator to determine the duration of the  $WP$  signal pulse. This feed-back

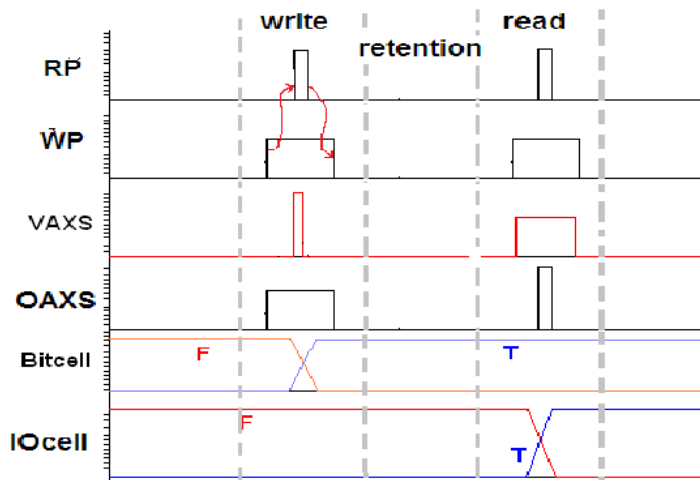


Figure 5.9: VAXS and OAXS in both write and read operation generated by WP and RP

action introduces a correction of PVT effects.

WP and RP are used to create the AXS<0:31>, GAXS, LAXS and OAXS by the *Signal Generator* block.

### 5.1.2.2 Signal Generator

Word line control signals are generated in two steps. The *Signal Generator* receives the WP and RP pulses and creates pAXS, pLAXS, pGAXS and pOAXS with the adequate chronogram (figure 5.8). The WLD block adjusts then the voltage level of the latter pulses. It determines the pulses width and secondly the level of these pulses is given by the WLD block. This different steps are explained in figure 5.8.

Table 5.2 gives some simplified logical equations for the generation of the pulses AXS, LAXS, GAXS and OAXS:

**Note:**  $S\uparrow$  is the positive edge of the signal S and  $S\downarrow$  is the negative edge of the signal S.

This equations are generated by the *Signal Generator* block with additional design details to insure the signal synchronicity.

## 5.1 Test chip design

---

| signal | logical equation  |
|--------|---|
| AXS    | $WP \cdot GAXS \downarrow \cdot W + CLK \uparrow \cdot WP \cdot \bar{W}$  |
| LAXS   | $WP \cdot GAXS \downarrow \cdot W + CLK \uparrow \cdot WP \cdot \bar{W} + OAXS \downarrow \cdot WP \cdot W + AXS \downarrow \cdot WP \cdot \bar{W}$ |
| GAXS   | $CLK \uparrow \cdot WP \cdot W + AXS \downarrow \cdot WP \cdot \bar{W} + LAXS \downarrow \cdot WP \cdot \bar{W} + OAXS \downarrow \cdot WP \cdot W$ |
| OAXS   | $LAXS \downarrow \cdot WP \cdot \bar{W} + CLK \uparrow \cdot WP \cdot W$  |

Table 5.2: Simplified logical equations for AXS, LAXS, GAXS, OAXS signals

### 5.1.2.3 Word line driver: WLD

As explained before, the *Signal Generator* block sets the pulse width and the *Word Line Driver* sets the pulses' level. The *WLD* is already presented in chapter 4. Figure 5.10 presents the *WLD* block. The *WLD* block contains the a *PMOS/NMOS* voltage divider for the read operation and a *PMOS* that connects the *AXS* signal to *Vddo* from the charge pump. Signals *Select<0:31>* are a bus of 32 bits from the *Ydecoder*. It select the targeted sub-matrix world line that will be read or written. So the *pAXS* signal is conducted to this word-line then the hard-line copy will be performed between this line and a *Lcell* line.

In these three blocks (*Pulse Generator*, *Signal Generator* and *WLD*), the required voltage levels are set for the targeted world-line according to write or read operation. These blocks are repeated in each sub-matrix to reduce the dynamic power consumption by reduction of the capacitances of signal wires and also of the delay of logical operations. The size of the sub-matrix with its control blocks is  $1784.475 \mu\text{m}^2$ . At this level the bit equivalent area is  $0.871 \mu\text{m}^2$ . The control blocks introduce an inflation of 63% of silicon area in the sub-matrix arrangement. Figure 5.11 presents waveforms of transient simulation results of different pulses and cells' internal nodes in both read and write operations. Next section presents the *Ydecoder* that generates the *Select<0:31>* signal used to select the targeted word line.

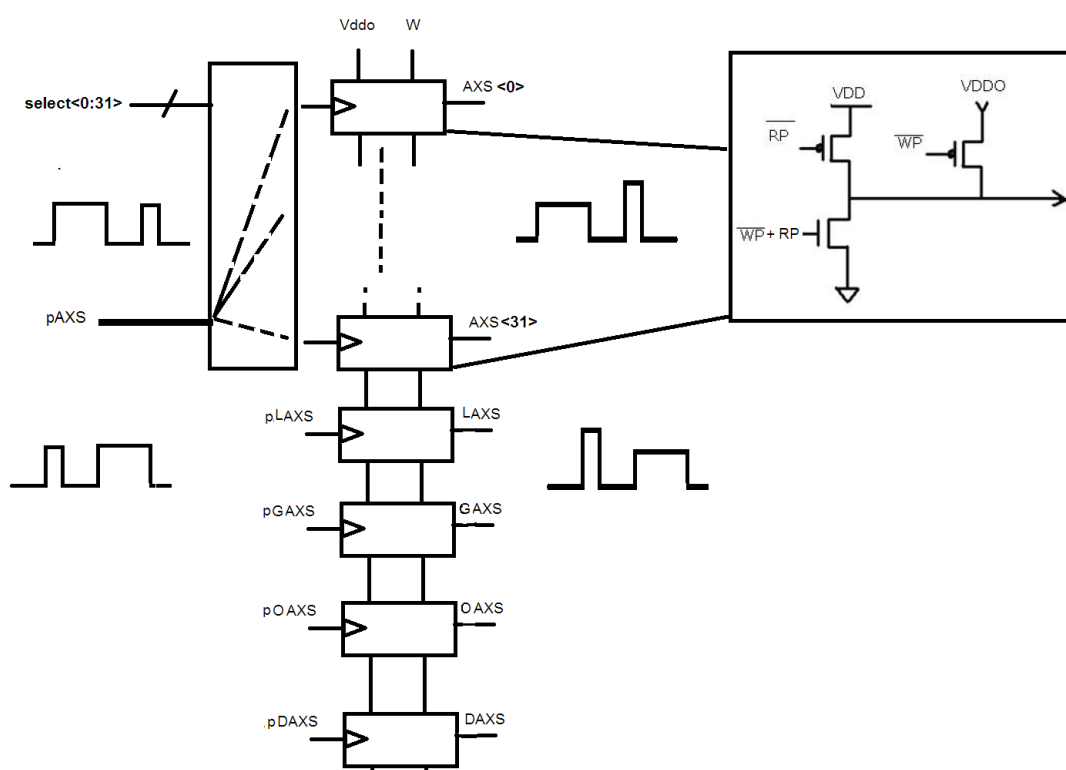


Figure 5.10: WLD block with different input and output signals

### 5.1.3 Y decoder

The dynamic power consumed in a decoding operation is given by (5.1), while  $f$  is the operating frequency,  $N$  the number of changing bits (charging and discharging wire),  $C$  wires' capacitances and  $V$  wires potential voltage. As explained in (5.1) the power consumption is proportional to the number  $N$  of the transition on the wires used to transmit the decoded data.

$$P_{dyn} = f \times N/2 \times C \times V^2 \quad (5.1)$$

In order to reduce the dynamic power consumed in the *Ydecoder* a technique of pre-decoding is implemented. This technique consists in partially decode a part of the address word in order to reduce the number of the transitions on the long address wires

## 5.1 Test chip design

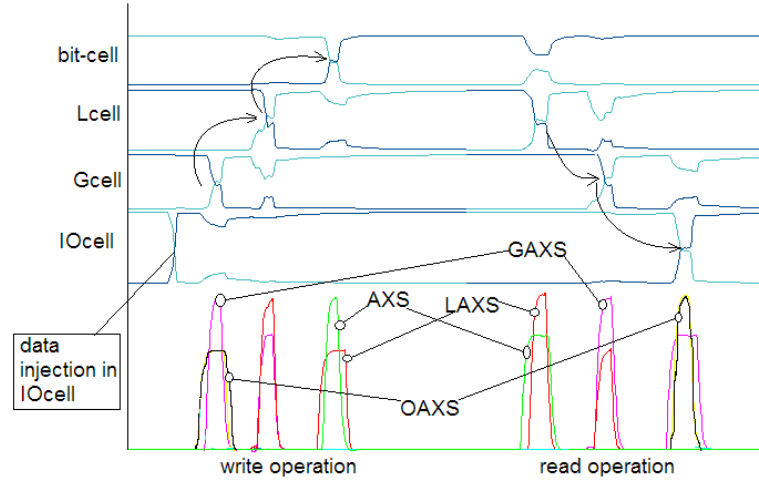


Figure 5.11: Cell's internal nodes voltages and AXS signals in both write and read operations

used to transmit the address data across the memory cut. The 1024 word lines are encoded in 10 bits,  $A\langle 0:9 \rangle$ . The address word  $A\langle 0:9 \rangle$  is divided into 2 parts  $A\langle 0:4 \rangle$  (LSB) and  $A\langle 5:9 \rangle$  (MSB). The address bit  $A\langle 0:4 \rangle$  (LSB) are used to select a sub-matrix word line and the address bit  $A\langle 5:9 \rangle$  (MSB) are used to select the active sub-matrix between the 32 sub-matrices. The five bits of the MSB and LSB are predecoded respectively as explain in figure 5.12. The three bits  $A\langle 0:2 \rangle$  (respectively  $A\langle 5:7 \rangle$ ) are decoded into the  $2^3=8$  bits,  $i\langle 0:7 \rangle$  (respectively  $I\langle 0:7 \rangle$ ) and the two bits  $A\langle 3:4 \rangle$  (respectively  $A\langle 8:9 \rangle$ ) are decoded into the  $2^2=4$  bits,  $h\langle 0:3 \rangle$  (respectively  $H\langle 0:3 \rangle$ ). The 8 bits  $i\langle 0:7 \rangle$  and the 4 bits  $h\langle 0:3 \rangle$  are used in *Local Ydecoder* to define the  $8 \times 4=32$  bits of the data bus  $Select\langle 0:31 \rangle$ . The same operation is made with the 8 bits  $I\langle 0:7 \rangle$  and the 4 bits  $H\langle 0:3 \rangle$ , they are used in *Matrix select* to define the  $8 \times 4=32$  bits of the data bus  $Msel\langle 0:31 \rangle$  used to select the active sub matrix. With the predecoding technique, the maximum number of transactions on the wires  $i\langle 0:7 \rangle$  and  $h\langle 0:3 \rangle$  (respectively  $I\langle 0:7 \rangle$  and  $H\langle 0:3 \rangle$ ) is 2 instead of 5 in the address bus  $A\langle 0:4 \rangle$  (respectively  $A\langle 5:9 \rangle$ ). With this technique, according to (5.1), the decoding dynamic power consumption is reduced by  $1 - \frac{2}{5}=60\%$ .



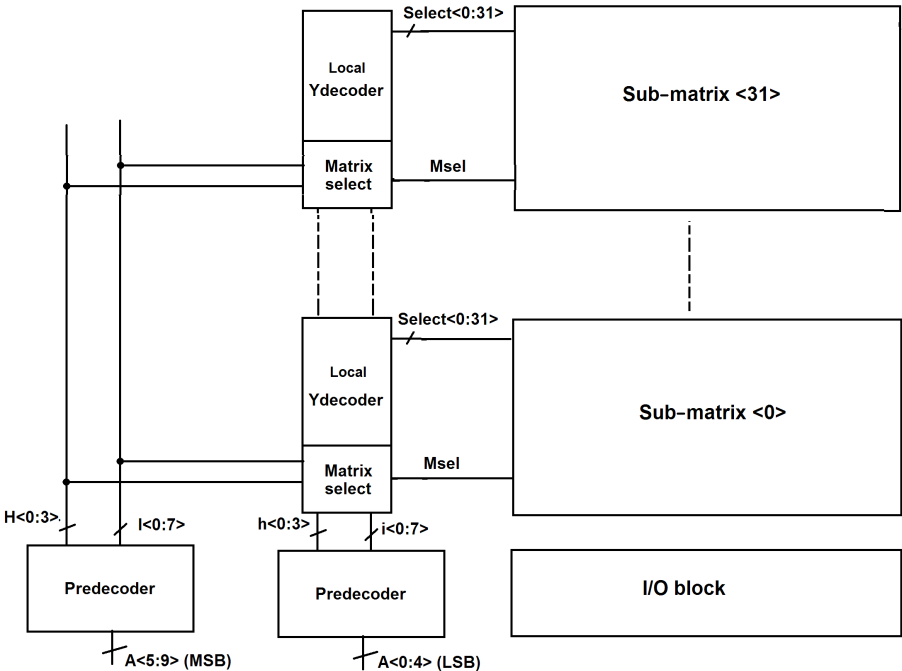


Figure 5.12: Ydecoder for both sub-matrix word line selection and sub-matrix selection

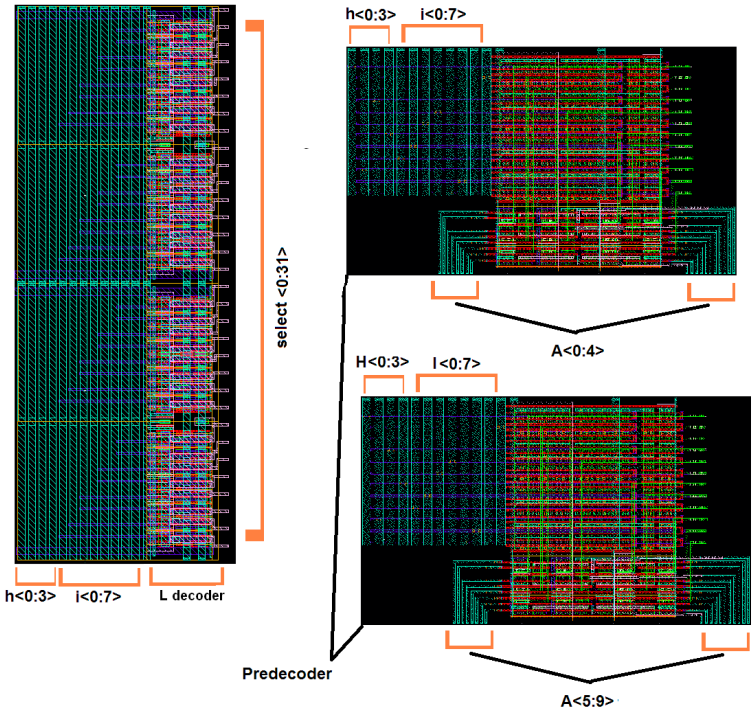


Figure 5.13: Local decoder and predecoder layout

## 5.1 Test chip design



Figure 5.14: Layout of the sub-matrix including Matrix array, Control block, Mux, and Ydecoder

Figure 5.13 presents the layout of the *Local decoder* and the *Predecoder* with their input/output signals. Figure 5.14 presents the global sub matrix, with the matrix array, Mux, Control and local Ydecoder.

### 5.1.4 Input/Output

Input and output interfaces are ensured by the *IOcell* (figure 5.15). The data  $D$  and  $\bar{D}$  are injected into the *IOcell* via the pass gate activated by the signal  $WE$ . The data  $Q$  and  $\bar{Q}$  are sensed from the *IOcell* by the two inverters connected to the *IOcell* internal nodes. The write operation is made as detailed before: the data is set at  $D$  and  $\bar{D}$  then injected in *IOcell* by activating the signal  $WE$ . The hard line duplication steps are then performed. In read operation after the data is copied into *IOcell*,  $Q$  data is latched to keep the read word at the memory output.

The memory Cut is then obtained by stacking the 32 sub-matrices and connected by the global bit-lines. *IOcells* line is added at the bottom of the sub-matrices and connected to the global bit-lines. Figure 5.16 presents the full cut layout with its 32 sub-matrices and Input and Output interfaces.

The cut silicon area is  $64261.3\mu\text{m}^2$ . The equivalent bit area is finally  $0.980\mu\text{m}^2$ . There is a small room for improvement in the cut layout as this issue has not received a large attention because the first objective of the testchip was to demonstrate the Portless

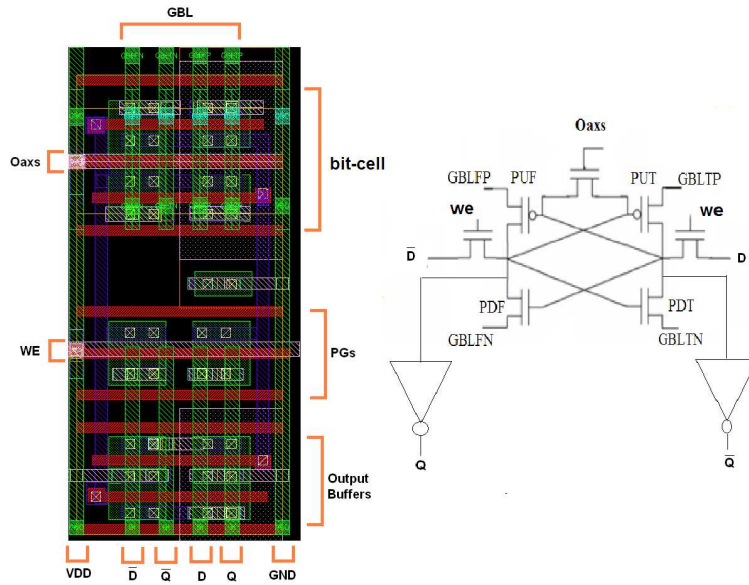


Figure 5.15: Schematic and layout of IOcell with  $Q$  and  $\bar{Q}$  output data and  $D$  and  $\bar{D}$  input data

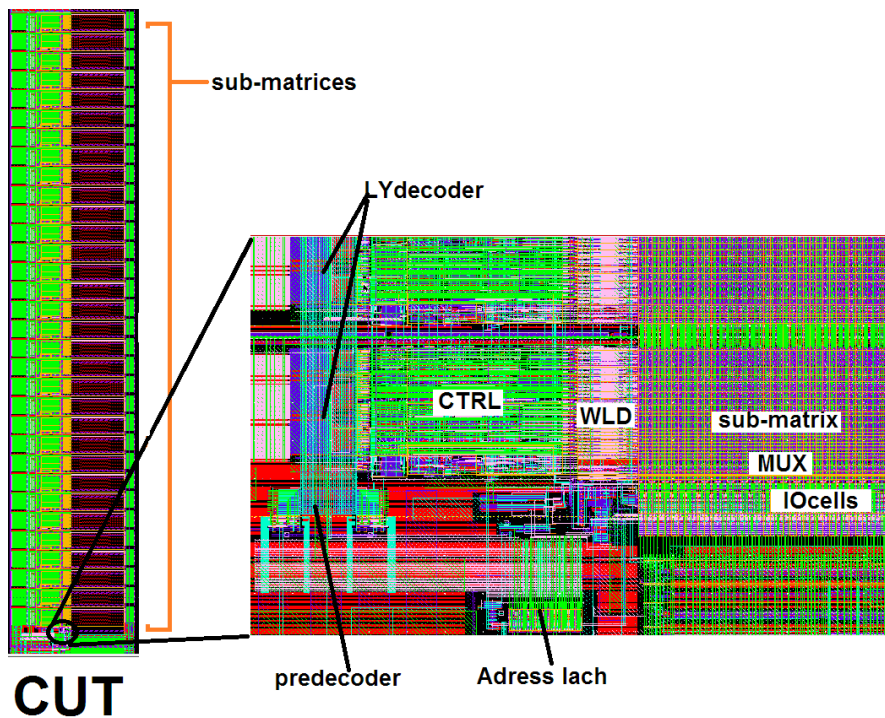


Figure 5.16: Cut layout with the 32 sub-matrices and Inpu/Output interfaces

## 5.2 Simulation results

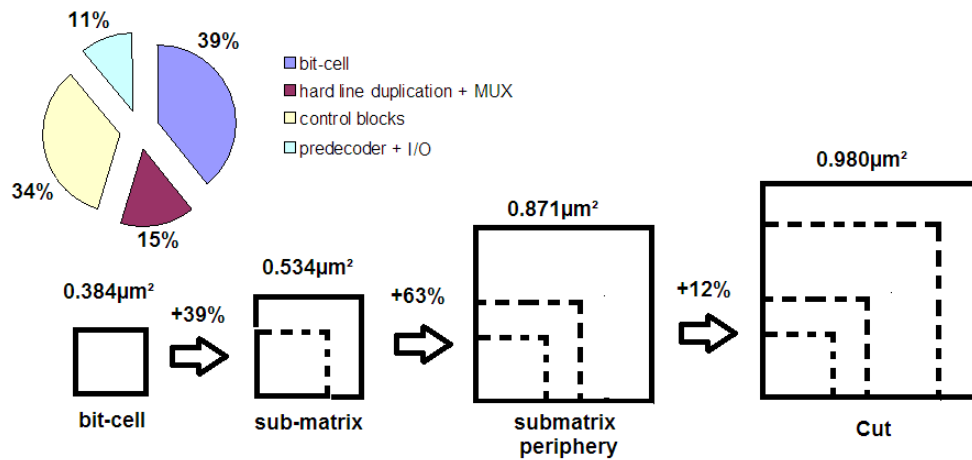


Figure 5.17: Bit effective area

operability in 32nm. Figure 5.17 pictures the contributors to the effective bit silicon area. The bit-cell weights 40% of the bit effective area. The hard line duplication technique and multiplexers occupy 49% including the control blocks. It is the price to pay for the bit-cell performances. The control blocks (34% of the area) have not been optimized in layout and extra spaces have been managed in advance of an eventual correction of the testchip.

## 5.2 Simulation results

The full cut contains more than  $4 \cdot 10^5$  transistors. Simulating the full cut with "Eldo" takes several hours for just one cycle of write/retention/read operations. Two approaches are developed to overcome this simulation issue. First it is possible to lighten the netlist by creating a *Critical Path* that represents just the set of necessary bit-cells or columns where the targeted parameters (delay, consumption, functionality ...) should appear in a worst case. The rest of the cut is replaced by its equivalent load (figure 5.18). The load is modeled as an RC delay. Resistance and capacitance values are estimated from the extracted netlist (full LVS). A second approach is to simulate the

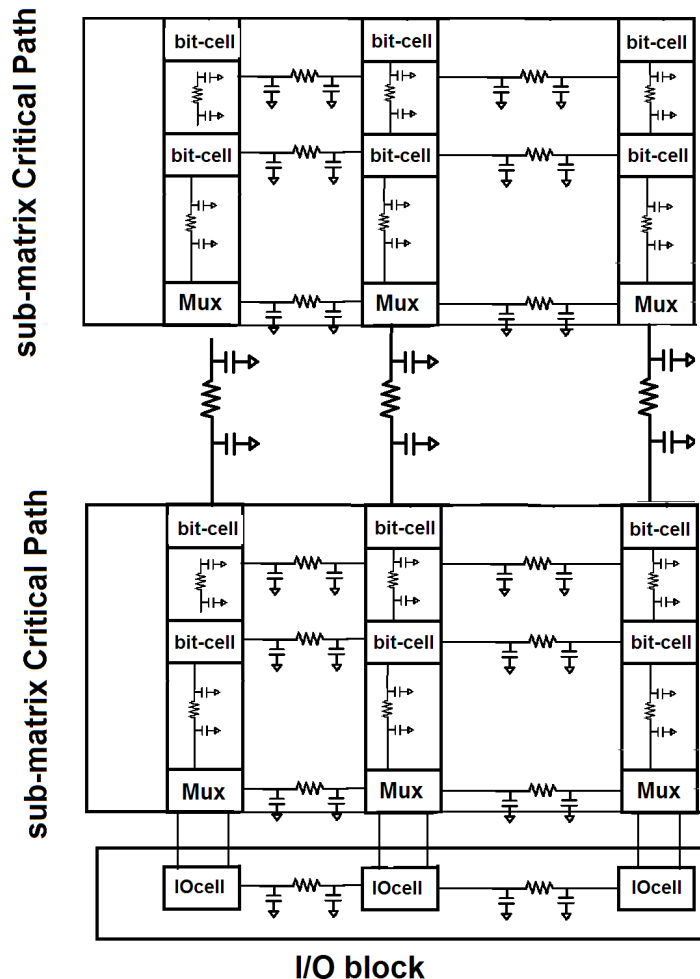


Figure 5.18: A critical path in the matrix array with the critical bit-cells to be simulated

full cut using the extracted netlist but not with Eldo. The "xa" simulator has been developed for this purpose. The simulations with "xa" are performed for ensuring the functionality in the different PVT corners. The extraction of the parameters are performed by the *Critical Path* simulated by "Eldo". The simulation of the *Critical Path* takes up to 10 to 15 minutes depending on the server machine performances. A simulation with "xa" takes 20 to 30min also depending on the server machine performances.

Parameters in Table 5.3 are extracted from the *Critical Path* simulations. To evaluate the effects of the process variability, Monte-Carlo simulation are not considered

## 5.2 Simulation results

---

because of its cost in simulation, computer resources and data size. The simulations are performed in the conditions of the 4 corners FF, FS SF and SS. Parameters in the *Design Kit* are evaluated at  $3.5\sigma$  from the TT corner so verifying the performances in the 4 possible corners gives a first level of confidence. The parameters presented in Table 5.3 are extracted from the full set of PVT corners presented in Table 5.1 (45 PVT corners are simulated).

| parameter | leakage | Iread | read delay | Write delay | dynamic power            |
|-----------|---------|-------|------------|-------------|--------------------------|
| unit      | A       | A     | s          | s           | $\mu\text{W}/\text{Mhz}$ |

Table 5.3: Extracted parameters from the critical path simulation

Figure 5.19 presents simulated waveforms in read and write operations at different address lines in the memory cut using the full cut netlist extracted from the layout, including the parasitic devices ("xa" simulator). The different steps of the hard line duplications are presented. The read delay is the delay between the *CLK* positive edge and the transition on the signal *Q* in read mode (*WEN*=1). The write delay is the delay between the *CLK* positive edge and the transition on the bit-cell data.

Write and read delays depend on the PVT corners. Figure 5.20 shows different values for the read delay versus the PVT corners. The read delay worst case is in case of SF corner (slow NMOS and Fast PMOS) for different  $V_{DD}$  and temperature values. The maximum value of the read delay is for  $V_{DD}=0.9\text{V}$  and  $\text{Temp}=-40^\circ\text{C}$ . The best case for the read delay is in case of the FS corner (Fast NMOS and Slow PMOS) and the minimum read delay is for  $V_{DD}=1.1\text{V}$  and  $\text{Temp}=125^\circ\text{C}$ . The write delay is affected in the same manner.

Table 5.4 presents the worst case and best case for the read and write delays and the typical values. The best case for the similar delays in a 6T SRAM structure are for the FF corner, 1.1V, 125°C (best case, where the process is fast) and the SS corner, 0.9V, -40°C (when the process is slow). The operation delay in the Portless structure depends on the current difference between the bit-lines. The current difference is



## 5 Test chip and simulation results

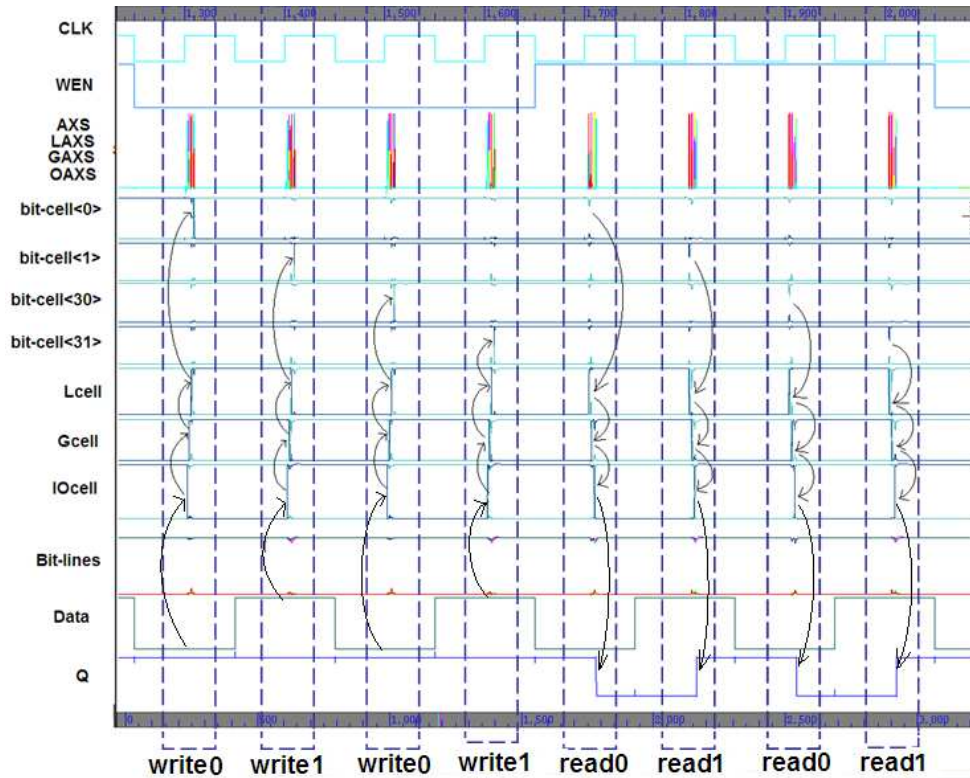


Figure 5.19: Simulation of read and write operations for the full memory cut using the simulator

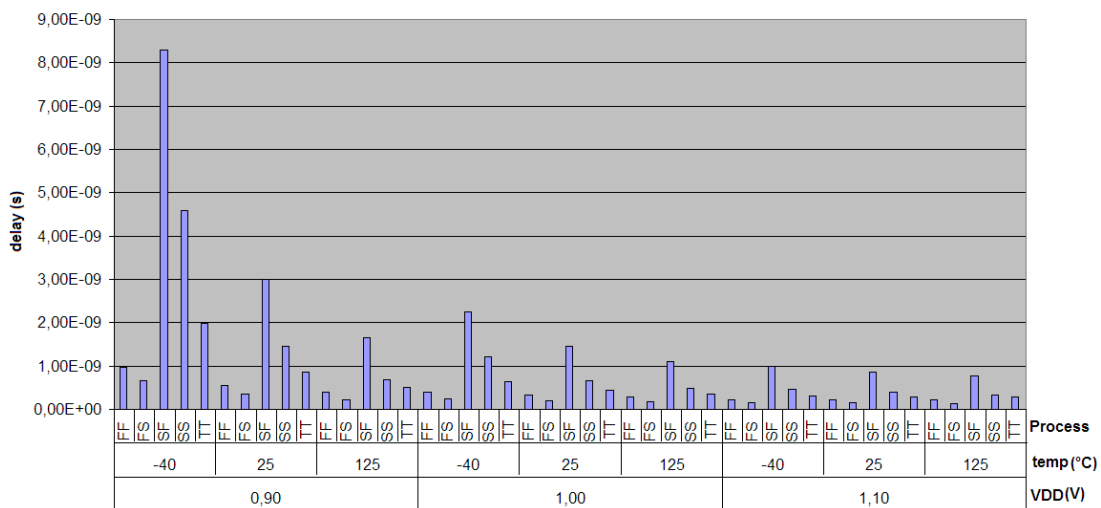


Figure 5.20: Simulation results for the read delay (Critical Path simulation with Eldo)

## 5.2 Simulation results

| process | temperature ( $^{\circ}C$ ) | $V_{DD}$ (V) | Read delay (ns) | Write delay (ns) |
|---------|-----------------------------|--------------|-----------------|------------------|
| TT      | 25                          | 1            | 1.3             | 1.4              |
| SF      | -40                         | 0.9          | 7               | 8.3              |
| FS      | 125                         | 1.1          | 0.7             | 0.5              |

Table 5.4: Hard line duplication delay in different PVT corners

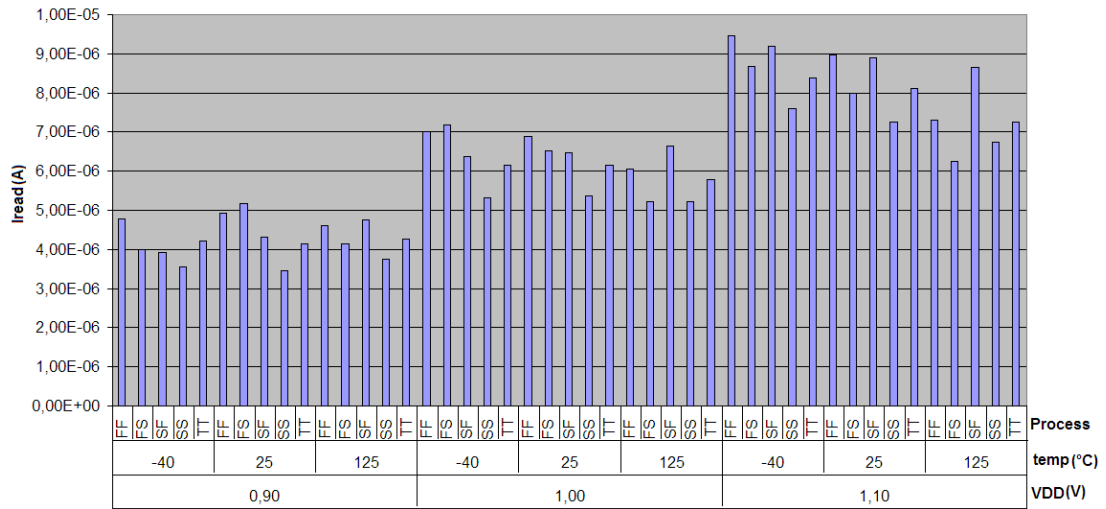


Figure 5.21: Bit-cell read current for different PVT corners

created by the bit-cell read current.

Figure 5.21 presents the bit-cell read current in the different PVT corners. It is clear that the read current depends essentially on the power supply  $V_{DD}$  and there is not a big difference between the fast and slow processes. Actually the bit-lines current difference doesn't depend only on the read current but also on the leakage current induced by the rest of the bit-cells in retention mode.

Figure 5.22 presents the current difference induced by a bit-cell in a retention mode. In the FS corner the current difference induced by the bit-cell is less than the current difference induced by the bit-cell in SF corner. The impact on the bit-line current difference is more important when the number of column bit-cells is important. However the leakage current induced by a bit-cell, as explained in figure 5.22 in the FS corner is more important than in the SF one.



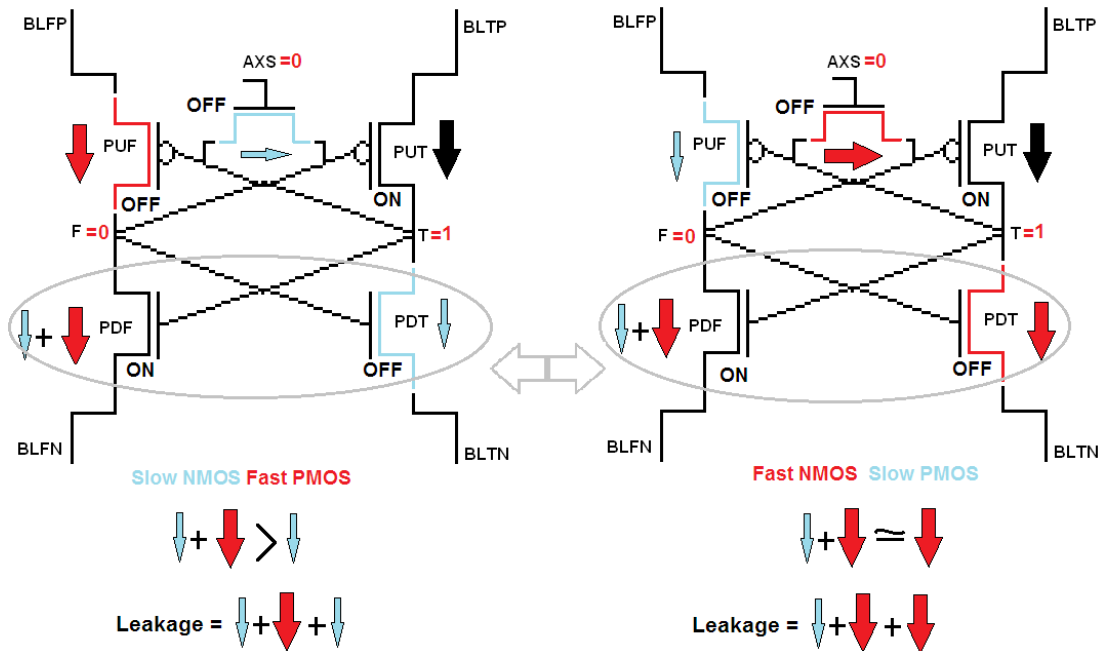


Figure 5.22: Leakage current difference induced by a bit-cell in the retention mode and the total bit-cell leakage in both FS and SF corners

Figure 5.23 presents the bit-cell leakage in different PVT corners, it is clear that the leakage in the FS corner is more important than in the SF one as detailed in here-above. The maximum value of the leakage is noted for the corner FF, 1.1V, 125°C and the smallest is noted for the corner SS, 0.9V, -40°C, what corresponds to the classical maximum and minimum leakage corners. Tables 5.5, 5.7 and 5.6 present the leakage variations versus process corners.

| Process | leakage (normalized to typical value) |
|---------|---------------------------------------|
| TT      | 1,00                                  |
| SS      | 0,53                                  |
| SF      | 0,92                                  |
| FS      | 1,39                                  |
| FF      | 2,26                                  |

Table 5.5: Bit-cell leakage values for different process corners in case of ( $V_{DD}=1V$ , Temp=25°C )

## 5.2 Simulation results

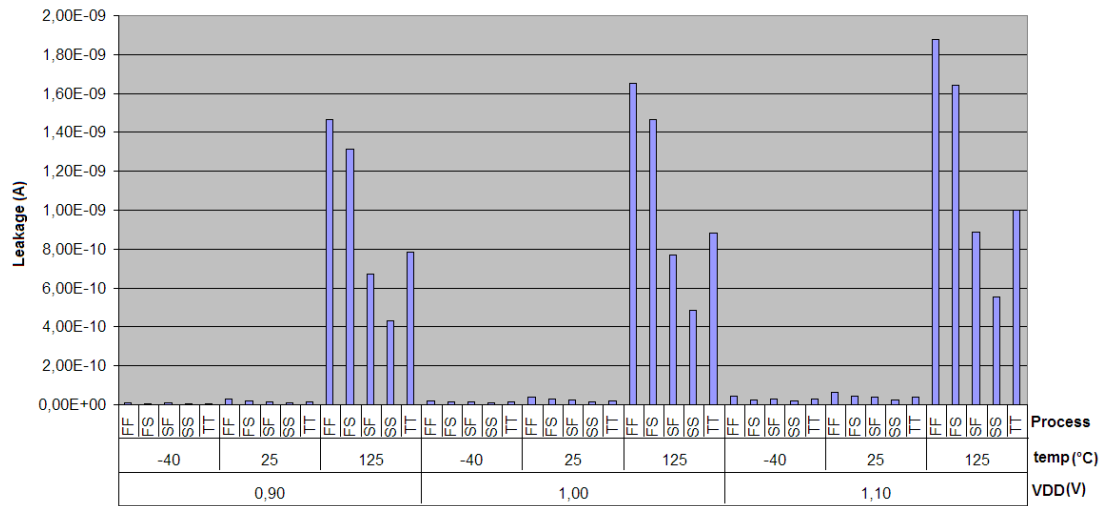


Figure 5.23: Bit-cell leakage in different PVT corners, simulated by Eldo in CMOS 32nm

| Process | leakage (normalized to typical value) |
|---------|---------------------------------------|
| TT      | 1,00                                  |
| SS      | 0,54                                  |
| SF      | 0,88                                  |
| FS      | 1,63                                  |
| FF      | 1,90                                  |

Table 5.6: Bit-cell leakage values for different process corners in case of ( $V_{DD}=1.1V$ ,  $Temp=125^{\circ}C$ )

| Process | leakage (normalized to typical value) |
|---------|---------------------------------------|
| TT      | 1,00                                  |
| SS      | 0,62                                  |
| SF      | 0,93                                  |
| FS      | 1,10                                  |
| FF      | 2,17                                  |

Table 5.7: Bit-cell leakage values for different process corners in case of ( $V_{DD}=0.9V$ ,  $Temp=-40^{\circ}C$ )

| Process | $V_{DD}$ (V) | Temp ( $^{\circ}C$ ) | leakage (nA) |
|---------|--------------|----------------------|--------------|
| TT      | 1            | 25                   | 3,33         |
| FF      | 1.1          | 125                  | 195,35       |
| SS      | 0.9          | -40                  | 0,76         |

Table 5.8: Bit-cell leakage values in typical, fastest and slowest corners

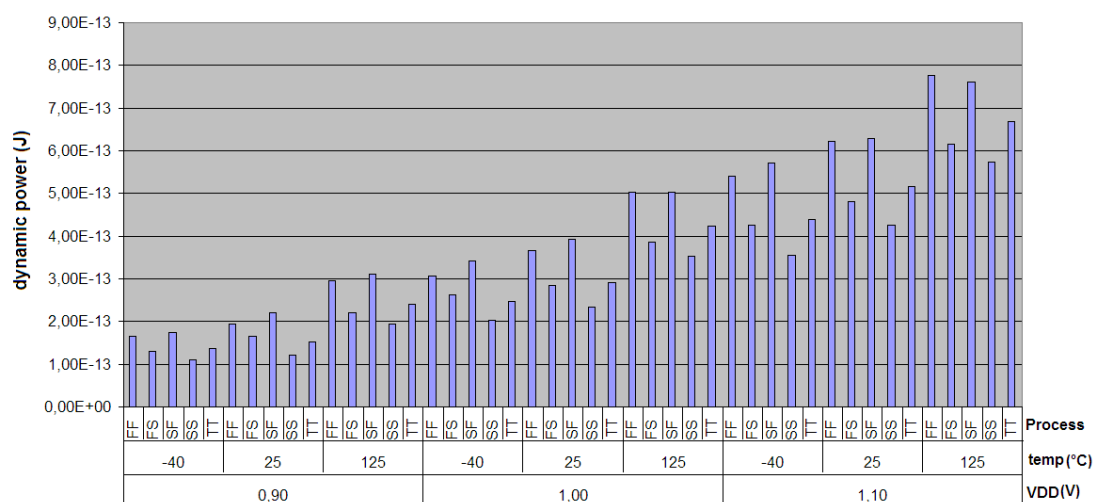


Figure 5.24: Dynamic power consumption during a read operation in different PVT corners

| corner                                   | TT, 1V, 25°C | FF, 1.1V, 125°C |
|--|--------------|-----------------|
| dynamic power 5T-Portless( $\mu$ W/ Mhz) | 7,01         | 49.2            |

Table 5.9: Dynamic power consumption of the full cut in typical and worst case corners

The most significant parameter for the leakage is still classically the temperature. Table 5.8 presents the maximum value of the bit-cell leakage, seen for the corner FF, 1.1 V, 125°C, and the minimum value, seen for the corner SS, 0.9V, -40°C.

Figure 5.24 presents the dynamic power consumption during a read operation. As discussed in chapter 2, the power consumption rises with power supply  $V_{DD}$  and the temperature. The minimum value is noted for the SS corner and the maximum for FF one. The power consumption in FS corner is less than SF corner because the read delay in SF is more important than SF one. So the read current is consumed during longer duration in SF case than FS case. The same behavior is observed in write operation, because of the symmetrical phenomena between read and write operations.

Table 5.9 presents the power consumption in read and write operations both for the typical and worst case corners. A comparison with a 6T SRAM enables to appreciate the improvement on many of the Portless performance parameters.

## 5.2 Simulation results

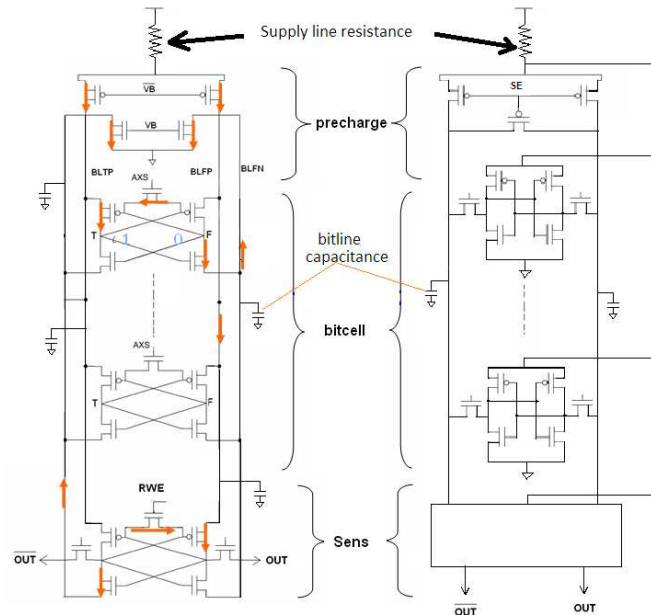


Figure 5.25: Comparison of 6T SRAM column and Portless column

### 5.2.1 Comparison with the 6T SRAM

In 6T-SRAM structure, read/write operations are driven by voltage: bit-lines need to be charged and discharged and the voltage sense amplifier at the bottom of a column uses the bit-lines' voltage difference to output the data. In the 5T-Portless structure, the data is detected by a current difference between bit-lines (Figure 5.25). Bit-lines are directly connected to the sources of the bit-cell transistors and also ensure the bit-cell supply. The *hard-line copy* technique allows to keep bit-lines voltage at  $V_{DD}$  in retention, write or read operation.

The hard-line copy in Portless structure offers a large gain in dynamic power consumption because bit-lines are not charged nor discharged at every write or read operation. Bit-cells in a same column are not disturbed by operation on one of them. The dynamic current waveform in a 6T-SRAM presents many spikes, the highest ones are when charging the bit-lines' capacitances that are discharged during write or read operation. In a 5T-Portless there is no significant current spikes as compared to the 6T-

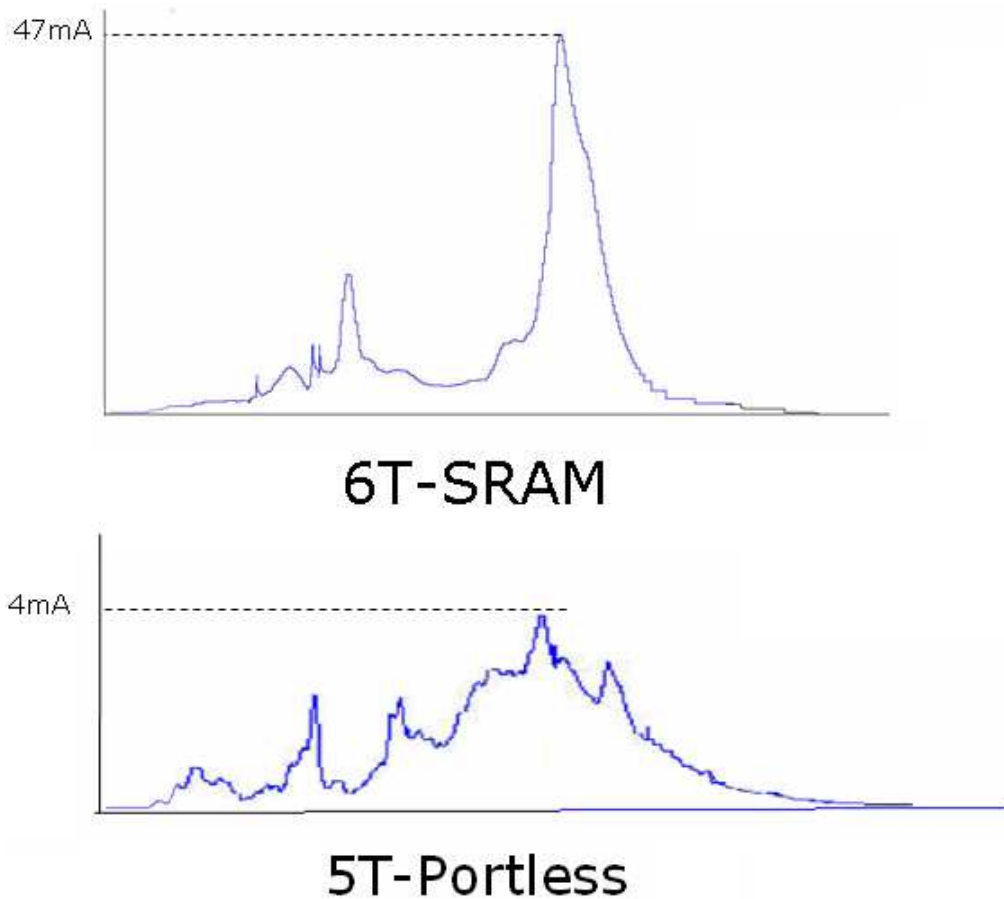


Figure 5.26: Current waveforms during read and write operations in both 6T and Portless SRAM

SRAM structure: a mean-value current corresponds to the bit-cell  $I_{read}$ . Figure 5.26 compares the current waveforms of two same size matrix of 5T-Portless and 6T-SRAM structures ( $1024 \times 64$  bits).

6T-SRAM column presents a current spike of 47mA. In the 5T-Portless, the highest current spike is 4mA. The current average value in 5T-Portless column is less than that in a 6T-SRAM. The supply line effective resistance creates a voltage drop  $\Delta V$ , which gives birth to the so-called *IR drop* effect [51], proportional to current spikes due to the read/write operations. This affects the bit-cell stability and read/write yield.

### 5.3 Testchip Results

---

| corner                    | TT, 1V, 25°C | FF, 1.1V, 125°C |
|---------------------------|--------------|-----------------|
| leakage Portless RVT cell | 3,32609E-11  | 6,30244E-09     |
| leakage 6T(H187) cell     | 5,5E-11      | 9,65E-09        |
| leakage Portless vs 6T    | -39,53%      | -34,69%         |

Table 5.10: Leakage current values comparison between Portless and 6T SRAM bit-cells

| corner   | TT, 1V, 25°C | FF, 1.1V, 125°C |
|--|--------------|-----------------|
| power dynamic 5T-Portless ( $\mu\text{W}/\text{Mhz}$ ) | 7.01         | 12.31           |
| 6T SRAM cut (1024x64) ( $\mu\text{W}/\text{Mhz}$ )     | 10.65        | 14.84           |
| power dynamic 5T vs 6T                                 | -0.34%       | -0.17%          |

Table 5.11: Leakage current values comparison between Portless and 6T SRAM bit-cells

Current mode read/write in Portless is immune from  $V_{DD}$  fluctuations due to current spike.

Table 5.10 presents a comparison of leakage current in Portless bit-cell and 6T SRAM (typical corner). A gain of 39% in static consumption is observed in the case of the typical Corner in favor of the Portless.

Table 5.11 presents dynamic power comparison between Portless and 6T SRAM. A gain of 34% is noted in typical corner and 17% in worst case.

Next section gives a summary of the available measurements on the 32nm testchip submitted for fabrication by Samsung.

## 5.3 Testchip Results

The test chip has been designed with RVT transistors as offered by the design kit (Regular  $V_{th}$ ). Standard DRC rules have been applied. The periphery is not voluntarily optimized to guarantee the functionality in CMOS 32nm (space reserves have been managed in anticipation of correction of the first testchip). It was known at the time of submission to fabrication that the results obtained for delays, Leakage and dynamic

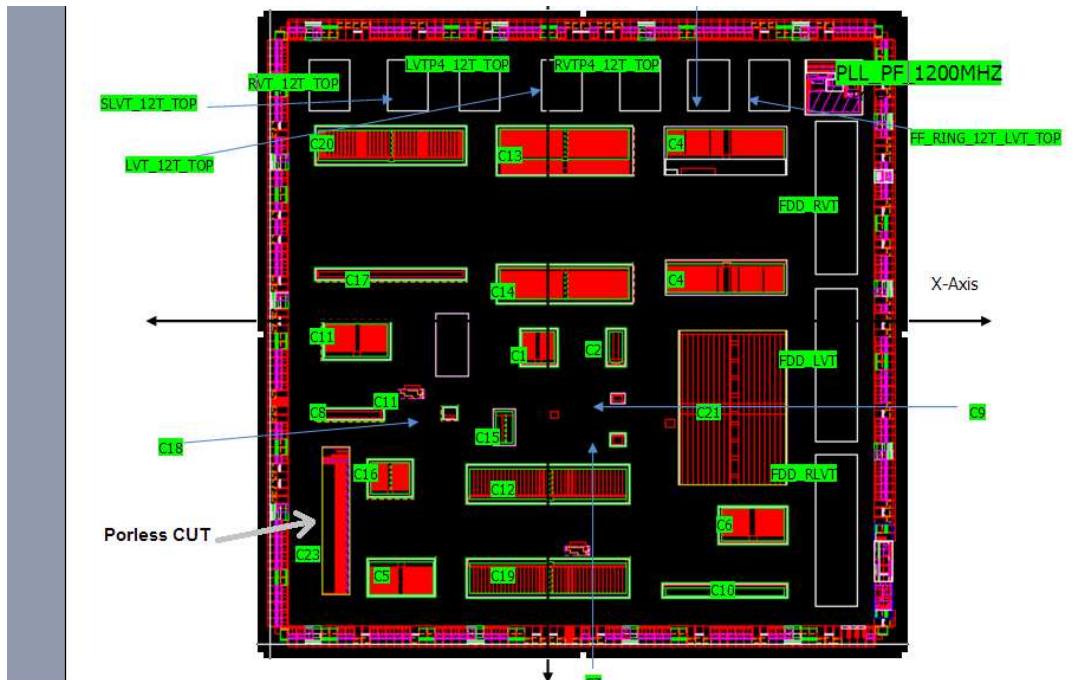


Figure 5.27: Portless CUT with other memories and logical IPs

power could be improved with an effort on the process (usage of the SRAM implants for Portless SRAM) and also with an effort on the periphery (layout optimization, dynamic decoder ...).

The Portless Cut has been implanted in a global Testchip called NAMASTE32LPA. This testchip is in fact following a primary circuit in 32nm that was delivered as untestable (major problem on ground grid). The NAMASTE32LPA contains, in addition to the Portless Cut, other memory CUTs (6T SRAM), Standard cells and ROs (Ring oscillators) for process characterization and library optimization.

### 5.3.1 Test Chip environnement

The NAMASTE testchip as delivered, is not functional, i.e. the IC does not meet the requirements of the technology maturity. This indicates at least a major deviation at one time in the process flow. An investigation has shown that the fabrication has suf-

### 5.3 Testchip Results

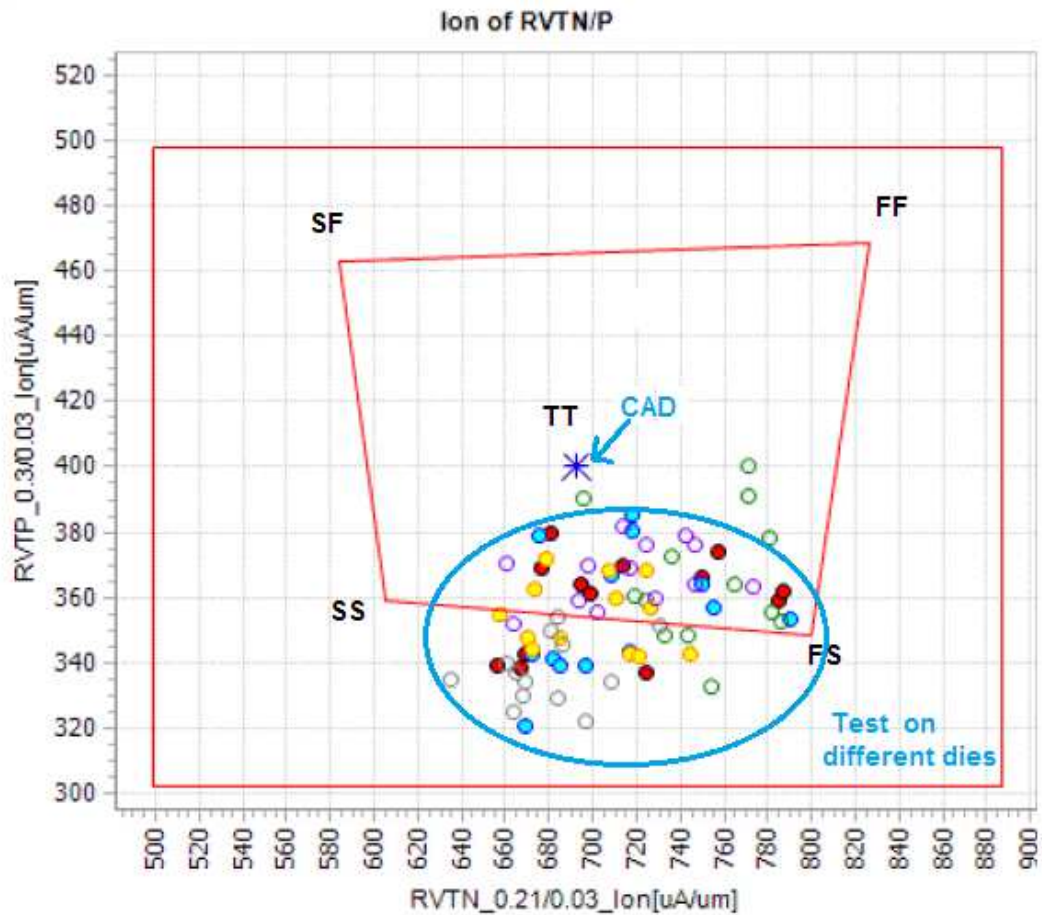


Figure 5.28: Values of  $I_{ON}$  of NMOS and PMOS given by the CAD and test chip measurements

ferred many alterations. For the ROs and standard cells, it was observed low values for the NMOSFET dynamic current,  $I_{dyn}$ , at  $125^{\circ}\text{C}$  compared to the CAD values. Values above CAD ones were observed under  $30^{\circ}\text{C}$ . In frequency the values are under the ones given by the CAD except at  $125^{\circ}\text{C}$ .

Figure 5.28 presents the  $I_{ON}$  value of NMOS and PMOS, given by CAD and some measurements extracted from the test chip. The process is rather FS and SS, and a big part of values are out of SS, SF, FS, FF boxes given by CAD.

A 10% yield drop is observed in standard logic IPs. In memories, a yield drop



is also evaluated at least of 10% and near to 17%. The maximum frequency of ring oscillators observed in the test chip is under the pessimistic values given by the CAD. The leakage measured for different blocks in the test chip are largely above the CAD ones.

The test chip report concludes that wide devices are out of specifications. Other devices are close to the specifications but not on target. Wide devices behavior makes the silicon vs CAD comparison difficult for memories (given the variety of transistors width in memory peripheries). It is impossible to conclude on the Portless functionality. CMOS 32nm industrial maturity cannot be performed on this lot. A new silicon is needed to prove first the industrial maturity of the CMOS 32nm. Then it will be possible to verify the performances of the NAMASTE testchip.

### 5.3.2 Portless Results

The large variation on the measurement dynamic current and leakage current is indicative of a high drop in fabrication yield. The large difference between CAD and silicon results, makes it difficult to characterize the memory cut. As is the case for the other devices, the leakage measurement on the Portless Cut is largely above results obtained on CAD (Figure 5.29). The dynamic power is in specification for temp=125°C but above CAD for temp=-40°C (Figure 5.30).

As concluded in the test chip report, a new silicon is needed to validate the portless memory cut. During the period of test chip manufacturing, the *Design Kit* has been updated. A new NAMASTE test chip was scheduled using this new *Design Kit*. It includes some DRC modifications, so some modifications are demanded in the layout (essentially on the VIAs). Also some modifications on the design are needed because characterizations of the transistors have changed. The Portless memory Cut was redesigned in accordance to the new *Design Kit* and including the optimization that were identified at the time of the first design. The *Word Line Driver* sizing and the

### 5.3 Testchip Results

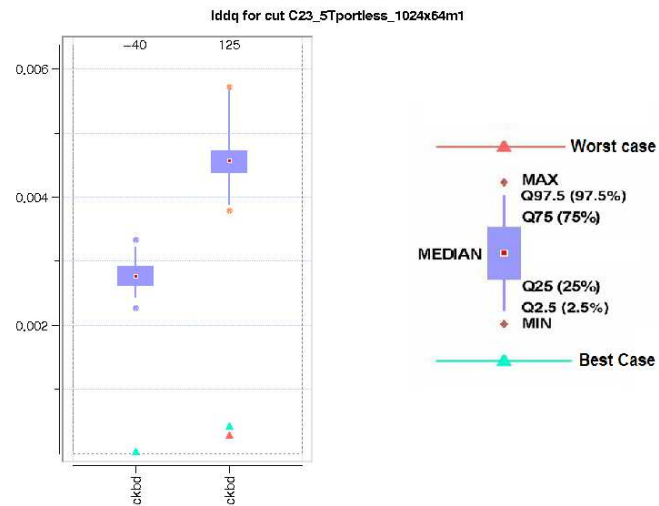


Figure 5.29: Test chip results for the full cut leakage current

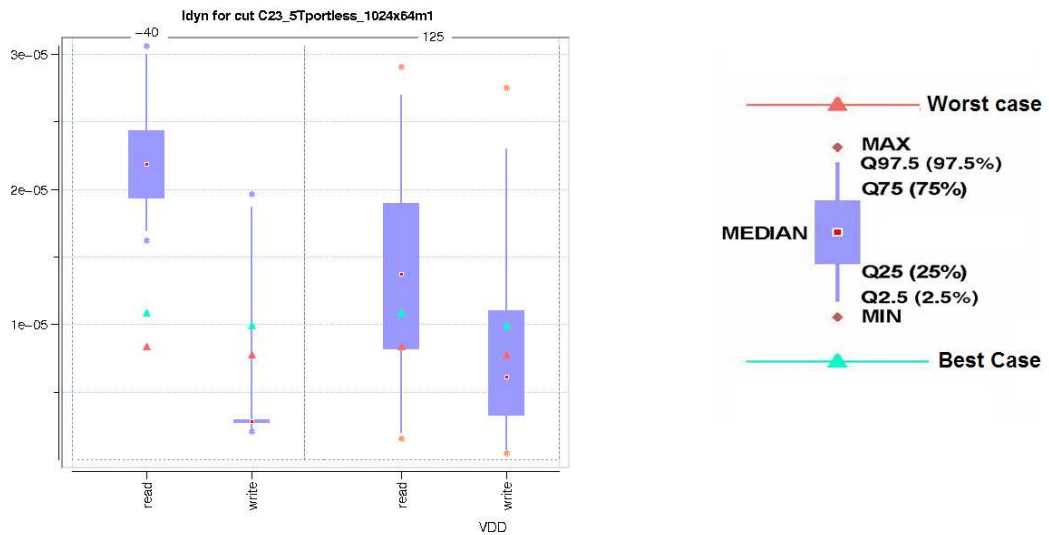


Figure 5.30: Test chip dynamic current measurements and CAD values for the full memory cut.

*Pulse Generator* have been modified to reduce the delays in read/write operations and improve the functionality. The dynamic power consumption is not affected. The potential of some critical nodes have been initialized to guarantee the detection of the Portless functionality even in the case of a second drop in yield. All simulations for the verification in different PVT corners have successfully been performed and the test chip is now in manufacturing line.

---

## Conclusion

---

SRAM memories and moreover embedded SRAMs face a number of challenges in coming technology nodes. The magnitude of variations in device performances is increasing as much as the transistor size decreases according to a  $\sigma_{V_{th}} = A/\sqrt{WL}$  dependence. The exponential increase in memory size with each product generation amplifies also the impact of the variability. Hence the required manufacturing yield at the bit-cell level increases proportionally to the memory size, as detailed in Chapter 3.

The leakage current is exponentially increasing at each technology node. The static power consumption becomes then a significant part in the global chip consumption. Classical techniques for leakage reduction are coming to a limit beyond 45nm. The reduction in dynamic power consumption is addressed by the power supply ( $V_{DD}$ ) scaling. Unfortunately the  $V_{DD}$  scaling impacts negatively the SRAM stability. The trade-off between power consumption and stability becomes difficult to satisfy and difficult to verify. The Monte-Carlo approach becomes impracticable or insufficient.

Several products now in manufacturing or in development continues to includes more and more applications but must be low power such as mobile or medical applications. We live in an always-on world. Some applications must now be always on as mobile interfaces; some kinds of sensor, supervision systems, medical applications... These applications can not be in sleep mode. In such applications the power consumption issue is dramatic. The PhD objective was to propose a solution for the SRAM

memory in advanced technology nodes, for embedded always-on applications. Design solutions were solely investigated. Process options were listed as the state of the art. In the state of the art, variability impacts were detailed at bit-cell level, bit-cell column and matrix level. The impact of variability on stability, consumption, density and performances were presented. Some existing solutions have been mentioned with their limitations in advanced technologies. Some mostly used bit-cells were studied with their benefits and disadvantages, with respect to variability and power consumption issues.

The targeted manufacturing yield for the SRAM bit-cell leads to narrower margin windows notably for the read stability characterized by the Static Noise Margin (SNM) and the write ability characterized by the Write Margin (WM). Both parameters represent one main design problem now faced by the memory designer. During the PhD works, a methodology for the variability modeling was studied as summarized in Chapter 3. It is demonstrated that the estimation of an optimal margin with respect to a given parameter and for a targeted manufacturing yield, can be determined with a good accuracy. This method costs less effort than the Monte Carlo simulation and gives more insight. The results of the study were compared to the Monte Carlo simulations in the case of the 6T bit-cell.

The state of the art concludes that the main contributor in static power consumption (leakage) is the bit-cell. Most of the dynamic consumption is dissipated in the bit-line capacitances. The 5T Portless bit-cell has been considered for its intrinsic better dispositions with respect to variability. Moreover the current mode operation presents an important interest. The absence of *Pass Gates* transistors reduces the impact of the bit-lines on the bit-cell internal nodes and eliminates their contribution in term of leakage current. The Portless is then identified as a low leakage and more stable bit-cell compared to the traditional 6T SRAM. The current mode operation allows to keep the bit-lines at  $V_{DD}$  so the dynamic power consumption is reduced.

---

The classical sensing technique does not work in advanced technology nodes because of increasing offsets. An original technique for write and read operations was introduced, the *hard line duplication*. The technique is associated to a particular operation of the control transistor in the bit-cell (AXS). This contribution defines new operating conditions for the Portless that extend its functionality beyond the 45nm node. The hard-line copy allows also the implementation of a low power multiplexed architecture. In the Portless architecture, the read and write operations are symmetrical so there is no conflict between them. So this solves the traditional problem in 6T between the SNM and WM. The IR-drop issue is reduced in Portless structure because of its low current values and a lack of significant current spikes.

The periphery of the bit-cell matrix arrangement includes the generation of various control signal. As much as possible, the signals are generated with a correction against the process status. This participates to the reduction of the impact of variability and consequently increases the manufacturing yield of the bit-cells.

A layout of 1024x32bits has been developed in standard 32nm CMOS using the available *Design Kit* at time of design. The simulation results demonstrate the Portless benefits in terms of static and dynamic power consumption compared to the 6T SRAM structure. A read/write operation with an indicative operating frequency of 100 MHz can be easily achieved. The simulations demonstrate that the 5T Portless is a good candidate for always-on, limited frequency applications.

The fabricated testchip presents large discrepancies with regards to CAD results. The large variation of the saturation current,  $I_{ON}$ , of the transistors and the large value of the leakage current are caused by a high drop in fabrication yield. A redesign has been achieved taking advantage of a latest *Design Kit* that imposed many fixes.

As mentioned in chapter 5, the performances of the Portless structure can be improved by optimization of the periphery. The bit-cell density can be improved by necessitates the SRAM implants during the fabrication process. The Portless perfor-

mances would be also improved, simulations show that in the Fast-Slow corner, the Portless presents less delays and less dynamic power consumption. The SRAM implants bring these benefits.

The main perspective to prove the industrial interest of the Portless is first to obtain a testchip with a nominal process.

Modeling for variability has been experienced. The modest contribution is sufficient to push for additional efforts. A first step is to develop a similar model for another significant parameter and concludes with the benefit of the approach compared to Monte Carlo simulations. A second step, in fact a dream, would be to get a huge number of a same test chip, fabricated in different lots and different locations to build a statistical study of the variability effects. Possessing these experimental results renders possible to confront the achievement of the proposed modeling approach compared to a classical procedure. Moreover the experimental results would quantify a real manufacturing yield of the Portless bit-cell. It is a dream because we are talking here of more than  $10^9$  test-chips of 1024 words.







---

## Bibliography

---

- [1] T. Ohsawa, K. Fujita, K. Hatsuda, T. Higashi, T. Shino, Y. Minami, H. Nakajima, M. Morikado, K. Inoh, T. Hamamoto, S. Watanabe, S. Fujii, and T. Furuyama. Design of a 128-mb SOI DRAM using the floating body cell (FBC). *IEEE Journal of Solid-State Circuits*, 41(1):135–145, January 2006.
- [2] S. Khan and S. Hamdioui. Trends and challenges of sram reliability in the nano-scale era. In *Design and Technology of Integrated Systems in Nanoscale Era (DTIS), 2010 5th International Conference on*, pages 1–6, 2010.
- [3] Shiao-Li Tsao and E-Cheng Cheng. Energy-conserving always-on schemes for a mobile node with multiple interfaces in all-IP network. In *Personal, Indoor and Mobile Radio Communications, 2007. PIMRC 2007. IEEE 18th International Symposium on*, pages 1–5, Athens, 2007.
- [4] Wan-Ki Park, Chang sic Choi, Il woo Lee, and Jonghyun Jang. Energy efficient multi-function home gateway in always-on home environment. *IEEE Transactions on Consumer Electronics*, 56(1):106–111.
- [5] D. A. El-Dib, Z. Abid, and H. A. Shawkey. Investigating an aggressive mode for drowsy cache cells. In *Canadian Conference on Electrical and Computer Engineering CCECE.*, pages 000901–000904, Niagara Falls, ON, 2008.
- [6] B. Davydov and V. Gopkalof. Real time energy consumption monitoring as a tool for the freight trains dispatching. In *4th IET International Conference on Railway Condition Monitoring*, pages 1–2, Derby, 2008.
- [7] ITRS. 2008 edition roadmap.
- [8] B. Cheng, S. Roy, G. Roy, F. Adamu-Lema, and A. Asenov. Impact of intrinsic parameter fluctuation in decanano MOSFET on a yield and functionality SRAM cell. *IEEE Solid-State Electronics*, 49, 2005.
- [9] F. Boeuf, M. Sellier, A. Farcy, and T. Skotnicki. An evaluation of the CMOS technology roadmap from the point of view of variability, interconnects, and power dissipation. *IEEE Transactions on Electron Devices*, 55(6):1433–1440, June 2008.

## Bibliography

---

- [10] Wei Dong, Peng Li, and G.M. Huang. Sram dynamic stability: Theory, variability and analysis. pages 378 –385, 10-13 2008.
- [11] T. Skotnicki, G. Merckel, and C. Denat. Mastar - a model for analog simulation of subthreshold, saturation and weak avalanche regions in mosfets. pages 146 –147, may. 1993.
- [12] M.J.M. Pelgrom, H. Tuinhout, and M. Vertregt. Transistor matching in analog CMOS applications. *Proceedings of IEEE International Electron Devices Meeting*, pages 915–918, 1998.
- [13] Zheng Guo, A. Carlson, Liang-Teck Pang, K. T. Duong, Tsu-Jae King Liu, and B. Nikolic. Large-scale SRAM variability characterization in 45 nm CMOS. *IEEE Journal of Solid-State Circuits*, 44(11):3174–3192, 2009.
- [14] S. Chellappa, Jia Ni, Xiaoyin Yao, N. Hindman, J. Velamala, Min Chen, Yu Cao, and L.T. Clark. In-situ characterization and extraction of sram variability. In *Design Automation Conference (DAC), 2010 47th ACM/IEEE*, pages 711 –716, 2010.
- [15] T. Fischer, E. Amirante, P. Huber, T. Nirschl, A. Olbrich, M. Ostermayr, and D. Schmitt-Landsiedel. Analysis of read current and write trip voltage variability from a 1-MB SRAM test structure. *Semiconductor Manufacturing, IEEE Transactions on*, 21(4):534 –541, 2008.
- [16] T. Azam, B. Cheng, and D.R.S. Cumming. Variability resilient low-power 7t-sram design for nano-scaled technologies. In *Quality Electronic Design (ISQED), 2010 11th International Symposium on*, pages 9 –14, 2010.
- [17] L. Chang, R. K. Montoye, Y. Nakamura, K. A. Batson, R. J. Eickemeyer, R. H. Dennard, W. Haensch, and D. Jamsek. An 8t-SRAM for variability tolerance and low-voltage operation in high-performance caches. In *Solid-State Circuits, IEEE Journal of*, volume 43, pages 956–963, Lille, France, April 2008.
- [18] Vita Pi-Ho Hu, Ming-Long Fan, Chien-Yu Hsieh, Pin Su, and Ching-Te Chuang. Finfet sram cell optimization considering temporal variability due to nbtI/pbtI and surface orientation. In *Simulation of Semiconductor Processes and Devices (SISPAD), 2010 International Conference on*, pages 269 –272, 2010.
- [19] K. Endo, S. O’uchi, Y. Ishikawa, Y. Liu, T. Matsukawa, K. Sakamoto, J. Tsukada, H. Yamauchi, and M. Masahara. Variability analysis of tin finfet sram cell performance and its compensation using vth-controllable independent double-gate finfet. In *VLSI Technology Systems and Applications (VLSI-TSA), 2010 International Symposium on*, pages 124 –125, 2010.

- [20] Xiao Zhang, Jing Li, M. Grubbs, M. Deal, B. Magyari-Kope, B.M. Clemens, and Y. Nishi. Physical model of the impact of metal grain work function variability on emerging dual metal gate mosfets and its implication for sram reliability. In *Electron Devices Meeting (IEDM), 2009 IEEE International*, pages 1–4, 2009.
- [21] S. Mukhopadhyay, Keunwoo Kim, and Ching-Te Chuang. Device design and optimization methodology for leakage and variability reduction in sub-45-nm FD/SOI SRAM. *IEEE Trans. Electron Devices*, 55(1):152–162, January 2008.
- [22] R. Tsuchiya, N. Sugii, T. Ishigaki, Y. Morita, H. Yoshimoto, K. Torii, and S. Kimura. Low voltage (vdd 0.6 v) sram operation achieved by reduced threshold voltage variability in sotb (silicon on thin box). In *VLSI Technology, 2009 Symposium on*, pages 150–151, 2009.
- [23] V.P.-H. Hu, Yu-Sheng Wu, Ming-Long Fan, Pin Su, and Ching-Te Chuang. Investigation of static noise margin of ultra-thin-body soi sram cells in subthreshold region using analytical solution of poisson’s equation. In *VLSI Technology, Systems, and Applications, 2009. VLSI-TSA ’09. International Symposium on*, pages 115–116, 2009.
- [24] M. Suzuki, T. Saraya, K. Shimizu, T. Sakurai, and T. Hiramoto. Post-fabrication self-convergence scheme for suppressing variability in sram cells and logic transistors. In *VLSI Technology, 2009 Symposium on*, pages 148–149, 2009.
- [25] B. Giraud and A. Amara. Read stability and write ability tradeoff for 6t SRAM cells in double-gate CMOS. In *Electronic Design, Test and Applications, 2008. DELTA 2008. 4th IEEE International Symposium on*, pages 201–204, Hong Kong, January 2008.
- [26] A. Kumar, Huifang Qin, P. Ishwar, J. Rabaey, and K. Ramchandran. Fundamental data retention limits in SRAM standby experimental results. In *Quality Electronic Design, 2008. ISQED 2008. 9th International Symposium on*, pages 92–97, San Jose, CA, March 2008.
- [27] Jiajing Wang, A. Singhee, R. A. Rutenbar, and B. H. Calhoun. Statistical modeling for the minimum standby supply voltage of a full SRAM array. In *33rd European Solid State Circuits Conference, 2007. ESSCIRC*, pages 400–403, Munich, September 2007.
- [28] A. Agarwal, S. Mukhopadhyay, C. H. Kim, A. Raychowdhury, and K. Roy. Leakage power analysis and reduction: models, estimation and tools. In *Computers and Digital Techniques, IEE Proceedings-*, volume 152, pages 353–368, May 2005.

## Bibliography

---

- [29] D. Pramanik, V. Moroz, and Xi Wei Lin. Process induced layout variability for sub 90nm technologies. In *Solid-State and Integrated Circuit Technology, 2006. ICSICT '06. 8th International Conference on*, pages 1849–1852, Shanghai, 2006.
- [30] A. J. Bhavnagarwala, Xinghai Tang, and J. D. Meindl. The impact of intrinsic device fluctuations on CMOS SRAM cell stability. *IEEE Journal of Solid-State Circuits*, 36(4):658–665, April 2001.
- [31] M. Yamaoka and H. Onodera. A detailed vth-variation analysis for sub-100-nm embedded SRAM design. In *International SOC Conference, 2006 IEEE*, pages 315–318, Austin, TX, September 2006.
- [32] B. Amelifard, F. Fallah, and M. Pedram. Leakage minimization of SRAM cells in a dual- $v_t$  and dual- $t_{rmax}$  technology. *IEEE Trans. VLSI Syst.*, 16(7):851–860, July 2008.
- [33] P. Athe and S. Dasgupta. A comparative study of 6t, 8t and 9t decanano sram cell. In *Industrial Electronics Applications, 2009. ISIEA 2009. IEEE Symposium on*, volume 2, pages 889–894, oct. 2009.
- [34] H. Yamauchi. Embedded SRAM circuit design technologies for a 45nm and beyond. In *ASIC, 2007. ASICON '07. 7th International Conference on*, pages 1028–1033, Guilin, October 2007.
- [35] M.M. Khellah, A. Keshavarzi, D. Somasekhar, T. Karnik, and V. De. Read and write circuit assist techniques for improving vccmin of dense 6t sram cell. In *Integrated Circuit Design and Technology and Tutorial, 2008. ICICDT 2008. IEEE International Conference on*, pages 185–188, june 2008.
- [36] T.S. Doorn, J.A. Croon, E.J.W. ter Maten, and A. Di Bucchianico. A yield centric statistical design method for optimization of the sram active column. In *ESSCIRC, 2009. ESSCIRC '09. Proceedings of*, pages 352–355, sept. 2009.
- [37] Keejong Kim, H. Mahmoodi, and K. Roy. A low-power SRAM using bit-line charge-recycling. In *Solid-State Circuits, IEEE Journal of*, volume 43, pages 446–459, Lille, France, February 2008.
- [38] S.K. Jain, K. Srivastva, and S. Kainth. A novel circuit to optimize access time and decoding schemes in memories. In *VLSI Design, 2010. VLSID '10. 23rd International Conference on*, pages 117–121, 3-7 2010.
- [39] Haitao Fu, Kiat-Seng Yeo, Anh-Tuan Do, and Zhi-Hui Kong. Design and performance evaluation of a low-power data-line sram sense amplifier. In *Integrated Circuits, ISIC '09. Proceedings of the 2009 12th International Symposium on*, pages 291–294, 14-16 2009.

- [40] A. Bhavnagarwala, S. Kosonocky, C. Radens, R. Stawiasz, K. Mann, Q. Ye, and K. Chin. Fluctuation limits and scaling opportunities for cmos sram cells. *IEEE international Electron Devices Meeting*, 2005.
- [41] M. Bhargava, M.P. McCartney, A. Hoefler, and K. Mai. Low-overhead, digital offset compensated, sram sense amplifiers. pages 705–708, sep. 2009.
- [42] Ding-Ming Kwai, Ching-Hua Hsiao, Chung-Ping Kuo, Chi-Hsien Chuang, Min-Chung Hsu, Yi-Chun Chen, Yu-Ling Sung, Hsien-Yu Pan, Chia-Hsin Lee, Meng-Fan Chang, and Yung-Fa Chou. SRAM cell current in low leakage design. *Memory Technology, Design, and Testing, 2006. MTD '06. 2006 IEEE International Workshop on*, August 2006.
- [43] I. Carlson, S. Andersson, S. Natarajan, and A. Alvandpour. A high density, low leakage, 5t SRAM for embedded caches. In *Solid-State Circuits Conference, 2004. ESSCIRC 2004. Proceeding of the 30th European*, pages 215–218, September 2004.
- [44] S. Cosemans, W. Dehaene, and F. Catthoor. A low power embedded SRAM for wireless applications. In *Solid-State Circuits Conference, 2006. ESSCIRC 2006. Proceedings of the 32nd European*, pages 291–294, Montreux, September 2006.
- [45] M. Wieckowski and M. Margala. A novel five-transistor (5t) sram cell for high performance cache. In *SOC Conference, 2005. Proceedings. IEEE International*, pages 101–102, Herndon, VA, September 2005.
- [46] M. Wieckowski, S. Patil, and M. Margala. Portless SRAMa high-performance alternative to the 6t methodology. In *Solid-State Circuits, IEEE Journal of*, volume 42, pages 2600–2610, Lille, France, November 2007.
- [47] M. Wieckowski and M. Margala. A portless SRAM cell using stunted wordline drivers. In *Circuits and Systems, 2008. ISCAS 2008. IEEE International Symposium on*, pages 584–587, Seattle, WA, May 2008.
- [48] E. Seevinck, P. J. van Beers, and H. Ontrop. Current-mode techniques for high-speed VLSI circuits with application to current sense amplifier for CMOS SRAM's. In *Solid-State Circuits, IEEE Journal of*, volume 26, pages 525–536, Honolulu, HI, April 1991.
- [49] S. Sundaram, P. Elakkumanan, and R. Sridhar. High speed robust current sense amplifier for nanoscale memories: a winner take all approach. In *VLSI Design, 2006. Held jointly with 5th International Conference on Embedded Systems and Design., 19th International Conference on*, January 2006.

## Bibliography

---

- [50] J. F. Richard and Y. Savaria. High voltage charge pump using standard CMOS technology. In *Circuits and Systems, 2004. NEWCAS 2004. The 2nd Annual IEEE Northeast Workshop on*, pages 317–320, June 2004.
- [51] K. Kobayashi, J. Yamaguchi, and H. Onodera. Measurement results of on-chip IR-drop. pages 521–524.